ВІСНИК
КИЇВСЬКОГО НАЦІОНАЛЬНОГО УНІВЕРСИТЕТУ ІМЕНІ ТАРАСА ШЕВЧЕНКА

ISSN 1728-2306

РАДІОФІЗИКА ТА ЕЛЕКТРОНІКА 15/2011

Засновано 1999 року

Публікуються результати експериментальних і теоретичних досліджень у галузях фізичної електроніки, фізики плазми, фізики поверхні твердого тіла, емісійної електроніки, кріогенної та мікроелектроніки, нанофізики та наноелектроніки, високотемпературної надпровідності, квантової радіофізики, функціональної електроніки, твердотільної електроніки, мобільного зв'язку, медичної радіофізики, методів отримання діагностичної інформації та її комп'ютерної обробки.

Для науковців, викладачів вищої школи, студентів.

Experimental and theoretical contributions are published in the following fields: physical electronics, plasma physics, solid-state surface physics, emission electronics, cryogenic electronics, microelectronics, nanophysics and nanoelectronics, high-temperature supercondactive electronics, solid-state electronics, functional electronics, microwave electronics, quantum electronics, mobile communication, medical radiophysics, methods of receipt and computer processing of diagnosis information.

Designed for researches, university teachers, students.

ЗМІСТ

CONTENTS

UDC 537.86/.87

D. Bozhko, stud.,
O. Prokopenko, Ph. D.

MICROWAVE ANTENNAS FOR TELECOMMUNICATION DEVICES BASED ON SPIN-TORQUE OSCILLATORS AND OSCILLATOR ARRAYS

Розглянуто можливість застосування різноманітних малорозмірних мікрохвильових антен для створення телекомунікаційних пристроїв на основі магнітних нано-автогенераторів та їх масивів. Показано, що хоча розміри антен суттєво менші за робочу довжину хвилі мікрохвильового сигналу, такі антени мають достатньо добрі характеристики (коефіцієнт підсилення > 1). Розглянуті антени можуть бути використані для створення практичних мікрохвильових пристроїв, причому в якості антени може бути використаним корпус мікросхеми з кількома магнітними нано-автогенераторами. В роботі показано, що робоча напруга на вході/виході відповідного пристрою може досягати декількох мВ для мікрохвильових сигналів з потужністю в декілька нВт у розрахунку на один нано-автогенератор.

Ключові слова: магнітний нано-автогенератор, мікрохвильова антена, телекомунікаційний пристрій.

The possibility of application of different low-size microwave planar antennas as potential microwave antennas for telecommunication devices based on spin-torque nano-oscillators and oscillator arrays is considered. Although the antenna sizes are substantially smaller than operating wavelength of the microwave signal the antennas have high enough performance (amplification coefficient > 1). These antennas can be used for creation of real devices; the antenna can be implemented as a shell of the microchip with several spin-torque nano-oscillators. We have shown that the devices can provide the dc output voltage of several mV for microwave power of several nW from a single STNO.

Key words: spin-torque nano-oscillator, microwave antenna, telecommunication device.

Introduction. The discovery of the spin-transfer-torque (STT) effect in magnetic multilayers, theoretically predicted by J. C. Slonczewski [54] and L. Berger [12] and after that experimentally observed by many authors [4, 5, 9, 10, 19–21, 31, 39, 40, 46, 57], opened a possibility for a new method of generation of microwave oscillations that does not involve any semiconductor materials or devices [51]. The STT effect turned out, that electric direct current passing through a magnetized magnetic layered structure becomes spin-polarized and, if the current density is sufficiently high, this spin-polarized current can transfer enough spin angular momentum between the magnetic layers to destabilize the static equilibrium orientation of magnetization in the thinner ("free") magnetic layer of the multilayered structure. Depending on the actual geometry and properties of the magnetic structure and the magnitude of the external bias magnetic field, this phenomenon can lead either to the magnetization switching (reversal of the magnetization direction) [3, 4, 11, 23, 55], or to the magnetization precession with the frequency close to the frequency of the ferromagnetic resonance (FMR) in the magnetic layer [19-21, 39, 40, 46]. In the last case the frequency of the current-induced precession is close to the frequency of the most unstable spin wave mode of the "free" magnetic layer (i.e. it is close to the FMR frequency), depends on the current magnitude, and, typically, lies in the microwave range. The generated microwave signal can be registered, typically, as oscillations of the multilayer resistance through to the effects of giant magnetoresistance (GMR) [9, 21, 22] or tunneling magnetoresistance (TMR) [17, 28, 29] due to the fact that in the course of precession the orientation of the magnetization of the "free" layer relative to the static magnetization of the "fixed" layer oscillates with microwave frequency. The other recently discovered possible method of registration of the microwave signal generated in magnetic multilayer structures is based on the observation of direct electromagnetic emission from the multilayer structures [8].

Practical applications of above described magnetization dynamics in non-volatile magnetic random access memory, microwave nanometer-scale oscillators, detectors, mixers and other devices are under development [14, 18, 34], and non-equilibrium states of magnetization induced by STT are of fundamental interest in nonlinear science [1, 43, 51]. Also STT is used in spin torque ferromagnetic resonance measurements of spin waves in magnetic nano-structures [13, 16, 29].

Microwave spin-torque nano-sized auto-oscillators (STNO) based on either fully metallic GMR spin valves or magnetic tunnel junctions, having a thin dielectric spacer and employing TMR effect, are very attractive for potential applications in active nano-sized devices in microwave spintronics [13, 14, 16, 18, 34, 47, 51]. The major problem that arises during the development and application of such nano-sized devices is the small microwave output power that can be extracted from a single STNO. In the case of a STNO based on the GMR effect this power is relatively small (around one nW) [20–22], while in the case of a STNO based on the TMR effect it can reach 1 μW [17, 28, 29, 32].

The characteristic value of operating level microwave power of modern telecommunication devices is around 10÷1000 μW, thus, one can see to create a practical source of microwave signals based on STNOs it would be useful to use arrays of coupled and synchronized STNOs [7, 15, 32]. There are two approaches to create such an array of STNOs. The first (traditional) approach is to form an array of N oscillators connected in parallel or in series and coupled by a common bias current. In such a case, as it was shown in [27], the output power extracted through the magnetoresistance (MR) mechanism from an array of N synchronized STNOs is N times larger than the power of a single STNO. The second approach is to place N STNOs (coupled through their dipolar electromagnetic fields) inside a resonator with a high Q-factor and extract the power through the dipolar emission mechanism [8]. In that case, as it was shown in [42], the output power of the N oscillator array can be N2 times larger than the power of a single oscillator, as long the total microwave power extracted from the resonator coupled to the array remains smaller then the power caused by Gilbert damping in a single STNO in the array [8].

In order to use a single STNO and oscillator arrays in telecommunication devices it is necessary to provide a special device, which from the one hand allow to effectively transmit the microwave signal generated by a STNO or an array of synchronized STNOs, receive the external microwave signal (which can be a signal from another STNO), and on the second hand allow to effectively match the impedance of a single STNO (or STNO arrays) with the impedance of a transmission line. The simplest type of above described device is a matched microwave antenna, which application allows solving all considered problems simultaneously.

Thus, the goals of this paper are to make a review of existing types of microwave antennas, analyze the possible applications of different types of microwave antennas for the development of microwave devices based on STNOs and STNO arrays, make a design of several antennas with acceptable technological parameters and estimate their performance.

Brief review of microwave antennas. There are several classification schemes of microwave antennas [30, 35, 37, 38, 56, 59] including the schemes, where the antennas are differentiate by their physical construction, functional predestination, type of used input microwave transmission lines, frequency range, physical principles of operations etc. Further we shall use the simple and understandable classification scheme based on the principle of forming of antenna's directional dia-

gram; also we shall consider only the passive antennas. In accordance with the declared above classification microwave antennas can be divided on three classes: linear antennas, aperture antennas and antenna arrays [30, 35, 37, 38, 56, 59].

Linear antennas consist of one or several external conductors (typically, metal wires); microwave currents are flowing along the conductors [30, 35, 37, 56, 59]. The direction of microwave current flow is coincided with the axis of symmetry of the system. Typically, the longitudinal sizes of such antennas are comparable with the wavelength λ of operating microwave signal, while the transversal sizes are much smaller then the wavelength λ. The view of several various linear antennas is shown in Fig. 1.

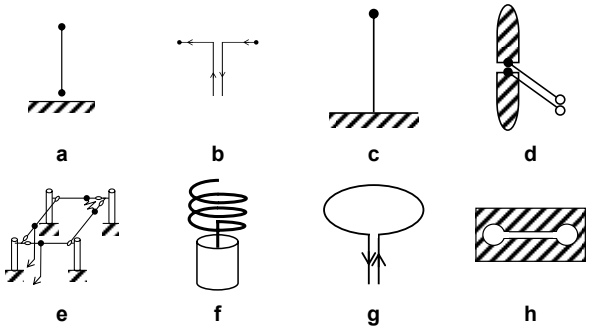

Fig. 1. Various types of linear antennas: (a) single-wire antenna, (b) dipole antenna, (c) monopole antenna, (d) wide-band flat antenna, (e) linear beam (rhombic) antenna, (f) traveling-wave antenna, (g) loop antenna, (h) slot antenna. Shaded area is the conductor area

Linear antennas can be implemented as standing-wave antennas or traveling-wave antennas [30, 35, 37, 59]. The class of standing-wave antennas includes single-wire antennas (see Fig. 1 a), dipole and monopole antennas (see Fig. 1 b, c, respectively), slot antennas (see Fig. 1 h), loop antennas (see Fig. 1 g) and other. The traveling-wave regime in traveling-wave antennas is realized by the one-end excitation of the antenna while the absorption load is connected to the other end of the antenna or by the continuous decrease of field amplitude along the antenna, for example, due to the electromagnetic energy radiation caused by a current flow. The typical traveling-wave antennas are spiral antennas, dielectric rod antennas and surface wave antennas. The significant specialty of the linear antennas is the series bias (excitation) of antenna's elements, and therefore, possible dependence of antenna's characteristics on antenna length or operating frequency

Linear antennas are widely used as antennas of VHF and UHF bands, and as the core element of some radar [6, 25, 30, 37, 50]. Linear microstrip antennas are used in microelectronics devices, in mobile phones and other wireless communication devices [6, 24, 25, 41, 50].

In aperture antennas [30, 35, 37, 56, 59] one can select some confined surface, typically, flat, through which the electromagnetic energy is radiated or received. This surface, named the aperture, typically, has the characteristic sizes greater than the wavelength λ. The class of aperture antennas includes horn antennas, dish antennas, lens antennas and the antennas based on open-end transmission lines, for instance, open-end waveguide antennas (Fig. 2).

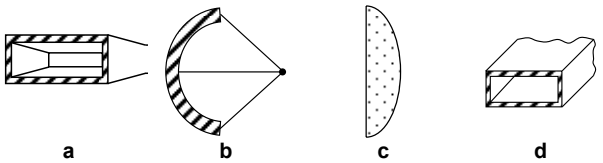

Fig. 2. Various types of aperture antennas: (a) horn antenna, (b) dish antenna, (c) lens (dielectric) antenna, (d) open-end waveguide antenna. Shaded area is the conductor area

The principles of forming of aperture antenna's direction diagram are similar to the principles for optical systems. The specialty of this class of antennas is the parallel bias (excitation) of antenna's elements by a group of independent electromagnetic rays, and therefore, independence of the direction diagram on characteristic aperture size or operating frequency.

Aperture antennas, especially dish antennas are typically used in wireless, satellite and space communications, as the basic element of various radars and as the base element of antenna arrays [6, 25, 30, 35, 37, 50, 56, 59].

Antenna arrays [2, 30, 33, 35, 36, 37, 38, 44, 45, 56, 58, 59] are the systems of the elementary antennas (oscillators) of the same kind, distributed in space and excited by a specific law. Antenna arrays can be one-dimensional (linear array) or two-dimensional (surface array). The system of slots carved in waveguide walls can be an example of linear antenna array. The two-dimensional antenna array can be formed by a superposition of several linear antenna arrays. The oscillators in such an array can be placed on a flat or curved surface. The excitation scheme of antenna array can be series, parallel or combined (series-parallel). The most important class of antenna arrays is the class of phased antenna arrays [52–53, 55–57], which allow independent regulation of amplitude-phase distribution for each element of the array.

Antenna arrays are widely used in wireless and deep space communications, radars and radioastronomy etc. [2, 6, 25, 33, 36, 44, 45, 58].

Design of microwave antennas for the systems with STNOs. In order to use a STNO and oscillator arrays in telecommunication devices it is necessary to provide a special device, which from the one hand allow to effectively transmit the signal generated by a single STNO or an array of synchronized STNOs from the source to an external microwave circuits, receive the external microwave signal (which can be a signal from another STNO or STNO array), and on the second hand allow to effectively match the impedances of a single STNO (or STNOs) and a transmission line used for sending/receiving the microwave signals. At present time there are a few papers involving the investigation and application of several synchronized STNOs. For the first time the experimental investigation of two synchronized STNOs was performed in [32], a little later the theory of mutual and forced phase-locking of several STNOs [7, 51–53] was developed. The major results of this theory were successfully confirmed in the recent experiment involving four phase-locked STNOs [15].

The first experiments have shown the problems concerning to the creation and application of the arrays consisting of several STNOs. The crucial limitation of an output microwave power from the array of several synchronized STNOs coupled via dc bias current (the power from an array of N oscillators is scaling by a factor N [27, 42]) have forced us to examine the methods to extract the microwave power from the array other than the MR method. In the scope of this problem the extraction of the microwave power from an array of synchronized STNOs through the direct electromagnetic radiation can be convenient for the large arrays of oscillators [8]. Yet the value of typical impedance of a single STNO can vary from several Ohm to several kOhm and even tens and hundreds of kOhm. Therefore, typically, the impedances of a STNO or STNO array are not equal to the impedance of the free space $Z_0 = 120\pi \approx 377$ Ohm, so additional losses due to impedance mismatch are exist.

The other important problem is the converting of a microwave signal from a single STNO (or an array of synchronized STNOs) in the form that is convenient for wireless communications. The efficiency of the standard method, including the extraction the microwave current from a STNO (or STNO array) through the MR mechanism and further excitation of an antenna by this current, is limited by a described above the impedance mismatch effect. On the other hand the microwave signal generated by a single STNO or by an array of synchronized STNOs can be

transmitted/received through the natural dipole radiation, but the theory of these operations is not yet developed.

Thus, there are two possible ways to get rid of the problems described above:

1. The developing of a microwave matched antenna, which in the best case allow us to substantially avoid the impedance mismatching. In such a case the microwave signal is extracted from a STNO or oscillator array through the MR mechanism, after that the matched antenna is excited by the current;

2. The developing of a passive planar microwave system with embedded STNO or oscillator array. This system functions as the matched antenna, but the microwave power is not extracted through the MR mechanism, but through the direct electromagnetic radiation from the structure. For instance, this structure can be a microstrip resonator with embedded STNO or STNO array, matched to a free space (an example of such structure is considered in [8]).

Although the second possibility is much more attractive (especially for a large array of oscillators) than the first one, it is also substantially complicated. Therefore in that paper we shall try to analyze the first problem. So, our goal is to make a design of matched antenna that is convenient for the application in systems with STNOs and estimate the antenna performance.

Technical approach. STNO is a nano-sized quantum device, and so in all known cases STNOs are fabricated using planar micro- and nanotechnology [47, 51]. In order to simplify the extraction of microwave power from these devices (typically, through the MR mechanism) they are embedded into a planar microwave system, in most cases it is a coplanar waveguide [14, 47]. It is clear in this situation the simplest type of matched antenna is an antenna based on a planar technology. The main advantages of such type of an antenna are:

- Antenna and STNOs can be fabricated in the same technological process, therefore, the system is high reliable;
- It is easy to match the antenna and a microwave planar system with embedded STNOs (in some cases this system can be the antenna itself, i.e. the microwave planar system with STNOs functions as the matched antenna);
- The sizes of an antenna can vary in a wide ranges (can be larger and smaller than the wavelength λ of a microwave signal generated by a STNO or STNO array);
- Typically, planar antennas has lesser sizes than the non-planar antennas, therefore planar systems are convenient for developing microwave devices with small sizes;
- The final device (STNO + antenna) is cheap enough due to the use of standard planar technology;
- Using the standard methods micro- and nanotechnologies planar antennas can be fabricated with very high accuracy from sample to sample (of course, in the first place we consider the relative fabrication error $\Delta x / \lambda$, where Δx is the absolute error value of length and λ is the wavelength of a microwave signal; Δx is typically around 10÷100 nm, thus $\Delta x <<< \lambda$ in a microwave band);
- Planar antennas are convenient for experimental investigations of the systems with STNOs and for their applications under trying conditions (for example, for military or space applications).

Taking into account above described advantages in this paper we consider the design and possible applications of several types of planar antennas: coplanar antenna, meander antenna, microstrip antenna, slot antenna and square spiral antenna. We also consider other types of planar and planar-like antennas in order to compare by performance one antenna with another.

Each considered planar antenna and many of other considered antennas has a three-layer structure:

- *Top layer* consists of the designed topology of the antenna. This topology is a composition of thin conductors of simple or complex shape, deposited on the dielectric (medium) layer;
- *Medium layer* is presented by a dielectric substrate;
- *Bottom layer* is a whole conductor film.

The general view of considered three-layer structures is shown in Fig. 3.

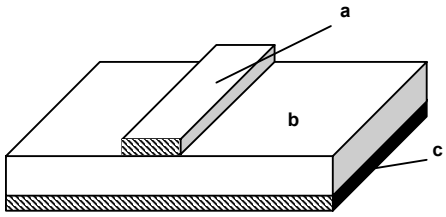

Fig. 3. General view of the considered antenna schematics: (a) the top layer consists of the antenna topology, (b) medium layer is made of dielectric, (c) whole conducting film. The majority of the considered antennas have a simple three-layer structure shown above, but the quantity of layers can be more than three for some planar-like antennas (for detailed information see Section 5)

In as much as we are planning to examine the designed antennas in real experiments involving STNOs, we fix the values of several parameters that are specific to the samples and experimental setup [14]. We use the following values of input parameters:

- Frequency range: 2÷5 GHz. The STNO samples we are planning to use in the experiments has the operation frequency in that range [14], so, for simplicity and in order to reduce the processor time needed for our calculations, we choose the frequency range as the range written above;
- The material of the dielectric substrate: Duroid 6002. The experimental samples we are planning to examine are fabricated on the Duroid 6002 dielectric substrates [49]. This type of dielectric has a relative dielectric constant $\varepsilon = 2.94 \pm 0.04$ [48, 49]. For simplicity in our calculations we use the average dielectric constant $\varepsilon = 2.96$;
- Thickness of the dielectric substrate in considered planar structure is chosen exactly as in the experiments, it equals 1.2 mm.

In our work we try to examine several antenna of the same schematics, but with different sizes (if it is convenient taking into account the performance of the antenna, time needed for performing our calculations, possibility of antenna application etc.). Many planar antennas are considered at least as "big" and "medium" size devices, some antennas are also considered as "small" size devices. The typical in-plane sizes (width and length of the dielectric substrate of the considered structure) of "big" antenna are 50×50 mm2, the sizes of "medium" antenna are 10×10 mm2, and the sizes of "small" antenna are 1×1 mm2. It is important to note that the epithets "big", "medium" and "small" have a figurative meanings, because the characteristic size x of all considered structures are less than the wavelength λ of microwave signal: $x < \lambda$. For "small" and "medium" antennas this inequality can be greatly improved to $x << \lambda$, because even for frequency 5 GHz the wavelength is $\lambda \sim 60$ mm.

Moreover in some cases (especially for planar-like antennas) we examine the antennas of other sizes. The reasons to do so are the wide application of such type and size antennas in wireless communications and microwave electronics and techniques, simplicity of calculation of the antenna performance, the existence of well-known and examined antenna performance etc.

General description of used theory, computational techniques and the electromagnetic simulator. During the analysis of designed antenna we used several computational techniques; the main techniques were the Finite-Difference Time-Domain (FDTD) method, Finite Element Method (FEM) and the Method of Moments (MoM). Each of these methods is well known and widely used for solving various problems and in numerous applications (not only for the electromagnetic simulations) [26].

In order to perform the required calculations we develop specialized software based on Wolfram Mathematica 7 software framework developed by Wolfram Research Inc.. Our electromagnetic simulator uses Maxwell's equations to compute the response of a structure from its physical geometry. Developed electromagnetic simulator can simulate highly arbitrary structures and nevertheless provide very accurate results. In addition, the simulator is not subject to many of the constraints of circuit models because it uses fundamental equations to compute the response. One limitation of our electromagnetic simulator is that simulation time grows exponentially with the size of the problem, thus it is important to minimize problem complexity to get timely results.

Electromagnetic simulation and circuit simulation are complementary techniques for circuit design, and the two approaches can be used in combination to solve many design problems. Our electromagnetic simulator is capable of simulating planar 3D structures containing multiple metallization and dielectric layers. The structures can have interconnecting vias (metallized links) between layers or to ground. Our simulator uses the Galerkin Method of Moments in the spectral domain. It is also specially optimized for analyzing microstrip, stripline, and coplanar structures as well as other more arbitrary media (the calculations performed with an extremely high accuracy). We hope, that if properly used, this technique implemented in our software can provide accurate simulation results up to the frequency bound of 100 GHz and beyond.

Our electromagnetic simulator includes enough fast (relatively to other commercial products for electromagnetic simulations) full-wave electromagnetic solver, that uses a modified spectral-domain method of moments to accurately determine the multi-port scattering parameters for predominately planar structures. In our simulator we also implemented a fast-frequency-sweep (FFS) algorithm that is up to an order of magnitude faster than other standard electromagnetic solvers. In addition to the FFS algorithm, we also realized a more conventional point-by-point solver.

At this time the electromagnetic simulator can analyze circuits with a limited number of layers (up to 10) and a limited number of ports (up to 10), but this is very enough for our calculations. The circuit is analyzed inside of a multi-layered rectangular enclosure. A gridded, variable cell size mesh can be set by a user, or automatically. The algorithm automatically places smaller cells in areas that have high variations in current densities, and larger cells in areas with more uniform current variations. The user can control the mesh by increasing the meshing density of specific polygons. The generated mesh can be viewed in Wolfram Matematica 7 software as 3D-image, while the geometry is being edited in any text editor so the effect of changing the meshing density can be seen instantly. Our de-embedding algorithm can automatically remove the discontinuities that arise from the excitations at the ports. In addition, arbitrary reference planes can be used for the de-embedding.

The important question is the question about the precision and stability of our simulator. Although our simulator is not certified yet, we compare the results obtained by our simulator for several (10) test 3-D planar structures with the results obtained for these structures by well-known CAD software, such as Ansoft HFSS, Femlab, Microwave Office and Sonnet. The difference between the results (relative error) was less than 0.1÷0.5 %, so it allows us to assert that our simulator works correctly.

Analysis procedure. Using the input parameters we designed the topology for major of considered antenna (coplanar, meander, microstrip, slot and square spiral antenna) and performed the evaluation of antenna parameters: the normalized total radiation power as the function of out-plane angle θ (the in-plane angle ϕ was equal to zero) and the normalized total radiation power as the function of in-plane angle ϕ (the out-plane angle θ was equal to zero) at different frequencies within the range 2–5 GHz. The evaluation was performed using our developed solver. During the calculations, for simplicity, we assume all metal parts of the antenna have an ideal conductivity.

Estimated antenna characteristics. During the analysis we evaluate three microwave characteristics of the structures (Fig. 4), listed below.

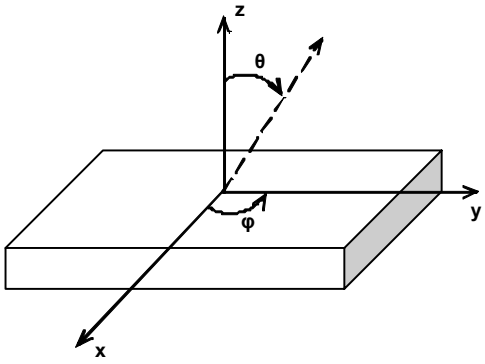

Fig. 4. General view of considered structure and a frame of reference. θ is the out-of-plane (vertical) angle and ϕ is the in-plane (polar) angle

Phi Sweep Curve. Phi Sweep is also known as a Conic Cut, which captures the total power in all directions, this measurement fixes the values of frequency and out-of-plane angle θ while sweeping in-plane angle ϕ from –180 to 180 degrees. The total power is defined as the sum of the power contained in E_θ and E_ϕ:

$$P(\theta,\phi)=\frac{1}{240\pi}\left(\left|E_\theta(\theta,\phi)\right|^2+\left|E_\phi(\theta,\phi)\right|^2\right) \qquad (1)$$

Phi Sweep returns a complex value $P_\theta(\phi)$, which represents the normalized far field radiation in the specified direction for all polarizations. This result is normalized to P_0 – an integration of the power (in all polarizations) in the upper hemisphere divided by 4π (asterisk denotes complex conjugate values):

$$P_\theta(\phi)=\sqrt{\frac{P(\theta,\phi)}{P_0}}\Bigg|_{-180°\le\phi\le180°,\theta=const}, \qquad (2)$$

$$P_0=\frac{1}{8\pi}\mathrm{Re}\int_0^{\pi}d\theta\int_0^{2\pi}d\phi\left(E_\theta H_\phi^*-E_\phi H_\theta^*\right)\sin\theta. \qquad (3)$$

The measurement $P_\theta(\phi)$ does not reflect the effect of mismatch or resistive losses. The result is an equivalent to a wave variable in the specified direction in order to preserve compatibility with other antenna measurements although the measurement is purely real. This insures that $\left[P_\theta(\phi)\right]^2$ is the directivity in that particular direction.

Theta Sweep Curve. Theta Sweep is also known as a Principal Plane Cut, which captures the total power in all polarizations, this measurement fixes the values of frequency and in-plane angle ϕ while sweeping out-of-plane angle θ from –90 to 90 degrees. The total power is defined by Ex. (1).

Theta Sweep returns a complex value $P_\phi(\theta)$, which represents the normalized far field radiation in the specified direction for all polarizations. This result is normalized to P_0 (see Ex. (3)):

$$P_\phi(\theta)=\sqrt{\frac{P(\theta,\phi)}{P_0}}\Bigg|_{-90°\le\theta\le90°,\phi=const}. \qquad (4)$$

The measurement $P_\phi(\theta)$ does not reflect the effect of mismatch or resistive losses. The result is an equivalent to a wave variable in the specified direction in order to preserve compatibility with other antenna measurements although the measurement is purely real. This insures that $\left[P_\phi(\theta)\right]^2$ is the directivity in that particular direction.

Performance of designed microwave antennas. The main results for each analyzed antenna are presented below. The results are presented by three figures.

The first figure is the topology of the top layer. Dark areas on these figures are the metal parts; white areas are vacuum (the dielectric substrate is visible through these areas). The borders of the system are shown by black lines. The square with number "1" is the excitation port; the external microwave signal is applied to that port.

The second and third figures are the normalized total radiation power as the function of polar angle ϕ or out-plane angle θ at different frequencies within the range 2–5 GHz, respectively.

Coplanar antenna. We assume that the coplanar antennas can be the most perspective antennas for STNOs, because in real samples STNOs are embedded in the coplanar waveguide in order to simplify microwave signal extraction from each STNO. Further we analyze the "medium"-size and "big"-size coplanar antennas.

2-D and 3-D views of considered "medium" and "big" coplanar antenna are shown in Fig. 5 (later on, we consider that Z-axis configuration is unchanged and similar to shown at Fig. 5, so 3-D view isn't necessary), while the performance curves of the antenna are shown in Fig. 6–7. The "big" antenna performance curves are shown in Fig. 8–9, respectively.

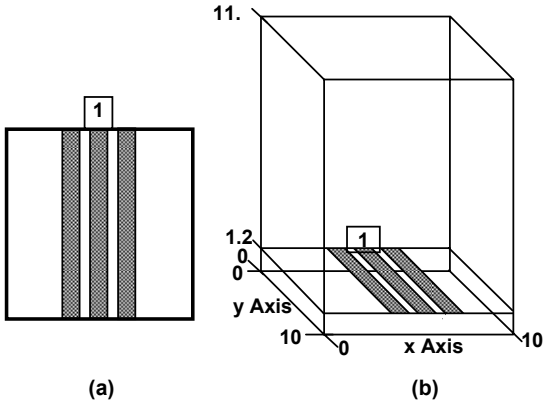

Fig. 5. (a) 2-D image of the topology (top layer) of the considered "medium" and "big" coplanar antenna. (b) 3-D images of the considered "medium" and "big" coplanar antenna (all sizes are in millimeters). The size of the structures (size of the black border frame in (a)) is 10×10 mm^2 and 50×50 mm^2 respectively. The dark filled area is the area of metallization. Conductor strips has a width of 1 mm and 5 mm, the distance between the strips is 0.5 mm and 2.5 mm respectively. Small square with number "1" is the virtual excitation port of the structure. The topology layer is located above the dielectric layer made of Duroid 6002 (ε = 2.96) with thickness 1.2 mm

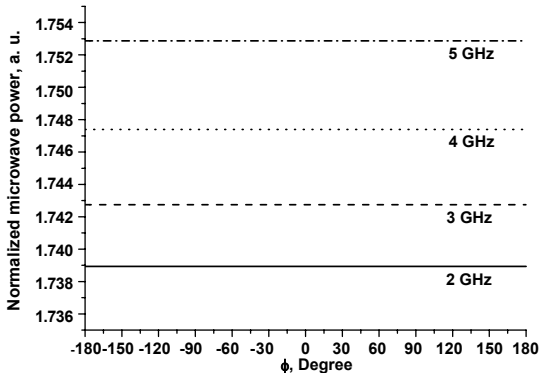

Fig. 6. Dependence of normalized total microwave power $P_\theta(\varphi)$ radiated by the "medium" coplanar antenna on the polar angle ϕ for various microwave frequencies and for out-of-plane angle θ = 0

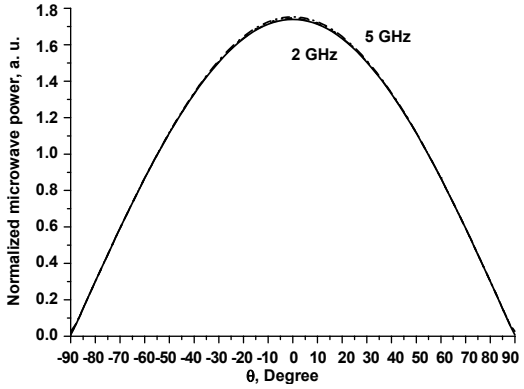

Fig. 7. Dependence of normalized total microwave power $P_\phi(\theta)$ radiated by the "medium" coplanar antenna on the out-of-plane angle θ for various microwave frequencies and for polar angle ϕ = 0

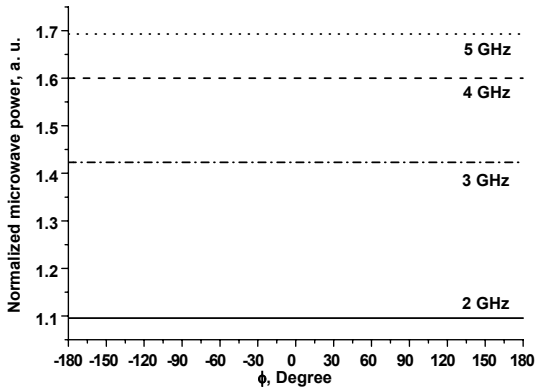

Fig. 8. Dependence of normalized total microwave power $P_\theta(\phi)$ radiated by the "big" coplanar antenna on the polar angle ϕ for various microwave frequencies and for out-of-plane angle θ = 0

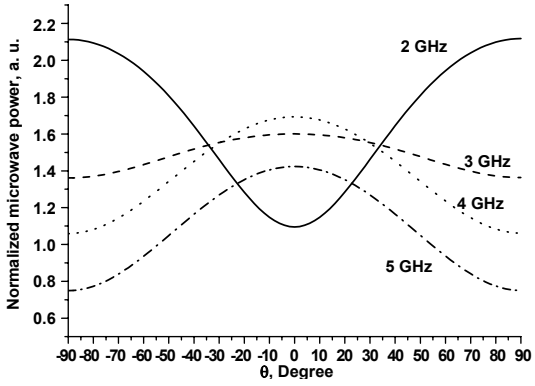

Fig. 9. Dependence of normalized total microwave power $P_\phi(\theta)$ radiated by the "big" coplanar antenna on the out-of-plane angle θ for various microwave frequencies and for polar angle $\phi = 0$

Meander antenna. Meander antenna can be easily fabricated and by varying the length of meander line the optimal microwave frequency of the antenna can be changed. Further we analyze the "medium"-size and "big"-size meander antennas.

2-D view of considered "medium" and "big" meander antenna is shown in Fig. 10, while the performance curves of the antenna are shown in Fig. 11–12. The views of "big"-size antenna performance curves are shown in Fig. 13 and 14 respectively.

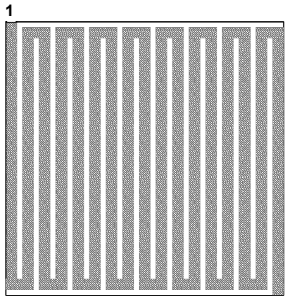

Fig. 10. 2-D image of the topology (top layer) of the considered "medium" and "big" meander antenna. The size of the structure (size of the black border frame) is 10×10 mm2 for "medium" and 50×50 mm2 for "big". The dark filled area is the area of metallization. Conductor strips has a width of 0.4 mm (2 mm for "big" antenna), the distance between the strips is 0.2 mm (1 mm for "big" antenna). Small square with number "1" is the virtual excitation port of the structure. The topology layer is located above the dielectric layer made of Duroid 6002 (ε = 2.96) with thickness 1.2 mm

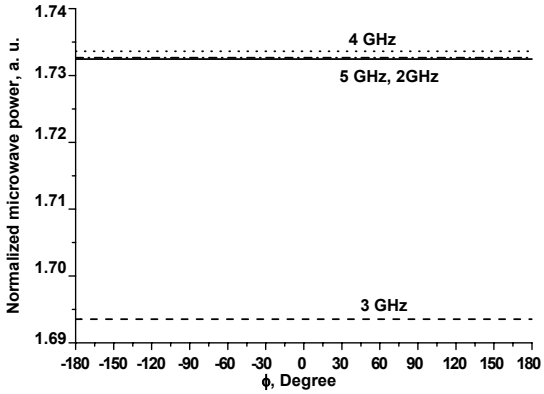

Fig. 11. Dependence of normalized total microwave power $P_\theta(\phi)$ radiated by the "medium" meander antenna on the polar angle ϕ for various microwave frequencies and for out-of-plane angle $\theta = 0$

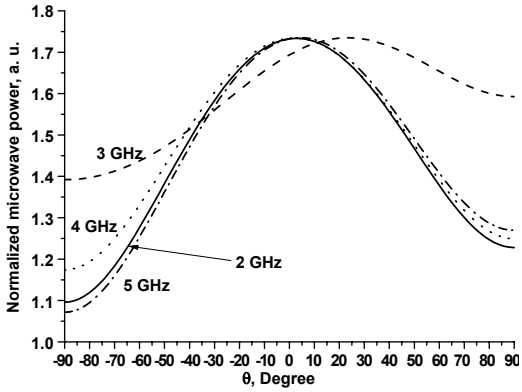

Fig. 12. Dependence of normalized total microwave power $P_\phi(\theta)$ radiated by the "medium" meander antenna on the out-of-plane angle θ for various microwave frequencies and for polar angle $\phi = 0$

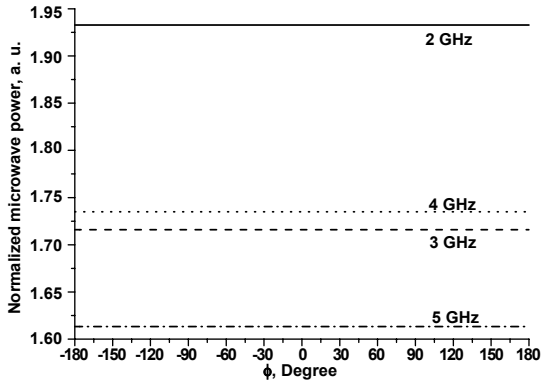

Fig. 13. Dependence of normalized total microwave power $P_\theta(\phi)$ radiated by the "big" meander antenna on the polar angle ϕ for various microwave frequencies and for out-of-plane angle $\phi = 0$

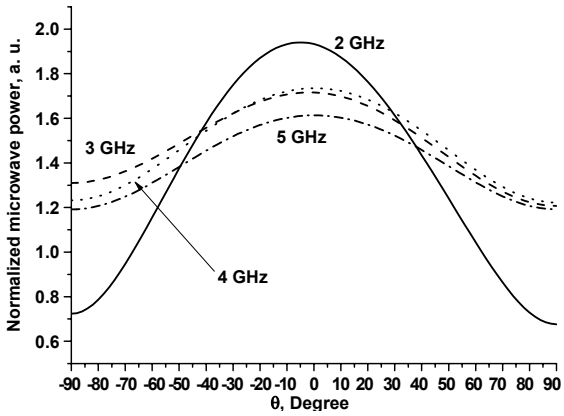

Fig. 14. Dependence of normalized total microwave power $P_\phi(\theta)$ radiated by the "big"-size meander antenna on the out-of-plane angle θ for various microwave frequencies and for polar angle $\phi = 0$

Microstrip antenna. Microstrip antenna is the simplest type of considered antennas. Many of the considered antenna can be considered as the very complicated microstrip antenna with more complicated topology. This is the reason why the performance of microstrip antenna is interesting.

Further we analyze the "medium"-size and "big"-size microstrip antennas.

2-D view of considered "medium" and "big" microstrip antenna is shown in Fig. 15, while the performance curves of the antenna are shown in Fig. 16–17. The performance curves of the "big" antenna are shown in Fig. 18 and 19, respectively.

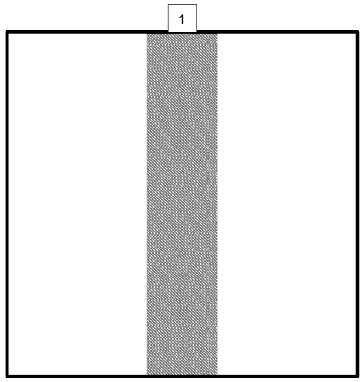

Fig. 15. 2-D image of the topology (top layer) of the considered "medium" and "big" microstrip antenna. The size of the structures (size of the black border frame) are 10×10 mm^2 and 50×50 mm^2 respectively. The dark filled area is the area of metallization. Conductor strips has a width of 2 mm and 5 mm, the distance from the strip to the edge of the structure is 4 mm and 22.5 mm respectively. Small square with number "1" is the virtual excitation port of the structure. The topology layer is located above the dielectric layer made of Duroid 6002 ($\varepsilon = 2.96$) with thickness 1.2 mm

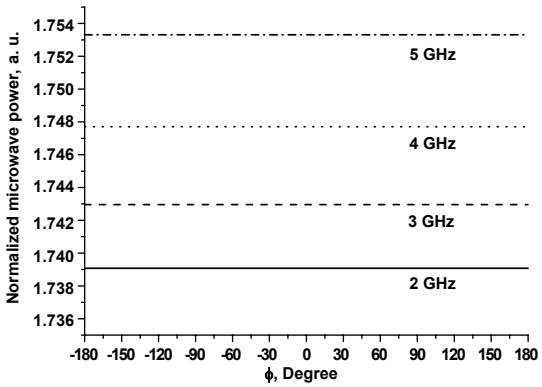

Fig. 16. Dependence of normalized total microwave power $P_\theta(\phi)$ radiated by the "medium"-size microstrip antenna on the polar angle ϕ for various microwave frequencies and for out-of-plane angle $\theta = 0$

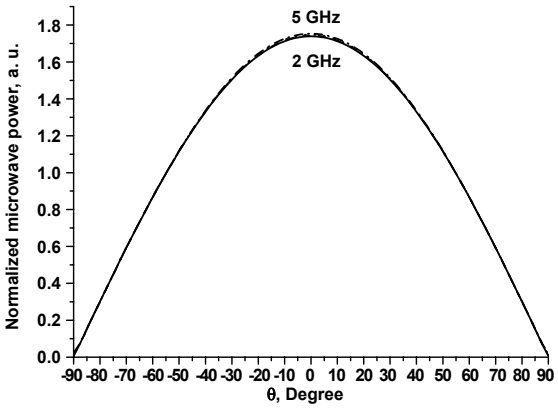

Fig. 17. Dependence of normalized total microwave power $P_\phi(\theta)$ radiated by the "medium" microstrip antenna on the out-of-plane angle θ for various microwave frequencies and for polar angle $\phi = 0$

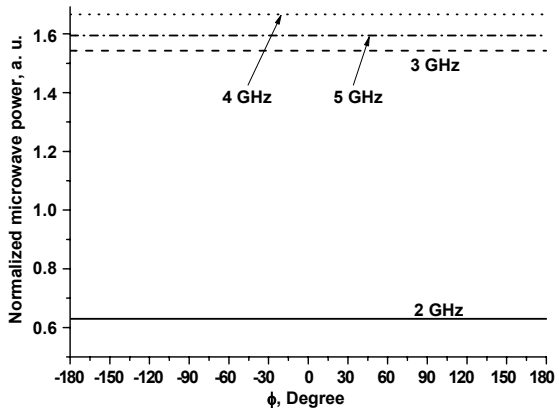

Fig. 18. Dependence of normalized total microwave power $P_\theta(\phi)$ radiated by the "big" microstrip antenna on the polar angle ϕ for various microwave frequencies and for out-of-plane angle $\theta = 0$

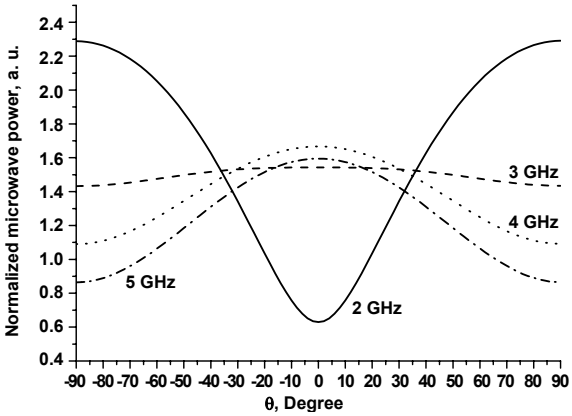

Fig. 19. Dependence of normalized total microwave power $P_\phi(\theta)$ radiated by the "big" microstrip antenna on the out-of-plane angle θ for various microwave frequencies and for polar angle $\phi = 0$

Slot antenna. Slot antenna is the important type of planar antennas. This is the reason why we investigate such type of antenna.

2-D and view of considered slot antenna is shown in Fig. 20, while the performance curves of the antenna are shown in Fig. 21–22, respectively.

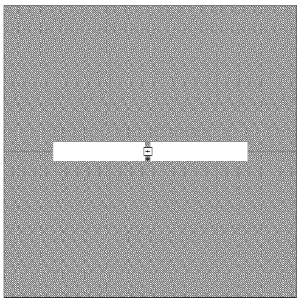

Fig. 20. 2-D image of the topology (top layer) of the considered slot antenna. The size of the structure (size of the black border frame) is 76.2×76.2 mm^2. The dark filled area is the area of metallization. The slit in conductor has a width of 50.8 mm and height of 5.08 mm. The conductor bridge with an excitation port is located at the center of the slit. The topology layer is located above the dielectric layer made of Duroid 6002 ($\varepsilon = 2.96$) with thickness 1.2 mm

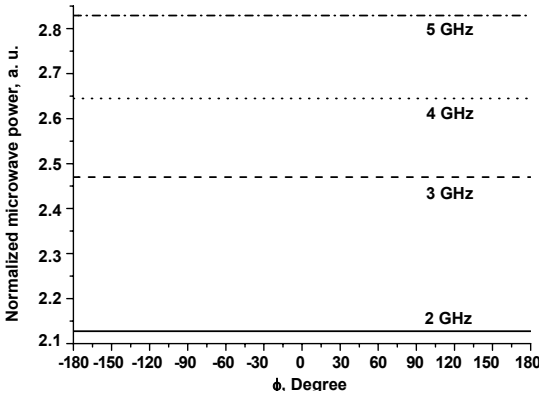

Fig. 21. Dependence of normalized total microwave power $P_\theta(\phi)$ radiated by the slot antenna on the polar angle ϕ for various microwave frequencies and for out-of-plane angle $\theta = 0$

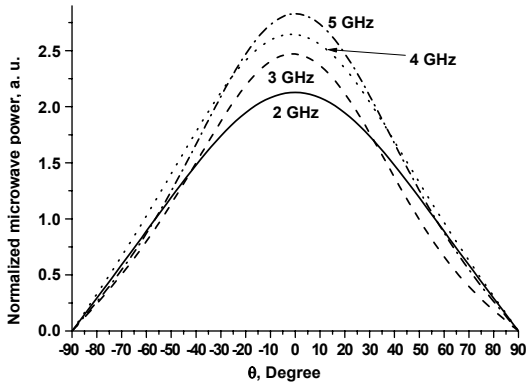

Fig. 22. Dependence of normalized total microwave power $P_\phi(\theta)$ radiated by the slot antenna on the out-of-plane angle θ for various microwave frequencies and for polar angle $\phi = 0$

Square spiral antenna. Square spiral antenna is variation of above considered meander antennas. This antenna can be easily fabricated and by varying the length of the spiral the optimal microwave frequency of the antenna can be changed. Further we analyze the "medium"-size and "big"-size square spiral antennas.

2-D view of considered "medium" and "big" square spiral antenna is shown in Fig. 23, while the performance curves of the antenna are shown in Fig. 24–25. The performance curves of "big"-size antenna are shown in Fig. 26–27, respectively.

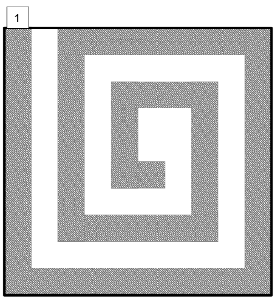

Fig. 23. 2-D image of the topology (top layer) of the considered "medium" and "big" square spiral antenna. The size of the structure (size of the black border frame) is 10×10 mm^2 and 50×50 mm^2. The dark filled area is the area of metallization. Conductor strips has a width of 1 mm and 5 mm, the distance between the strips are 1 mm and 5 mm. Small square with number "1" is the virtual excitation port of the structure. The topology layer is located above the dielectric layer made of Duroid 6002 ($\varepsilon = 2.96$) with thickness 1.2 mm

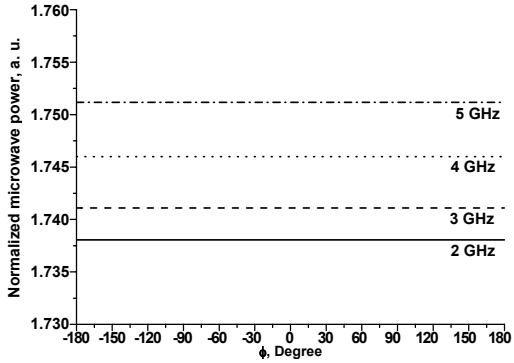

Fig. 24. Dependence of normalized total microwave power $P_\theta(\phi)$ radiated by the "medium" square spiral antenna on the polar angle ϕ for various microwave frequencies and for out-of-plane angle $\theta = 0$

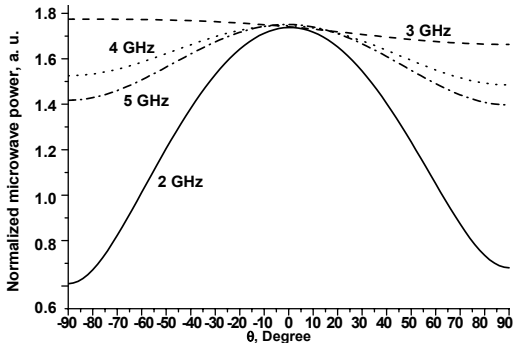

Fig. 25. Dependence of normalized total microwave power $P_\phi(\theta)$ radiated by the "medium" square spiral antenna on the out-of-plane angle θ for various microwave frequencies and for polar angle $\phi = 0$

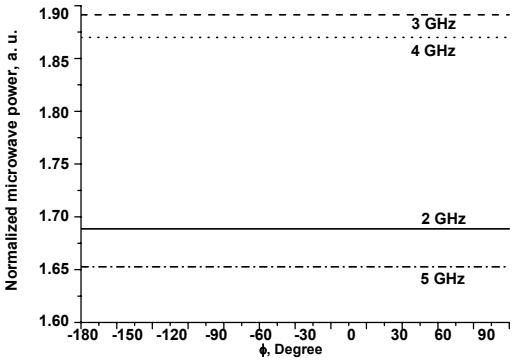

Fig. 26. Dependence of normalized total microwave power $P_\theta(\phi)$ radiated by the "big"-size square spiral antenna on the polar angle ϕ for various microwave frequencies and for out-of-plane angle $\theta = 0$

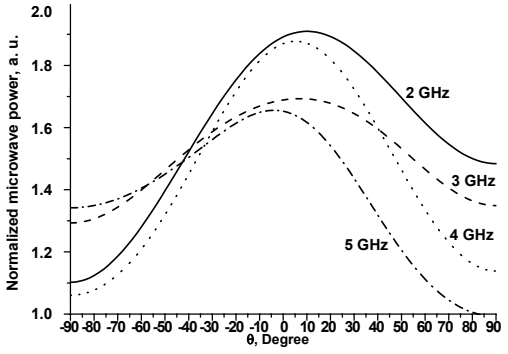

Fig. 27. Dependence of normalized total microwave power $P_\phi(\theta)$ radiated by the "big" square spiral antenna on the out-of-plane angle θ for various microwave frequencies and for polar angle $\phi = 0$

T-like microstrip antenna. The geometry of T-like microstrip antenna is close to the geometry of dipole antenna, that is the reason to analyze such type of antenna.

2-D view of considered T-like antenna are shown in Fig. 28, while the performance curves of the antenna are shown in Fig. 29–30, respectively.

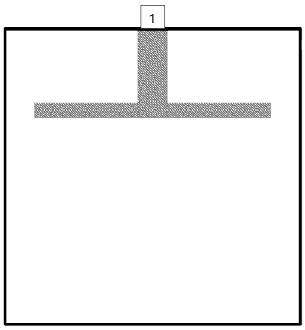

Fig. 28. 2-D image of the topology (top layer) of the T-like microstrip antenna. The size of the structure (size of the black border frame) is 10×10 mm^2. The dark filled area is the area of metallization. Conductor strips has a width of 1 and 0.5 mm. Small square with number "1" is the virtual excitation port of the structure. The topology layer is located above the dielectric layer made of Duroid 6002 ($\varepsilon = 2.96$) with thickness 1.2 mm

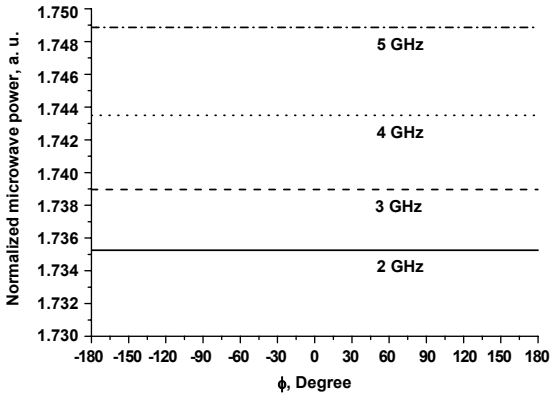

Fig. 29. Dependence of normalized total microwave power $P_\theta(\phi)$ radiated by T-like antenna on the polar angle ϕ for various microwave frequencies and for out-of-plane angle $\theta = 0$

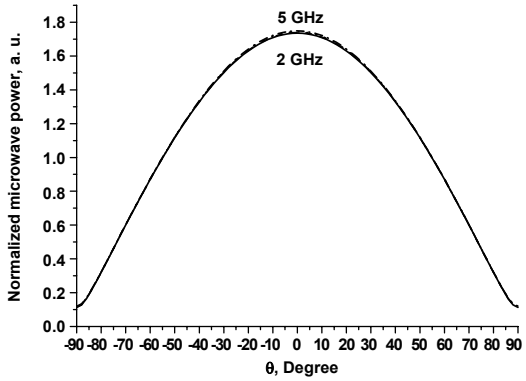

Fig. 30. Dependence of normalized total microwave power $P_\phi(\theta)$ radiated by T-like antenna on the out-of-plane angle θ for various microwave frequencies and for polar angle $\phi = 0$

Endfire antenna. Endfire antennas are widely used in different telecommunication devices [6, 25, 50]. The considered endfire antenna is characterized by large sizes (we use the sizes of real antenna) and three excitation ports, located at the central three strips in the system.

3-D view of considered endfire antenna is shown in Fig. 31, while the performance curves of the antenna are shown in Fig. 32–33, respectively.

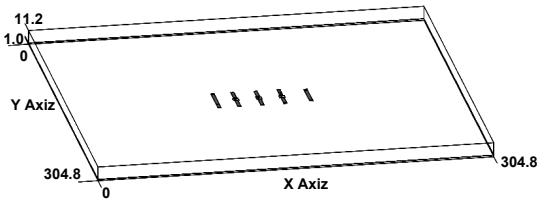

Fig. 31. 3-D image of endfire antenna (all sizes are in millimeters). The size of the structure (size of the black border frame) is 304.8×304.8 mm^2. The dark filled area is the area of metallization. Conductor strips have sizes of 30.48×3.048 mm^2. The strips are located at the center of the structure. Three-port excitation is used for considered endfire antenna. The topology layer is located above the dielectric layer made of Duroid 6002 ($\varepsilon = 2.96$) with thickness 1.2 mm

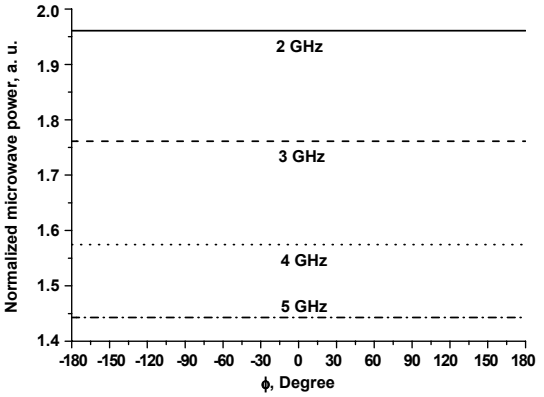

Fig. 32. Dependence of normalized total microwave power $P_\theta(\phi)$ radiated by endfire antenna on the polar angle ϕ for various microwave frequencies and for out-of-plane angle $\theta = 0$

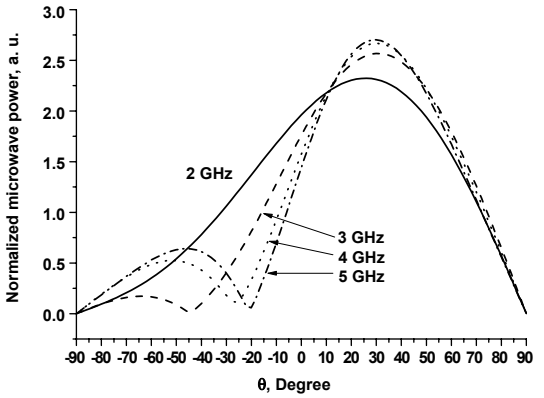

Fig. 33. Dependence of normalized total microwave power $P_\phi(\theta)$ radiated by endfire antenna on the out of-plane angle θ for various microwave frequencies and for polar angle $\phi = 0$

Logarithmic spiral antenna. Logarithmic spiral antennas are well-known in microwave electronics. The considered logarithmic spiral antenna is characterized only by one metallization layer; it is the topology layer.

2-D view of considered antenna is shown in Fig. 34, while the performance curves of the antenna are shown in Fig. 35–36, respectively.

Fig. 34. 2-D image of the topology (top layer) of the logarithmic spiral antenna. The size of the structure (size of the black border frame) is 101.6 × 101.6 mm^2. The dark filled area is the area of metallization. Small square with number "1" is the virtual excitation port of the structure, located at the center of the structure. The topology layer is located above the dielectric layer made of Duroid 6002 ($\varepsilon = 2.96$) with thickness 1.2 mm

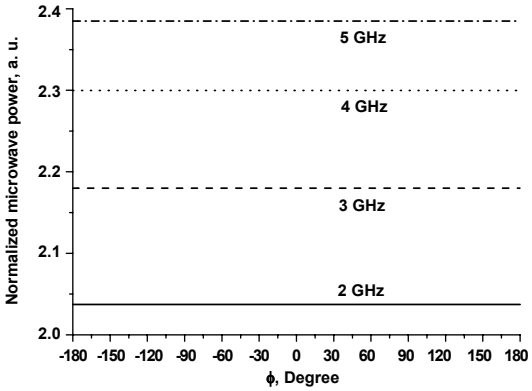

Fig. 35. Dependence of normalized total microwave power $P_\theta(\phi)$ radiated by the logarithmic spiral antenna on the polar angle ϕ for various microwave frequencies and for out-of-plane angle $\theta = 0$

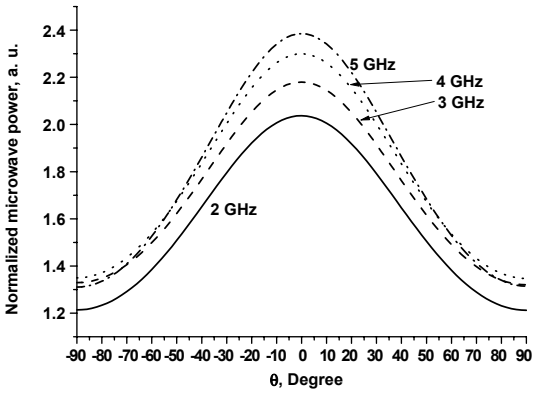

Fig. 36. Dependence of normalized total microwave power $P_\phi(\theta)$ radiated by the logarithmic spiral antenna on the out-of-plane angle θ for various microwave frequencies and for polar angle $\phi = 0$

Patch antenna. Patch antennas are widely used in mobile phones and in other telecommunication devices. That is the reason we analyze the patch antenna.

3-D view of considered antenna is shown in Fig. 37, while the performance curves of the antenna are shown in Fig. 38–39, respectively.

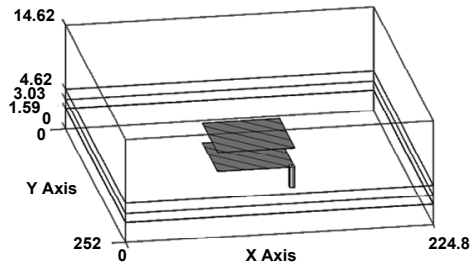

Fig. 37. 3-D image of the patch antenna (all sizes are in millimeters). The size of the structure is 252 × 224.8 mm^2. The dark filled area is the area of metallization. Conductor strips have size of 56.2 × 63 mm^2. There are several dielectric layers in the structure

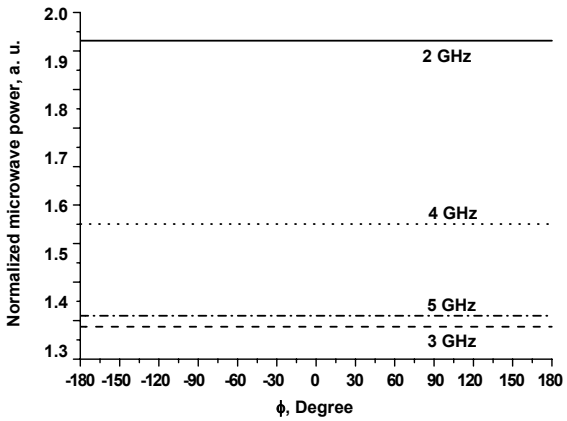

Fig. 38. Dependence of normalized total microwave power $P_\theta(\phi)$ radiated by the patch antenna on the polar angle ϕ for various microwave frequencies and for out-of-plane angle $\theta = 0$

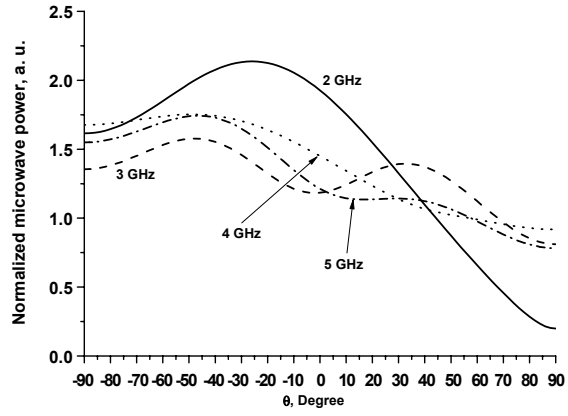

Fig. 39. Dependence of normalized total microwave power $P_\phi(\theta)$ radiated by the patch antenna on the out-of-plane angle θ for various microwave frequencies and for polar angle $\phi = 0$

Window antenna. Window antenna can be considered as the complicated microstrip-slot antenna.

2-D view of considered antenna is shown in Fig. 40, while the performance curves of the antenna are shown in Fig. 41–42, respectively.

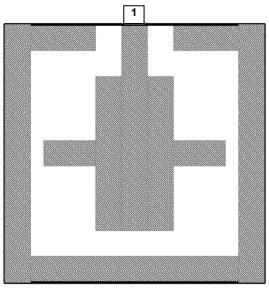

Fig. 40. 2-D image of the topology (top layer) of the window antenna. The size of the structure (size of the black border frame) is 10 × 10 mm^2. The dark filled area is the area of metallization. The border conductor strips have a width of 1 mm. Small square with number "1" is the virtual excitation port of the structure. The topology layer is located above the dielectric layer made of Duroid 6002 (ε = 2.96) with thickness 1.2 mm

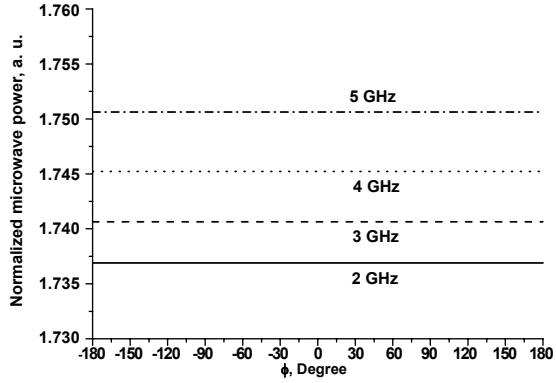

Fig. 41. Dependence of normalized total microwave power $P_\theta(\phi)$ radiated by the window antenna on the polar angle ϕ for various microwave frequencies and for out-of-plane angle $\theta = 0$

Fig. 42. Dependence of normalized total microwave power $P_\phi(\theta)$ radiated by the window antenna on the out-of-plane angle θ for various microwave frequencies and for polar angle $\phi = 0$

Analysis of obtained results. Here is the summary table for the best of all considered antennas:

Antenna	Maximum amplification χ (at frequency)	Out-plane angle θ, degree
Coplanar antenna 10×10 mm^2	1.753 (at 5 GHz)	≈ 0
Coplanar antenna 50×50 mm^2	≈ 1.7 (at 5 GHz) ≈ 2.1 (at 2 GHz)	≈ 0 ≈ 90
Meander antenna 50×50 mm^2	1.94 (at 2 GHz)	≈ 0
Microstrip antenna 50×50 mm^2	≈ 1.6 (at 4 GHz) ≈ 2.3 (at 2 GHz)	≈ 0 ≈ 90
Slot antenna 76×76 mm^2	2.83 (at 5 GHz)	≈ 5
Square spiral antenna 10×10 mm^2	≈ 1.75 (at 5 GHz)	≈ 0

First of all, we have to conclude that the performance of all antennas is not very high, because antenna sizes are smaller (or much smaller) than the characteristic wavelength λ of microwave signal. So, the considered antennas of small sizes can be used only for receiving relatively strong microwave signals, or for transmitting the signals at short distances ~ several λ.

The second specialty is the fact that sensitivity of all considered antennas is increased in most cases (or remains unchanged) if out-plane angle θ is moving towards zero. But in several cases (for example, see "big" coplanar antenna, "big" microstrip antenna, "medium" spiral antenna) antenna sensitivity is increased if the angle θ is also increased. This is happens due to the fact that excitation is better if an electromagnetic power is radiated to the structure through a dielectric substrate, between the bottom and top conductor plates. This is a natural way to excite any planar microstrip system, therefore in these cases the antenna performance is increased if out-plane angle θ is increased. In the other cases the antenna works as an antenna array, so in that case other excitation (and therefore, radiation) mechanisms exist.

The volt-watt sensitivity η of an antenna (voltage V generated by microwave signal divided to the power P of the signal) can be described by the expression:

$$\eta = \frac{V}{P} = \frac{\sqrt{2\chi PZ}}{P} = \sqrt{\frac{2\chi Z}{P}}, \qquad (5)$$

where χ is the amplification coefficient of an antenna and Z is a microwave resistance of an antenna. For perfectly matched antenna Z = Z0 = 377 Ohm. The table of possible values of η and V on the dependence of P is shown below for the case $2\chi = 1$:

P	V	η, V/W
1 mW	614 mV	614
100 uW	194 mV	1940
10 uW	61 mV	6,100
1 uW	19 mV	19,000
100 nW	6 mV	60,000
10 nW	1.9 mV	190,000

So, one can see the considered systems are applicable for creating telecommunication devices with STNOs.

We must also to note that all considered antennas are characterized by a very low dependence of normalized radiated power on in-plane angle ϕ. Due to this circumstance the considered planar antennas can be successfully used for registering electromagnetic signals coming from all (any) directions.

Conclusions. In summary, we analyzed the performance of several microwave planar antennas, which can be used in systems with STNOs. We proved from the numeric calculations that these antennas have high enough performance and can be used for creation of telecommunication devices based on STNOs. We suppose these devices can provide the dc output voltage of several mV for microwave output power of several nW from a single STNO. We also suppose that the best of considered antennas could be a coplanar antenna due to the simplicity of matching with STNO and some technological advantages.

1. *Ablowitz M. J., Hoefer M. A., Ilan B., Pufall M. R. and Silva T. J.* Theory of magnetodynamics induced by spin torque in perpendicularly magnetized thin films // Phys. Rev. Lett. –2005. – Vol. 95. – P. 2676206., 2. Adaptive antennas and receivers/ Ed. by M. M. Weiner. – CRC Press, NY, 2005., 3. *Albert F. J., Buhrman R. A., Katine J. A. and Ralph D. C.* Spinpolarized current switching of a Co thin film nanomagnet // Appl. Phys. Lett. –2000. – Vol. 77. – P. 3809–3811., 4. *Albert F. J., Buhrman R. A., Katine J. A., Myers E. B. and Ralph D. C.* Current-driven magnetization reversal and spin-wave excitations in Co/Cu // Phys. Rev. Lett. –2000. – Vol. 84. – P. 3149–3152., 5. *AlHajDarwish M., Covington M., Ding Y., Gokemeijer N. J. and Seigler M. A.* Current-induced magnetization dynamics in current perpendicular to the plane spin valves// Phys. Rev. B. – 2004. – Vol. 69. – P. 184406.,6. Antenna Handbook: Volume III Antenna applications / Ed. By Y. T. Lo, S. W. Lee. – Springer, NY, 1993., 7. *Bankowski E., Gerhart G., Tiberkevich V. and Slavin A.* Phase-locking and frustration in an array of nonlinear spin-torque nano-oscillators // Appl. Phys. Lett. – 2009. – Vol. 95. – P. 262505.

8. *Bankowski E., Meitzler T., Prokopenko O., Tiberkevich V., and Slavin A.* Spin-torque nano-oscillator as a microwave signal source// submitted to IEEE Magn. Letters. – 2010. 9. *Bass J., Chiang W. C., Jansen A. G. M., Seck M., Tsoi M., Tsoi V., and Wyder P.* Excitation of a magnetic multilayer by an electric current // Phys. Rev. Lett. – Vol. 80. – P. 4281–4284. 10. *Bass J., Chiang W. C., Jansen A. G. M., Tsoi M., Tsoi V., and Wyder P.* Generation and detection of phase-coherent current-driven magnons in magnetic multilayers // Nature – 2000 – Vol. 406. – P. 46–48. 11. *Bass Jr. and J., Birge N. O., Pratt W. P., Urazhdin S.* Current-Driven Magnetic Excitations in Permalloy-Based Multilayer Nanopillars // Phys. Rev. Lett. – 2003. – Vol. 91. – P. 146803. 12. *Berger L.* Emission of spin waves by a magnetic multilayer traversed by a current // Phys. Rev. B. – 1996. – Vol. 54. – P. 9353–9358. 13. *Boone C. T., Cheng X., Childress J. R., Katine J. A., Krivorotov I. N., Tiberkevich V., Slavin A. and Zhu J.* Resonant nonlinear damping of quantized spin waves in ferromagnetic nanowires: a spin torque ferromagnetic resonance study // Phys. Rev. Lett. –2009. – Vol. 103. – P. 167601. 14. *Boone C. T., Cheng X., Krivorotov I. N. and Zhu J.* Nonadiabatic stochastic resonance of a nanomagnet excited by spin torque // Phys. Rev. Lett. – 2001. – Vol. 105. – P. 047202. 15. *Bouzehouane K., Cros V., Deranlot C., Dussaux A., Fert A., Fusil S., Georges B., Grollier J., Guillemet R. and Ruotolo A.* Phase-locking of magnetic vortices mediated by antivortices // Nature Nanotech. –2009. – Vol. 4.– P. 528–532. 16. *Braganca P. M., Buhrman R. A., Garcia A. G. F., Krivorotov I. N., Ralph D. C. and Sankey J. C.* Spin-transfer-driven ferromagnetic resonance of individual nanomagnets // Phys. Rev. Lett. – 2006. – Vol. 96. – P. 227601. 17. *Brunet M., Cyrille M.-C., Dieny B., Delaët B., Ebels U., Firastrau I., Houssameddine D., Michel J.-P., Ponthenier F., Prejbeanu-Buda L., Redon O., Rodmacq B. and Thirion C.* // Spin-torque oscillator using a perpendicular polarizer and a planar free layer// Nature Mater. –2007. – Vol. 6 – P. 447–453. 18. *Buhrman R. A., Cui Y.-T., Katine J. A., Ralph D. C., Sun J. Z. and Wang C.* Sensitivity of spin-torque diodes for frequency tunable resonant microwave detection // J. Appl. Phys. – 2009. – Vol. 106. – P. 053905. 19. *Buhrman R. A., Emley N. C., Garcia A. G. F., Kiselev S. I., Krivorotov I. N., Ralph D. C. and Sankey J. C.* Spin-transfer excitations of permalloy nanopillars for large applied currents // Phys. Rev. B. – 2005. – Vol. 72. – P. 064430. 20. *Buhrman R. A., Emley N. C., Kiselev S. I., Krivorotov I. N., Perez C., Ralph D. C., Rinkoski M. and Sankey J. C.* Current-induced nanomagnet dynamics for magnetic fields perpendicular to the sample plane// Phys. Rev. Lett. – 2004. – Vol. 93. – P. 036601. 21. *Buhrman R. A., Emley N. C., Kiselev S. I., Krivorotov I. N., Ralph D. C., Sankey J. C. and Schoelkopf R. J.* Microwave oscillations of a nanomagnet driven by a spin-polarized current // Nature. – 2003. – Vol. 425. – P. 380–383. 22. *Buhrman R. A., Emley N. C., Kiselev S. I., Krivorotov I. N., Ralph D. C. and Sankey J. C.* Time-domain measurements of nanomagnet dynamics driven by spin-transfer torques // Science. – 2005. – Vol. 307. – P. 228–231. 23. *Buhrman R. A., Katine J. A., Louie R. N., Myers E. B. and Ralph D. C.* Current-induced switching of domains in magnetic multilayer devices // Science. – 1999. – Vol. 285. – P. 867–870. 24. *Chen Z. N., Chia M. Y. W.* Broadband Planar Antennas: Design and Applications. – Wiley, NY, 2006. 25. *Chen Z. N., Luk K.-M.* Antennas for Base Stations in Wireless Communications. – McGraw-Hill Professional, NJ, 2009. 26. Computer techniques for electromagnetics / Ed. by R. Mittra. – Pergamon Press, Oxford, 1973. 27. *Cros V., Fert A., Georges B. and Grollier J.* Impact of the electrical connection of spin transfer nano-oscillators on their synchronization: an analytical study // Appl. Phys. Lett. –2008. – Vol. 92. – P. 232504. 28. *Deac A., Dieny B., Nozières J.-P., Lee K. J. and Redon O.* Excitations of incoherent spin waves due to spin-transfer torque // Nature Mater. – 2004. – Vol. 3. – P. 877–881. 29. *Djayaprawira D. D., Fukushima A., Kubota H., Maehara H., Suzuki Y., Tsunekawa K., Tulapurkar A. A., Yuasa S. and Watanabe N.* Spintorque diode effect in magnetic tunnel junctions // Nature. – 2005. – Vol. 438. – P. 339–342. 30. Encyclopedia of Rf and Microwave Engineering, 6-volume set/ Ed. by K. Chang. – Wiley, Interscience, NY, 2005. 31. *Engel B. N., Mancoff F. B., Rizzo N. D. and Tehrani S.* Area dependence of high-frequency spin-transfer resonance in giant magnetoresistance contacts up to 300 nm diameter // Appl. Phys. Lett. – 2006. – Vol. 88. – P. 112507. 32. *Engel B. N., Mancoff F. B., Rizzo N. D. and Tehrani S.* Phase-locking in double-point-contact spin-transfer devices // Nature. – 2005. – Vol. 437. – P. 393–395. 33. *Fenn A. J.* Adaptive Antennas and Phased Arrays for Radar and Communications: Artech House Radar Library. – Artech House, Inc., Toronto, 2007. 34. *Fullerton E. E. and Katine J. A.* Device implications of spin-transfer torques // J. Magn. Magn. Mater. – 2008. – Vol. 320, № 7. – P. 1217–1226. 35 *Gaucher B., Grzyb J., Liu D., Pfeiffer U.* Advanced millimeter-wave technologies: antennas, packaging and circuits. – Wiley, Toronto, 2009. 36. *Grau A., Flaviis F. D., Jofre L., Romeu J.* Multiantenna systems for MIMO Communications. – Morgan & Claypool, Singapore, 2006. 37. *Johnson R. C.* Antenna engineering handbook:third edition. – McGraw-Hill, St. Lois, 1993. 38. *Joseffson L., Persson P.* Conformal antenna array theory and design / IEEE Press series on electromagnetic wave theory. – Wiley, IEEE Press, NJ, 2006. 39. *Kaka S., Pufall M. R., Rippard W. H., Russek S. E. and Silva T. J.* Direct-current induced dynamics in Co90Fe10/Ni80Fe20 point contacts // Phys. Rev. Lett. – Vol. 92. – P. 027201. 40. *Kaka S., Pufall M. R., Rippard W. H., Russek S. E. and Silva T. J.* Current-driven microwave dynamics in magnetic point contacts as a function of applied field angle // Phys. Rev. B. – 2004. – Vol. 70. – P. 100406. 41. *Kumar G., Ray K. P.* Broadband microstrip antennas. – Artech House, Inc., NY, 2003. 42. *Kurths J., Pikovsky A. and Rosenblum M.* Synchronization: a universal concept in nonlinear sciences. – University Press, Cambridge, 2007. 43. *Li Y. C., Yang Z., and Zhang S.* Chaotic dynamics of spin-valve oscillators // Phys. Rev. Lett. – 2007. – Vol. 99. – P. 134101. 44. *Ma M.T.* Theory and Application of Antenna Arrays. – John Wiley & Sons Inc, NY, 1974. 45. *Mailloux R. J.* Phased Array Antenna Handbook: Second Edition. – Artech House, Inc., NJ, 2005. 46. *Pufall M. R., Rippard W. H. and Silva T. J.* Quantitative studies of spin-momentum-transfer-induced excitations in Co // Appl. Phys. Lett. – 2003. – Vol. 82. – P. 1260–1262. 47. *Ralph D. C., Stiles M. D.* Spin transfer torques // J. Magn. Magn. Mater. – 2008. – Vol. 320. – P. 1190–1216. 48. Reliability and Key Properties of RT/duroid® 6002, web link: http://secomtel.com/UpFilesPDF/PDF/ROGERS/rt294.pdf 49. RT/duroid®6002 High Frequency Laminates, web-link: www.rogerscorporation.com 50. *Saunders S. N., Zavala A. A.* Antennas and propagation for wireless communication systems: Second edition. – Wiley, Toronto, 2007. 51. *Slavin A. and Tiberkevich V.* Nonlinear auto-oscillator theory of microwave generation by spin-polarized current // IEEE Trans. on Magn. – 2009. – Vol. 45, № 4. – P. 1875–1918. 52. *Slavin A. N. and Tiberkevich V. S.* Nonlinear self-phase-locking effect in an array of current-driven magnetic nanocontacts // Phys. Rev. B. – 2005. – Vol. 72. – P. 092407. 53. *Slavin A. N. and Tiberkevich V. S.* Theory of mutual phase locking of spin-torque nanosized oscillators // Phys. Rev. B. – 2006. – Vol. 74. – P. 104401. 54. *Slonczewski J. C.* Current-driven excitation of magnetic multilayers // J. Magn. Magn. Mater. – 1996. – Vol. 159. – P. L1–L7. 55. *Sun J. Z.* Current-driven magnetic switching in manganite trilayer junctions// J. Magn. Magn. Mater. – 1999. – Vol. 202. – P. 157–162. 56. The ARRL Antenna Book 21th edition/ Ed. by L. B. Cebik, D. Hallidy and D. R. Straw. – American Radio Relay League, NY, 2007. 57. *Tsoi M.* Phase-coherent current-driven magnons in magnetic multilayers // J. Magn. Magn. Mater. – 2002. – Vol. 240. – P. 103–107. 58. *Visser H.* Array and Phased Array Antenna Basics. – John Wiley & Sons, NY, 2005. 59. *Volakis J. L.* Antenna engineering handbook: fourth edition. – McGraw-Hill, NY, 2007.

Submitted 19.11.10

UDC 539.186.2

V. Vysotskii, Dr. Sci.,
V. Rydenky, stud.

EXCITATION OF QUANTUM OBJECT WITH INNER STRUCTURE DUE TO ACCELERATION

Застосовано теорію нестаціонарних збурень для обчислення імовірності переходу квантової системи внаслідок її прискорення. Отримано критерій для обмеження розгляду першим порядком теорії збурень.

Ключові слова: теорія збуреннь, збудження, перехід, прискорення

Non-stationary perturbation theory applied to calculate the probability of excitation of quantum object due to an arbitrary acceleration. Detailed treatment shows that limitation with first order of perturbation is accurate enough.

Key words: perturbation theory, excitation, transition, acceleration

Introduction. Challenge of formation of exited states of atomic and nuclear systems pretend to acquire great priority in a field of quantum radiophysics and nuclear physics. It may be useful for creation of new types of laser systems with optimized methodology of atom or nuclear excitation. Side by side with traditional way of excitation (resonance and non-resonance pumping, ionization-recombination mechanism of excitation due to intense heating and rapid cooling of plasma, coulomb excitation due to inelastic scattering of charged particles on atoms and nuclei) new ways of excitation due to collision of particles with inner structure and non-charged particles are used. New methods are based on non-stationary perturbation theory, but researchers paid much attention to the adiabatic evolution and instantaneous acceleration. An intermediate case needs more careful treatment [3]. An analogical problem arises in an inverse problem of detecting moving particles or detecting a perturbation field by known rates coefficients of excitation. In this issue probability calculation method for arbitrary rate of acceleration is proposed.

Background. There are several methods described in a literature to calculate the probability of excitation of atoms due to acceleration of a nuclear. All of them are based on assumption that the electrons and nuclear changed their velocity during interval of time less than characteristic time of internal electron shell process. This called instantaneous way of acceleration. This means that the spatial electronic wave function after acceleration process acquires form:

$$\Psi(\vec{r}) = \Psi_n(\vec{r}) \exp(-i\mu\vec{v}\vec{r}/\hbar)$$

Here $\vec{v},\mu$ – acquired velocity and mass of the electron respectively. The next step is to decompose this wavefuntion into basic electron functions of atomic Hamiltonian's operator. Probability of the n-m level transition equals:

$$W_{nm} = \left|\langle \Psi_n \left| \exp(-i\mu\vec{v}\vec{r}/\hbar) \right| \Psi_m \rangle\right|^2$$

In a hydrogen atom transition from state with quantum numbers 100 to state with quantum numbers 210 has probability equals to [4]:

$$W_{100,210} = \frac{72(v/v_{100})^2}{[(v/v_{100})^2 + 9/4]^2}$$

On the other hand, the theorem about adiabatic changes states that acceleration applied during time interval greater than characteristic time of internal electron shell process do not cause any transitions of the electron in an atom. The characteristic time of changes of electron subsystem of the atom equals to $1/\omega_{nm}, \omega_{nm}$, the transition frequency. For the electron transition from state 1s0 (100) to state 2s0 (210) in hydrogen atom characteristic time approximately equals $10^{-14} s$. Clearly to understand that there is no such a quick mechanical process to accelerate atom during this time frame. A relatively large time frame of acceleration of an atom is a new challenge to calculate probability of transition due to mechanical influence.

Application of non-stationary perturbation theory to atom excitation. Below discussed treatment are based on non-stationary perturbation method in terms of an acceleration of atom system. Acceleration is rarely used in quantum mechanics but sometimes it can be useful to describe coupling with other quantum system. The treatment begins with non-stationary of Schrödinger equation. We consider $\hat{R}(t) = \vec{e}_z z(t)$ being a nuclear position of atom in laboratory system.

$$i\hbar\frac{\partial\Psi(\vec{r},t)}{\partial t} = -\frac{\hbar^2}{2\mu}\Delta\Psi(\vec{r},t) + U(\vec{r}-\vec{R}(t))\Psi(\vec{r},t)$$

To obtain Hamiltonian eigenfunction separation of translator motion and internal wave function is needed. To reach this we need Schrödinger equation to be depicted in the intrinsic frame of reference of atom

For the separation of internal processes and translation motion we use substitution [1]:

$$\Psi(\vec{\xi},t) = \phi(\vec{\xi},t)\exp\{\frac{i}{\hbar}\mu\vec{v}(t)\vec{\xi} - \frac{i}{\hbar}\int_0^t \frac{\mu v(\tau)^2}{2} d\tau\}$$

After substitution and some transformation Schrödinger equation acquire following form.

$$i\hbar\frac{\partial\phi(\vec{\xi},t)}{\partial t} = -\frac{\hbar^2}{2\mu}\Delta\phi(\vec{\xi},t) + U(\vec{\xi})\phi(\vec{\xi},t) + \mu\vec{\xi}\vec{a}(t)\phi(\vec{\xi},t).$$

Here $\vec{a}(t)$ acceleration of atom due external influence. We consider additional potential $V(\vec{\xi},t) = \mu\vec{\xi}\vec{a}(t)\phi(\vec{\xi},t)$ to be small compared with a potential $U(\vec{\xi})$. This fact courses to use a non-stationary perturbation theory. For more general treatment we are going to use non-stationary perturbation theory in operator form. Let $\hat{\hat{S}}_0$, $\hat{\sigma}$ be unitary operator evolution for atom Hamiltonian and intrinsic evolution operator caused by perturbation potential respectively. To calculate operator $\hat{\sigma}$ we need solve operator equation $i\hbar\frac{d\sigma}{dt} = \mu\vec{a}(t)\hat{S}_0^+\vec{\xi}\hat{S}_0\hat{\sigma}$

Formal solution with initial condition $\hat{\sigma}(0) = 1$ can be depicted in form of time ordered exponential.

$$\hat{\sigma}(t) = \hat{T}\exp(-\frac{i}{\hbar}\int_0^t \mu\vec{a}(\tau)\hat{S}_0^+\vec{\xi}\hat{S}_0\hat{\sigma}d\tau)$$

Matrix element of operator $\hat{\sigma}$ represents probability of atomic transition $W_{nm} = \left|\langle\Psi_n\left|\hat{\sigma}(t)\right|\Psi_m\rangle\right|^2$. Let $X_{nm} = \langle\Psi_n\left|z\right|\Psi_m\rangle$ than for first order of non-stationary perturbation theory and acceleration $\vec{a}(t) = \{0,0,a(t)\}$ can be depicted as.

$$W_{nm}^{(1)}(t) = \frac{\mu^2\left|X_{nm}\right|^2}{\hbar^2}\left|\int_0^t a(\tau)\exp[i\omega_{nm}\tau]d\tau\right|^2.$$

Application of method. Above results can be used to calculate probability of instantaneous way of acceleration. We consider electronic transition 100 to 210 in a hydrogen atom due to instantaneous perturbation potential (let $\vec{a} = \{0,0,a\}$) $V(t) = \mu a z\delta(t)$. Evolution operator should be calculated as a sum of infinite series:

$$\hat{\sigma} = \sum_{n=0}^{\infty}\frac{\mu^n a^n}{n!(i\hbar)^n}\int_0^t\ldots\int_0^{t_n}\delta(\tau_1)\hat{S}_0^+ z\hat{S}_0 * \ldots * \delta(\tau_n)\hat{S}_0^+ z\hat{S}_0 d\tau_1\ldots d\tau_n$$

After summarization we get an explicit form of operator $\hat{\sigma} = \exp(-i\mu vz/\hbar)$. Probability of transition from quantum state 100 to quantum state 210 in hydrogen atom can be calculated as a matrix element of above operator.

$$W_{100,210} = \left|\langle\Psi_{210}\left|\hat{\sigma}\right|\Psi_{100}\rangle\right|^2 = \frac{72(v/v_{100})^2}{[(v/v_{100})^2 + 9/4]^2}$$

As we shown, non-stationary perturbation method can be used to calculate instantaneous way of atom excitation exactly. The first order of expansion above formula over powers of $(v/v_{100})^2$ corresponds to first order of non-stationary perturbation theory. Because of a relativistic limitation of an atom velocity first order can be exact enough.

Proposed method incorporates conclusions of theorem about adiabatic system evolution [2, p. 517–521]. If acceleration changes more slowly than characteristic time of internal atomic processes $T_{nm} = 1/\omega_{nm}$ than in first order of theory integral $\left|\int_0^t a(\tau)\exp[i\omega_{nm}\tau]d\tau\right|^2$ vanishes, because of integral over multiplication of slowly varying and quickly oscillating functions. The higher orders can be dominated by high powers of such integrals. This means that high orders vanish to. Taking to account all orders of non-stationary perturbation theory does not change that fact that relatively slowly varying acceleration does not cause any transitions.

Let consider acceleration in a form of $\vec{a} = \{0,0,a_0\exp(-\frac{t}{\tau})\}$. Probability of transition in a hydrogen atom from quantum state 100 to quantum state 210 equals

$$W_{100,210} = \frac{\left|X_{100,210}\right|^2 a_0^2\mu^2}{\hbar^2}\frac{\tau^2}{(1+\omega_{100,210}^2\tau^2)}.$$

It is estimated around ($\tau = 10^{-9} s$ at the edge of duration of mechanical processes in typical cases) $10^{-43}a_0^2$ (here a_0 in m/s^2 units). Estimated probability is very tiny because of relatively slow duration of acceleration applied on atom.

Discussion about accuracy of first order of non-stationary perturbation treatment. It is safe enough to limit our consideration with first order perturbation theory if the next order is much less than previous one. In hydrogen atom during dipole allowed transitions only odd orders of perturbation series exist. Applying technique of majorant we can get the criterion of limiting ourselves with first order:

$$v(t) << v_{100}\sqrt{3!\left|X_{nm}\right|/\left|(X^3)_{nm}\right|}$$

In hydrogen atom 1s→2p0 transition we have $v(t) << 0.8v_{100}$. It too severe limitation in a practical situations we can consider much more velocities. It is more correct to require that $\mu a_{\max} |X_{nm}| / \hbar\omega_{nm} << 1$. For hydrogen atom 1s→2p0 transition $a_{\max} << 10^{22}$. It is correct to limit treatment with first order of non – stationary perturbation theory because of great limiting value of velocity or acceleration.

Conclusions. An excitation of quantum object with inner structure due to acceleration was investigated. Proposed method includes previously known results for adiabatic evolution and instant acceleration. Results cover an intermediate case between adiabatic evolution and excitation due to instant acceleration. Detailed treatment shows that limitation with first order of perturbation is accurate enough.

1. *Greenberg D.* Inadequacy of usual Galilean transformation in quantum mechanics // Phys. Rew. – 2001. – Vol. 87, № 10. 2. *Бом М.* Квантовая теория – М., 1980. 3. *Корнилова А., Высоцкий В., Сысоев Н.,* и др. Ударно – кавитационный механизм генерации рентгеновского излучения при кавитации быстрой струи воды // ВМУ. Физика. Астрономия. – 2010. – № 1. 4. *Корнилова А., Высоцкий В., Сысоев Н.,* и др. Генерация рентгеновского излучения при пузырьковой кавитации быстрой струи жидкости в диэлектрических каналах // Поверхность. Рентген., синхротрон. и нейтрон. исслед. – 2009. – № 4.

Submitted 15.11.10

UDC 535. 36

A. Ivanisik, Ph. D.,
O. Isaienko, post grad. stud.,
O. Sereduyk, stud.

THE INFLUENCE OF DIELECTRIC MEDIUM ON THE INTENSITY OF SURFACE-ENHANCED RAMAN SCATTERING LINES

У роботі досліджено вплив діелектричної проникності середовища на ефективність явища гігантського комбінаційного розсіяння світла молекулами, що розташовані на поверхні сферичних наночастинок. Розглянуті наночастинки металів Ag, Cu і Au. Показано частинки якого металу більш ефективно підсилюють комбінаційне розсіяння. Порівняно гігантське комбінаційне розсіяння з наночастинками металів у середовищі та у вакуумі. Зокрема, з'ясована залежність коефіцієнта підсилення комбінаційного розсіяння від довжини хвилі при різних параметрах середовища: діелектричної проникності, приведеної сили осцилятора, сталої загасання осцилятора, яка визначає ширину спектральної лінії поглинання.

Ключові слова: гігантське комбінаційне розсіювання, наночастинка, дисперсійна залежність, діелектрична проникність.

This article studies the dielectric medium influence on the efficiency of surface-enhanced Raman scattering of light by molecules, which are disposed at surface of spherical nanoparticles. Metal nanoparticles of Ag, Cu, and Au are considered. It is shown which metal particles enhance Raman scattering more efficiently. Surface-enhanced Raman scattering with metal nanoparticles is compared in the media and in the vacuum. In particular, the dependence of Raman scattering gain on wavelength is found out under different medium parameters: dielectric permittivity, reduced oscillator strength, oscillator damping constant which define the width of a spectral line in absorption.

Keywords: surface-enhanced Raman scattering, nanoparticle, dispersion, dielectric permittivity.

Introduction. Raman spectroscopy is a powerful method of analysis and studying the molecules composition and structure. However, detection of Raman scattering, which is a two-photon process, is technically complicated and requires sophisticated equipment and precise optimization of experimental conditions. Surface-enhanced Raman scattering is one of the methods to increase the spectral lines intensity. It allows to record spectra under concentrations which are by several orders of magnitude smaller than when traditional Raman spectroscopy is used. This is important, as large number of biological compounds is found in limited concentrations.

This work aim was to study the dielectric medium influence on the efficiency of surface-enhanced Raman scattering of light by molecules, which are disposed at surface of spherical metal nanoparticles of Ag, Cu, and Au.

Development and discussion. Surface-enhanced Raman scattering is the effect that shows up to many times increase in Raman scattering spectrum lines intensity by the molecules absorbed on the noble metal surface (e. g. Ag, Au) [1]. But physical mechanism of such enhancement of Raman scattering is not fully ascertained yet. It is determined, that the full gain in lines intensity depends on two factors. One of them perhaps is related to changes in polarization of molecule and to interaction with electrons in metal. When a molecule approaches the metal surface, its electronic energy levels expand and converge. With adsorption involved, a new chemical bond may be created, as well as a new molecule, with its electronic spectrum, consisting of not only initial molecule energy levels, but also of a new energy level, that relates to the charge transfer between the molecule and the metal. This energy level is significantly broader, it increases interaction between molecule electrons and metal electrons and is called the charge transfer band. If this band is located in the visible spectral region, the metal-molecular complex is excited by resonant pumping. Thus, the new molecule gains Raman polarization, and line intensity significantly increases [2, 3]. In this article we don't take into consideration such physical mechanism.

The other factor that can produce increase of more than 103 times is related to the electric field increase, acting on a molecule near the metal surface. This gain is caused by incident electromagnetic radiation resonance with plasmon oscillations of electrons, localized near the metal surface [4].

Small spherical particles were considered, which can serve as a model of rough surface with permittivity ε_1, that is a complex frequency-dependent metallic dielectric constant. Field intensity on the sphere surface was determined as:

$$E_{\text{sphere surface}} = \frac{\varepsilon_1 - \varepsilon_2}{\varepsilon_1 + 2\varepsilon_2} E_{\text{incident radiation}}, \qquad (1)$$

where ε_2 is a medium permittivity. Complex permittivity can be given as

$$\varepsilon_1 = \varepsilon_1^{'} + i\varepsilon_2^{''}, \qquad (2)$$

where $\varepsilon_1^{'}$ and $\varepsilon_2^{''}$ are real and imaginary parts of permittivity value.

Metals have a frequency range where the permittivity real part is less than zero: $\varepsilon_1^{'}(\omega) < 0$. In this case, the equality $\varepsilon_1^{'} = -2\varepsilon_2$ is gained at the certain, so called "resonant", frequency and the resulting field intensity near the sphere surface increases dramatically.

To study surface-enhanced Raman scattering effect on the metal particles surface in the media, a physical model was used, that is suggested by Kerker [5], who reviewed the uniformly polarized sphere field. The total increase is a multiplication of the pumping field enhancement at the frequency ω_1 and Raman field enhancement at the frequency ω_2:

$$G = \left| \left(1 + 2\frac{\varepsilon_1(\omega_1) - \varepsilon_2(\omega_1)}{\varepsilon_1(\omega_1) + 2\varepsilon_2(\omega_1)}\right) \left(1 + 2\frac{\varepsilon_1(\omega_2) - \varepsilon_2(\omega_2)}{\varepsilon_1(\omega_1) + 2\varepsilon_2(\omega_2)}\right) \right|^2. \qquad (3)$$

Real and imaginary parts of permittivity are $\varepsilon_1' = n^2 - k^2$ and $\varepsilon_1'' = 2nk$, where n and k are real and imaginary parts of refractive indices measured by Johnson and Christy for Ag, Cu, and Au [6]. For medium we use dispersive equation in standard form:

$$\varepsilon_2 = \varepsilon^{\infty} + \frac{S\omega_0^2}{\omega_0^2 - \omega^2 + i\omega\Gamma}, \qquad (4)$$

where ε^{∞} is permittivity at the infinite frequency, ω_0 – resonant frequency, $S = f\,\omega_p^2 / \omega_0^2$ – a dimensionless quantity, which characterizes the interaction strength between the oscillator and the electromagnetic wave, it is called "reduced oscillator strength", f – oscillator strength, ω_p – plasma frequency, Γ – damping constant [7].

The gain dependence on exciting light frequency ω_1 and the Raman shift $(\omega_1 - \omega_2)$ is given by (3). Only one maximum value is observed for Ag, Cu, and Au in the case when complex part of dielectric medium permittivity ε_2'' equals zero. These maximum values G_{1max} dependences on the permittivity $\varepsilon_2 = \varepsilon_2' = \varepsilon^{\infty}$ are presented in Fig. 1. The Raman shift was 100 cm^{-1}. It is obvious from these results, that all particles are providing some influence on Raman scattering and in the relevant wavelength range they can amplify scattering signals.

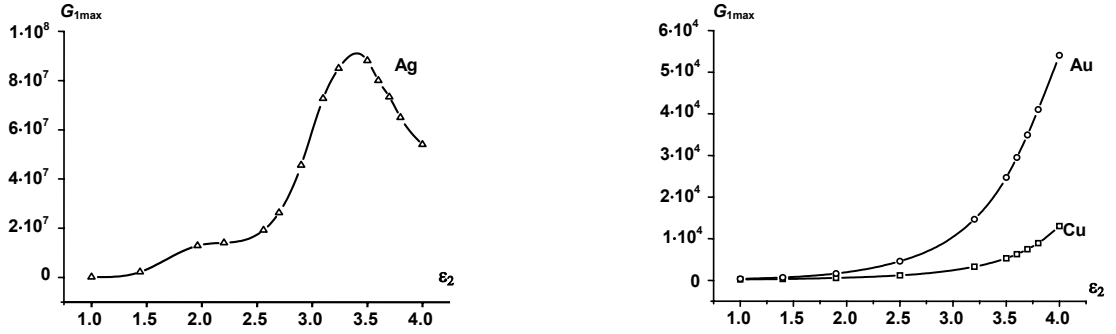

Fig. 1. The gain G_{1max} dependence on medium permittivity for Ag, Au and Cu

While permittivity increases in nonabsorbable media, Raman scattering is increasing as well for different metal particles. Significant amplification is observed while using silver particles. Among the most effective metals, studied by the theoretical calculations, silver revealed the strongest gain. That is why silver particles are of special interest and should be used to substantially increase the Raman scattering lines gain.

In absorbable media we selected reduced oscillator strength $S = 0.1$, damping constant $\Gamma = 0.01 \cdot \omega_0$, $\lambda_0 = 2\pi c / \omega_0 = 550$ nm, permittivity at the infinite frequency $\varepsilon^{\infty} = 1.33^2$ and the Raman shift $(\omega_1 - \omega_2)/(2\pi c) = 100$ cm^{-1}, at which the significant gain is obtained, and also compared with amplification in the vacuum. The second maximum G_{2max} appears while using silver particles. Figure 2 shows the G dependence on wavelength $\lambda_1 = 2\pi c / \omega_1$ in the medium and the vacuum.

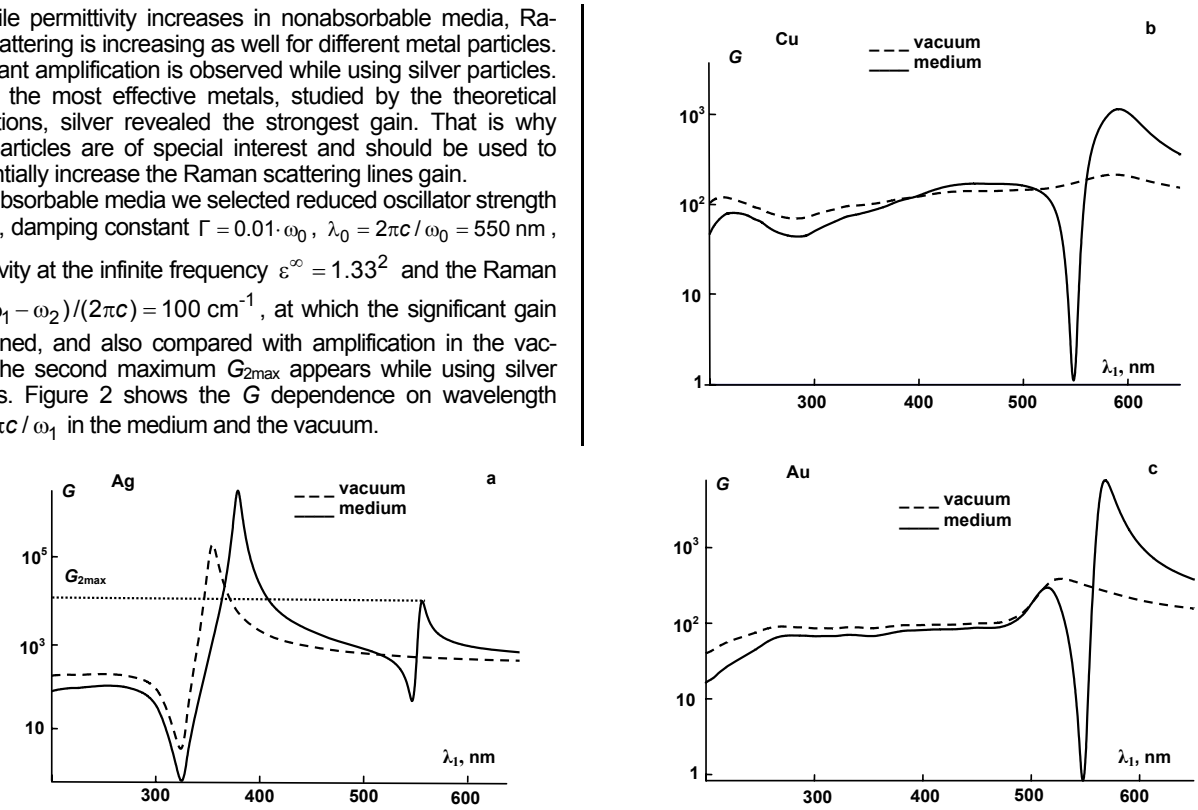

Fig. 2. The G gain dependence on wavelength in the medium and the vacuum: a – Ag, b – Cu, c – Au
($S = 0.1$, $\Gamma = 0.01 \times \omega_0$, $\lambda_0 = 550$ nm, $\varepsilon^{\infty} = 1.33^2$, $(\omega_1 - \omega_2)/(2\pi c) = 100$ cm^{-1})

Using such parameters with silver, the first maximum of the gain in medium is $G_{1max} = 6.91 \cdot 10^6$ at $\lambda_1 = 379$ nm, although in vacuum maximum gain is only $G_{1max} = 2.2 \cdot 10^5$ at $\lambda_1 = 355$. The second maximum with silver is $G_{2max} = 5.7 \cdot 10^3$ at $\lambda_1 = 556$ nm. For copper particles maximum Raman scattering lines gain $G_{max} = 1.1 \cdot 10^3$ at $\lambda = 591$ nm in medium and 212 in vacuum. For golden particles it is obtained $G_{max} = 7.7 \cdot 10^3$ at $\lambda = 568$ nm in medium and 370 in vacuum environment.

It is shown in Fig. 3 the change in gain for silver: a – first maximum of gain G_{1max} on the reduced oscillator strength S when $\Gamma = 0.01 \cdot \omega_0$, b – second maximum of gain G_{2max} on the reduced oscillator strength S when $\Gamma = 0.01 \cdot \omega_0$, c – G_{1max} on damping constant Γ when $S = 0.1$, d – G_{2max} on damping constant Γ when $S = 0.1$.

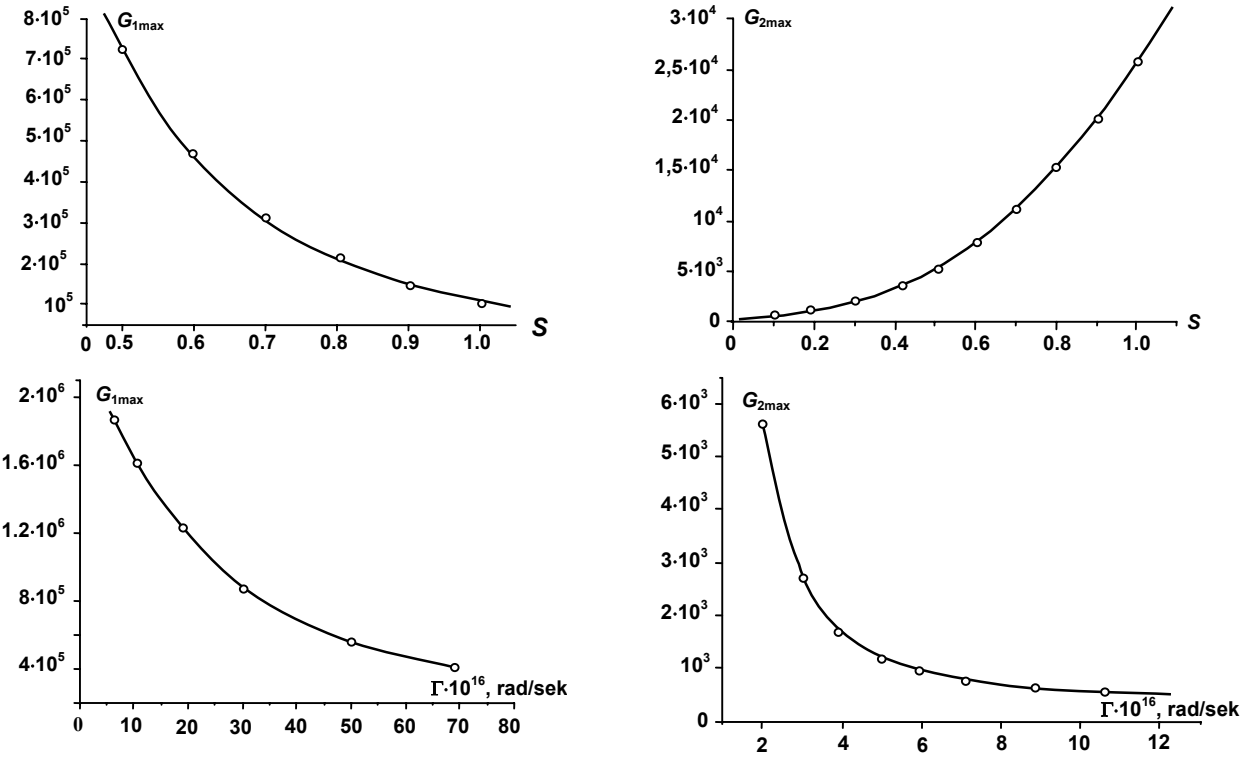

Fig. 3. Dependence of gain from reduced oscillator strength *S* and damping constant Γ for silver particles

The Raman scattering gain G_{2max} increases with increasing *S*. In contrast the first maximum G_{1max} for silver is decreasing. The significant gain G_{max} is observed on copper and gold particles with varying *S* and may reach tens of thousands.

Conclusions. Theoretical dependence of the surface-enhanced Raman scattering efficiency on nonabsorbable and absorbable media dielectrical permittivity with the noble metals particles was researched. The results were compared with the vacuum environment.

Maximum Raman scattering lines gain for particles Ag, Cu, Au in vacuum is: for silver – $2.2 \cdot 10^5$ at wavelength 355 nm, for gold – $3.4 \cdot 10^2$ at wavelength 527 nm, for copper – $2.0 \cdot 10^2$ at wavelength 587 nm. In the nonabsorbable media maximum Raman lines gain increases in all cases.

In the absorbable media the impact on Raman scattering amplification factor *G* was calculated from reduced oscillator strength *S* and damping constant Γ. It was shown that while using silver, the stronger is reduced oscillator strength, the less is first maximum gain value and the larger is second maximum gain value. While using particles of gold and copper, the stronger is reduced oscillator strength, the greater gain is obtained. For particles of Ag, Cu, Au amplification increases with decreasing damping constant.

1. *Алиев А. Р., Гаджиев А. З.* // Журнал прикладной спектроскопии. – 1993. – В. 59, № 5. 2. Физическая энциклопедия // Под. ред. *Прохорова.* – М.: Наука, 1988. 3. *Нобиев И. Р., Ефремов Р. Г., Чуманов Г. Д.* Гигантское комбинационное рассеяние и его приминение к изучению биологических молекул // Успехи физических наук. – 1988. – 154, вып. 3. 4. *Емельянов В. И., Коротеев Н. И.* Эффект гигантского комбинационного рассеяния света молекулами, адсорбированными на поверхности метала // Успехи физических наук. – 1981. – 135, вып. 2. 5. *Chang R. K., Furtak T. E.* Surface Enhanced Raman Scattering.– N. Y.: Plenum Press,1982. 6. *Johnson P.B., Christy R. W.* Optical constants of the noble metals // Phys. Rev. – 1972. – 6, N.6. 7. *Сивухин Д. В.* Общий курс физики. Электрика и магнетизм. – М.: Наука, 1980.

Submitted 25.11.10

UDC 577.33

K. Karpenko, post grad. stud.,
O. Sudakov, Ph. D.,
M. Platonov, Ph. D.

QUANTUM MECHANICAL ANALYSIS OF CYTIDINE AND 6-AZACYTIDINE BIOLOGICAL ACTIVITY MOLECULAR MECHANISMS

Нуклеозиди цитидин та 6-азацитидин – це дві природні органічні сполуки, які мають широкий спектр біологічної активності і певним чином взаємодіють із ДНК - полімеразою. У даній роботі було виконано неемпіричне квантово - механічне моделювання нуклеозидних комплексів з ДНК – полімеразою для з'ясування механізмів їх взаємодії. Оптимізовано їх геометрію у вакуумі, знайдено та порівняно стаціонарні енергії. Обрахунки проводились на обчислювальному кластері КНУ ім. Т. Шевченка за допомогою квантово - хімічного програмного комплексу GAMESS US на рівні теорії Unrestricted Hartree Fock + Density Functional Theory, з градієнтною корекцією B3LYP та повним базисним набором хвильових функцій 6 - 31G. Нижча енергія 6-азацитидину (~ 10 ккал/моль) у порівнянні з цитидином говорить про більшу стабільність 6-азацитидину. Наявність водневого зв'язку у молекулі цитидину та його відсутність у 6-азацитидину говорить про принципово різні механізми взаємодії з активним центром ДНК - полімерази.

Ключові слова: квантово-хімічне моделювання, метод Хартрі-Фока, оптимізація геометрії, цитидин, 6-азацитидин, ДНК - полімераза.

Nucleosides cytidine and 6-azacytidine offer wide spectrum of biological activities. The presumed reason of their activity is bonding with active site of DNA - polymerase. In present work we performed a non - empirical quantum mechanical simulation of nucleosides complexes with DNA - polymerase to investigate their interaction mechanisms. Geometry of both molecules were optimized in vacuum, their stationary energies were obtained and compared. Simulations were performed on the cluster of National Taras Shevchenko University of Kyiv by GAMESS US package (Hartree Fock, DFT B3LYP, 6 - 31G). Lower energy of 6-azacytidine (by 10 kcal/mol) comparatively to cytidine approves its greater stability. Hydrogen bond present in cytidine and absent in 6-azacytidine indicates their different bonding mechanisms with DNA - polymerase.

Key Words: Quantum chemical simulation, Hartree Fock method, geometry optimization, cytidine, 6-azacytidine, DNA – polymerase.

1. Introduction. Computer aided molecular modeling is widely used in the different branches of molecular biology, chemistry, microelectronics. Quantum chemical models provide the most precise information about the mechanisms of molecular structures functioning. Most of this information is unavailable to experimental investigation [10]. The prime example of such techniques is computer aided drug design. Quantum – mechanical and semi – classical computer – aided drug design allows finding of molecules structures that can significantly affect functions of cellular proteins [3]. In present work we performed ab-initio quantum mechanical investigation of cytidine and 6-azacytidine that are proved to have biological activities including antiviral and antitumoral ones. Many of such activities may be caused by interactions of these substances with DNA-polymerase [12].

2. General problem and task. A DNA – polymerase is an enzyme that catalyzes the polymerization of deoxyribonucleotides into a DNA strand. DNA polymerases are best-known for their role in DNA replication, in which the polymerase "reads" an intact DNA strand as a template and uses it to synthesize the new strand. This mechanism copies a piece of DNA. Some DNA - polymerases have own ability to retrieve mistakes in the DNA strand, which is gathered anew. Not only cells, but other microscopic living forms have DNA - polymerase. For example retroviruses have own gene of unusual DNA - polymerase, which is yet named by reverse transcriptase [1].

Nucleosides cytidine and 6-azacytidine are presumed to establish bonding with active site of DNA – polymerase. Cytidine is a natural organic compound which consists of residues of pyrimidine's basis of cytosine and hydrocarbon of ribose [2]. 6-azacytidine is another modified nucleoside [12, 4]. Both offers experimentally proved antiviral and antitumoral activity, are well soluble in water and gyroscopic. These substances may be found in living cells in composition ribonucleic acids and nucleotides [7]. X-ray structures of DNA - polymerase with cytidine and 6-azacytidine are available but their interaction mechanisms are still need clarification.

3. Quantum chemical simulation of nucleosides. 3.1. Theory and software. Simulation of molecular structures is performed by calculation of molecular structures energy under the necessary external conditions. Minimizing the energy it is possible to find many other molecule's characteristics and macroscopic characteristics of matter.

All quantum chemistry methods are based on solution of the Schrödinger equation for a given set of atoms and molecules. Various methods of quantum chemistry have different accuracy and require different number of operations are rather long in time and requires application of parallel computing [3].

Theory of quantum - chemical calculations is described in literature [8]. Let us summarize the necessary aspects. These methods allow finding approximate solution of the Schrodinger equation for given types of atoms and atoms and their spatial position. To use quantum-chemical program required initial conditions: trial structure of compounds studied, its charge, multiplicity, and a set of commands that define the calculation method and conditions of its implementation.

Traditional methods of quantum chemistry are based on Hartree – Fock [8] method and use the wave function as the characteristic of a quantum system. They in principle can give an accurate answer about the structure, energy, and chemical properties of the compounds. This requires full knowledge about the energy of the electrons correlated motion and the concept of the atomic orbitals that have no error concerned with basis set selection. Today, such calculations are possible only for very simple molecules.

A very attractive alternative to these methods is an approach that is based on density functional theory(Density Functional Theory, DFT) [8]. It appeared that DFT methods, being approximate in nature, in many cases and for many systems provide good accuracy that even exceeds the accuracy of results obtained by other methods. This method has the same time and computer resources requirements as the Hartree – Fock method.

Using DFT the properties of a many – electron system can be determined as the functional of electron density. This leads to a substantial simplification of the problem, since many - electron wave function depends on 3N variables – for 3 - dimensional coordinates for each of the N electrons, while the density – the function of only three spatial coordinates. The method of density functional theory is used in conjunction with the formalism of Kohn – Sham where Multiple interacting electrons in a static external field of atomic nuclei is reduced to the simpler problem of independent electrons moving in some effective potential. This effective potential includes the static potential of atomic nuclei, but also takes into account the Coulomb effects, in particular, the exchange interaction and electron correlation. One of the most common forms of exchange functional is called BLYP (Becke, Lee, Yang, and Parr) [8]. Even more widespread approach B3LYP, which is based on a hybrid functional, where the exchange energy is calculated with the assistance of the exact result obtained by the Hartree – Fock.

3.2. Results and analysis. For non-empiric quantum – mechanical simulation we used GAMESS US package [14]. Quantum-chemical complex GAMESS (General Atomic and Molecular Electronic Structure System) is one of the most popular programs for theoretical studies of the properties of chemical systems. Its main advantage is the free access to the source code of the program and it has wide-ranging coverage of basic computational algorithms required for the theoretical study of chemical systems.

For visualization of biological structures used quantum-chemical program MOLDEN [13] is a software package for pre- and post- processing of computational chemistry program data. Interfacing to the ab initio programs GAMESS - US/UK is provided.

Non – empirical quantum mechanical simulations of both nucleosides in vacuum were performed on the computational cluster of National Taras Shevchenko University of Kyiv [9] by GAMESS US package (Hartree Fock, DFT, B3LYP, 6 – 31G).

Initial structures of nucleosides cytidine (Fig. 1) and 6-azacytidine (Fig. 2) were obtained from X-ray. In 6-azacytidine, in comparison with cytidine, one atom of hydrogen is absent and atom of carbon is replaced by the nitrogen (see selection in Fig. 2). Other atoms are the same in both structures: spatial location of atoms and distances between them are identical.

Cytidine molecule consists of 29 atoms, has 127 electrons, number of 6 – 31G basis functions – 315. Spin multiplicity of this molecule is 2, because it lacks one proton as in X – ray data. Computing time of geometry optimization is 22 hours on 16 processors and required 1.1 Gb of memory.

In contrast to cytidine, molecule of 6-azacytidine consists of 28 atoms, has 127 electrons, number of 6 – 31G basis functions – 378. 6-azacytidine molecule also lacks one proton as in X - ray data and its spin multiplicity is also 2. Computing time of geometry optimization is 27 hours on 16 processors and required 8.1 Gb of memory.

Geometry of molecules was found by minimizing of molecule's energy in vacuum. Initial orbitals we obtained by Huckel method, which used approximation non-correlation electrons. Optimized geometry of both structures is described below: cytidine (Fig. 3) and 6-azacytidine (Fig. 4).

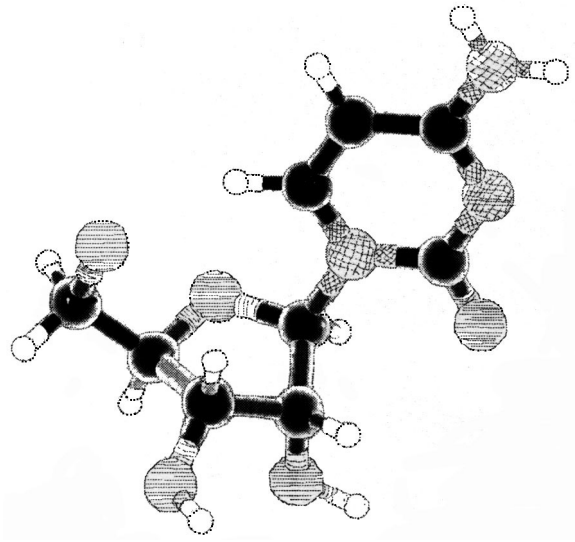

Fig. 1. Cytidine before geometry optimization

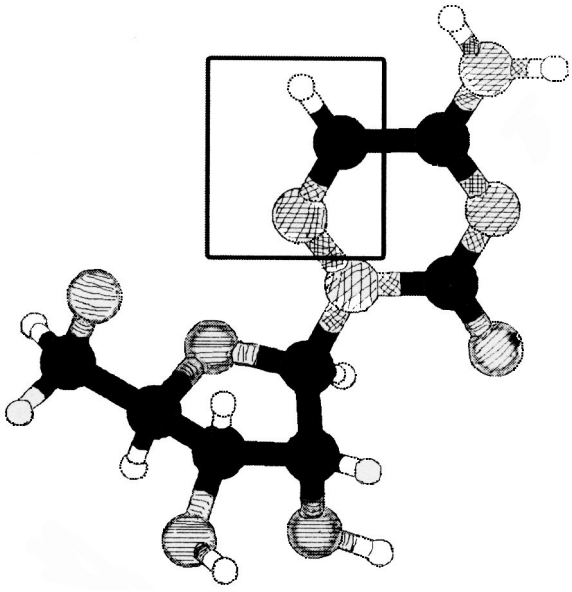

Fig. 2. 6-azacytidine before geometry optimization

It is easy to see that hydrogen bond present in cytidine (Fig. 3, square selection) and absent in 6-azacytidine after geometry optimization in stationary point. Presents of H - bond is proved by the distance of 1.85 A between Oxygen and Carbon atoms. This fact indicates their different bonding mechanisms with DNA – polymerase [11].

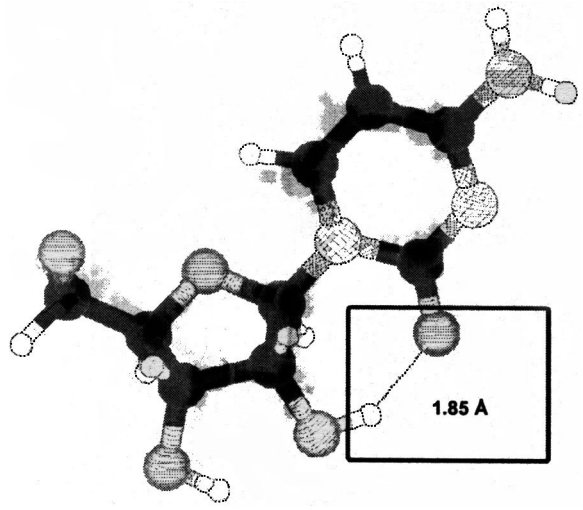

Fig. 3. Cytidine after geometry optimization

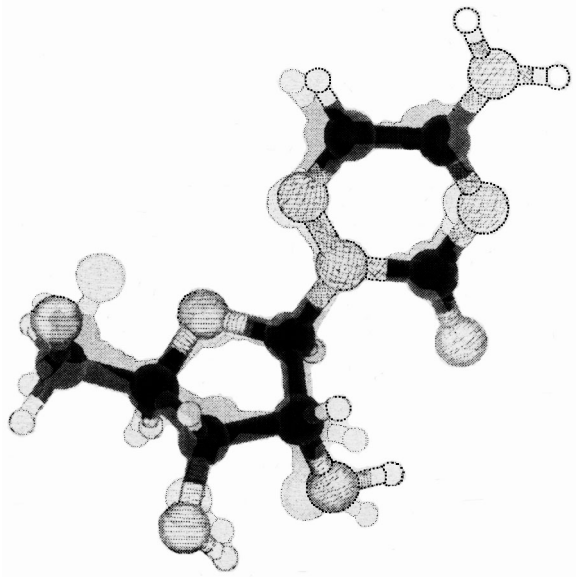

Fig. 4. 6-azacytidine after geometry optimization

Hydrogen bonding is responsible for the formation of many molecular and ion complexes in virtually all biological processes, including enzymatic catalysis. The most important fact is that hydrogen bonding involved in the process of DNA replication. This process is accompanied by complex formation of purine and pyrimidine bases by forming two hydrogen bonds - the binding of adenine and thymine or three - the binding of guanine and cytosine [5].

Hydrogen bonding occurs in the interaction of depleted electrons of the hydrogen atom with an unshared electron pair of the oxygen atom. One of the criteria that indicating the formation of hydrogen bonds between molecules, is that the distance between neighboring atoms, which participate in hydrogen bonding, is much less than the sum of their van deer Waals radii [6]. Presence of H – bonds in cytidine suggests the possibility of interaction with DNA polymerase by hydrogen ties. Geometry convergence for cytidine was quick and took 95 iterations. To improve geometry convergence for 6-azacytidine we start computing without DFT with precision 10–3. After convergence was achieved the precision was increased to 10–6 and DFT was turned on. All optimization took 135 iterations.

And lack of H - bonds in the 6-azacytidine spoke about probable Van der Waals ties with DNA – polymerase.

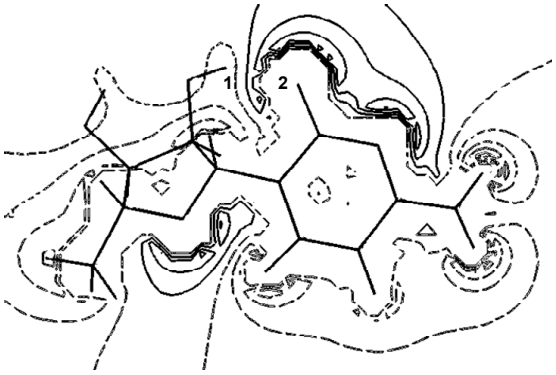

Fig. 5. Electric charge in cytidine.
Solid line – negative charge, dotted line – positive chargeFig

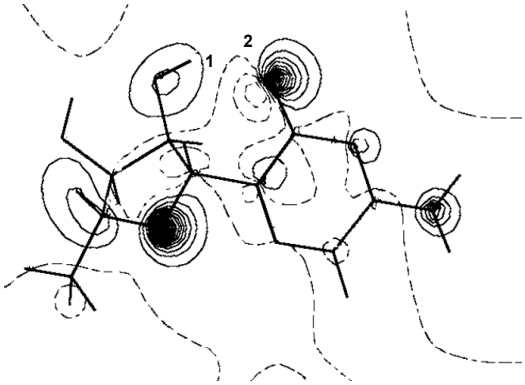

Fig. 6. Electric charge in 6azacytidine.
Solid line – negative charge, dotted line – positive charge

These two facts are also proved by analysis of electric charge distribution in both molecules. (Fig. 5 and Fig. 6). Red lines correspond to regions of negative charges, and green lines to the regions of positive charges. Cytidine (Fig. 5) has region of negative charge open outside of the molecule (Oxygen atom 2). This atom contacts Hydrogen atom 1 with positive charge. This also proves the existing of H - bond between these atoms. This hydrogen bond is open outside the molecule and may participate in bonding with active site of DNA - polymerase. In contrast to this appropriate atoms of 6-azacytidine (Fig. 6) do not form H-bond because region of positive charge exist between negatively charged Hydrogen 1 and Oxygen 2. All negatively charged atoms in 6-azacytidine are surrounded by regions of positive charge. So this molecule is supposed to interact with active site of DNA - polymerase by Van der Waals ties.

Cytidine's general energy is -890.03 Hartree or -233.7*107 Joule/mole, and 6-azacytidine's general energy is -906.07 Hartree or -237.9*107 Joule/mole. Lower energy of 6-azacytidine comparatively to cytidine approves its greater stability.

4. Conclusions. Non-empirical quantum mechanical simulation of nucleosides cytidine and 6-azacytidine at the level of theory UHF + DFT leads to the following conclusions:

- Lower energy of 6-azacytidine comparatively to cytidine approves its greater stability;
- Hydrogen bond present in cytidine and absent in 6-azacytidine indicates their different bonding mechanisms with DNA - polymerase.
- Taking into account hydrogen bond present in cytidine we suggest that it can interact with DNA- polymerase by hydrogen bonding
- 6-azacytidine is supposed to interact with DNA-polymerase by Van der Waals ties.

Now the last two assumptions are being investigated by analysis of cytidine and 6- azacytidine complexes with DNA-polymerase active cite.

5. Acknowledgements. All calculations were performed on computing cluster of Information and Computer Center National Taras Shevchenko University of Kyiv.

1. *Глик Б., Пастернак Дж.* Молекулярная биотехнология. Принципы и при-менение. – Москва: Мир, 2002. 2. *Кнорре Д. Г., Мызина С. Д.* Биологическая химия. – 3. – Москва: Высшая школа, 2000. 3. *Кононов М. В., Мисник А. В., Радченко С. П., Судаков О. О.* Моделювання фізичних процесів. Видавничо-поліграфічний центр "Київський університет". 2006. 4. Потягайло А. Л. Протонна рухливість у модельних білково-нуклеїнових і нуклеїново-нуклеїнових комплексах та її можливе біологічне значення // Дисертація на здобуття наукового ступеня кандидата біологічних наук. Київ 2002. 5. *Раевский О. А.* Дескрипторы водородной связи в компьютерном молекулярном дизайне // Российский химический журнал (Журнал Российского химического общества им. Д. И. Менделеева), 2006.– №2. 6. *Степанов Н. Ф.* Водородная связь: как ее понимать // Соросовский образовательный журнал, том 7, №2, 2001. 7. *Титович О. І., Зінченко А. І.* Ферментативний синтез цитидин-5'-дифо-сфатхоліну. Мінськ 2006. 8. *Хурсан С. Л.* Квантовая механика и квантовая химия. Конспекты лекций. – Уфа: ЧП Раянов, 2005. 9. *Boyko Yu. V., Vystoropsky O. O., Nychyporuk T. V., Sudakov O. O.* Kyiv National Taras Shevchenko University High Performance Computing Cluster. // Proc. Third International Young Scientists Conference on Applied Physics. June, 18–20, 2003, Kyiv, Ukraine. 10. *Hinchliffe Alan*. Modelling molecular structures. Second edition. Department of Chemistry, UMIST,Manchester,UK, 2000. 11. *Karpenko Kateryna, Sudakov Oleksandr, Platonov Maksim.* Looking for bonding mecha-nisms of cytidine and 6-azacytidine with DNA-polymerase active site by quantum chemical study // X International Young Scientists' Conference on Applied Physics, Kyiv, Ukraine 2010. 12. *Platonov Maxym O., Sudakov Olexandr O., Palchykovs'ka Larysa H., Alexeeva Inna V., Boyko Yuriy V., Hovorun Dmytro M.*. Non-empirical quantum-mechanical conformational analysis of 6-azacytidine – a modified nucleoside of wide spectrum of biological activities // International Conference Modern Problems of Theoretical Physics (MPTP). Kyiv 2002. 13. *Schaftenaar G., Noordik J. H.* MOLDEN: a pre- and post-processing program for molecular and electronic structures // J. Comput.-Aided Mol. Design. 2000. V. 14. 14. *Schmidt M. W., Baldridge K. K., Boatz J. A., Elbert S. T., Gordon M. S., Jensen J. H. , Koseki S., Matsunaga N., Nguyen K. A.,* Windus S. J. Su, T. L., Dupuis M., Montgomery J. A. . Comput.Chem. 14, 1347–1363 (1993).

Submitted 24.09.10

UDC 533.9

O. Kelnyk, Ph. D.,
O. Samchuk, engineer.

PECULIARITIES OF ENERGY DISTRIBUTION FUNCTIONS FOR PARTICLES IN MICROPLASMA DISCHARGE INSIDE DIELECTRIC CELL

Шляхом комп'ютерного моделювання комбінованим методом крупних частинок у комірках – Монте-Карло досліджено еволюцію функцій розподілу електроніе та іонів за енергіями у мікроплазмовому розряді всередині копланарної діелектричної комірки розмірами 700x200 мкм для різних прикладених напруг. Для більшої частини електронів справедливий розподіл Максвелла, існує також певна додаткова кількість нерівноважних електроніе. Для іонів із досить великою точністю справедливий розподіл Дрюйвейстейна. В оптимальному діапазоні прикладених напруг (210–250 В) розряд має найвищу енергетичну ефективність з точки зору випромінювання ультрафіолетових квантів.

Ключові слова: мікроплазмовий розряд, комп'ютерне моделювання, функція розподілу, нерівноважні електрони.

Evolution of the electrons' and ions' energy distribution functions for the microplasma discharge inside coplanar dielectric cell with 700x200 μm size was studied at various applied voltages via computer simulation with combined large particles-in-cells – Monte Carlo method. For most of electrons, Maxwellian distribution is applicable but some portion of additional non-equilibrium electrons also exists. For ions, Dryuvesteynian distribution is applicable with good accuracy. In the optimal applied voltages band (210–250 V), discharge has highest energetic efficacy in aspect of the ultraviolet photons' radiation.

Key words: microplasma discharge, computer simulation, distribution function, non-equilibrium electrons.

1. Introduction. Microplasma discharges are currently used in wide range of applications such as plasma technology devices and plasma display panels (PDP, [1]). In modern types of PDPs, pulse discharges in noble gas mixtures (mostly neon and xenon) inside dielectric cells are applied as a source of ultraviolet (UV) photons' emission that excites the phosphor with luminescence at appropriate visible color. Such a multi-stage process has quite low energetic efficacy (about 1 %) and most of energy losses are caused by the elementary processes in the discharge where background gas excitation and ionization can be effectively performed only by the small portion of electrons at the high energy band of distribution function. So one of the ways to increase the energetic efficacy of UV radiation from pulse microplasma discharges can be the shifting of electron energy distribution function from Maxwellian shape in order to increase the amount of non-equilibrium electrons in the necessary high-energy band. That goal can be reached in various ways such as optimization of the cell construction and electrodes configuration, applied voltage amplitude and waveform shape, gas mixture composition, consistence and pressure. Also, there can be influence of striation structures formed in such discharges in certain conditions. In this work, aspect of applied voltage amplitude is analyzed,

Among existing works, investigations of applied voltages waveforms and respective waveforms of discharge current inside dielectric PDP cell can be found both in computer simulation (for instance, [19]) and experimental (e.g. [10]) approaches. Coplanar behaviour of that discharge type means that address electrode current is much smaller in comparison with the current to coplanar electrodes [19] so phosphor degradation due to the ion bombardment is lowered. In the case of additional electrodes' using, pulse of gas discharge current can be shaped in multi-phase form. For instance, discharge can proceed in two phases with two maxima of current waveform [8, 10]. One can also note the delay between positive and negative electrodes' currents that appear for relatively small discharge driving voltages but vanish in the case of larger address voltages applying. According to our recent works [3, 14, 15], small current to the address electrode has pulsations corresponding to the oscillations of electric potential near that electrode. There are many other important results already obtained but one can see that the problem of applied voltage and discharge current waveforms' influences upon the particles' energy distributions in the concerned discharge is not yet completely investigated.

Application of plasma with striation structures can also be a method to obtain a non-equilibrium energy distribution for discharge particles those can be accelerated between plasma spatial structures. Striation of microplasma discharge inside dielectric cell is an experimental fact described in many existing works (see, e.g., [9,16]). This phenomenon was also investigated via computer simulation in works [2,6,9,17] and others. Appearance of striation structures usually takes place in the positive electrode region and then those structures slowly move towards the negative electrode. Amount of striation structures and their maximal electric charge density disturbance depends strongly upon composition and pressure of the gas mixture [2, 16]. These structures usually appear during the initial discharge phase when electrons are accumulated on the dielectric surface near the positive electrode and positive ions' charge bunch is formed upon that surface. At those conditions, applied voltage in the address electrode region is effectively shielded and transversal electric field component accelerates electrons along that electrode. That effect is increased with the striation structures growth. Initially formed as small ion spatial distribution disturbances, striation structures quickly increase their amplitude and become visible on the potential profile. Note that negative charge fluctuation appears near positive electrode so striation structures' formation strongly depends on this fluctuation [16]. Disturbance of electron energy distribution due to the striation structure formation described in our recent works [4, 13]. Such a distribution has additional electrons in the high-energy band and those electrons are capable for background gas excitation and ionization so the striation structures' formation can increase the discharge energetic efficacy. There are some more interesting results about the striation structures but their influence upon the particles' energy distributions at different discharge driving voltages is also not yet studied completely.

So the main purpose of this paper is investigation of electrons' and ions' energy distribution functions in the microplasma discharge inside coplanar dielectric cell for different applied voltages in order to find a regimes with highest energetic efficacy.

2. Model description and simulation parameters. For computer simulation, our original computational code [12] was applied. Code implements two-dimensional (2D) electrostatic particles'-in-cells (PiC) method for calculation of large particles' motion. That method provides much more information about particles' kinetics than contemporary hydrodynamic approaches. For microscopic plasma systems such as microplasma discharges, each large particle contain relatively small bunch of real particles (about 100 and less) so the accuracy of calculations must be rather high. Code is oriented to weakly ionised plasma systems so the background gas neutrals are taken into account as continuum with constant parameters. Elementary processes (large particles' collisions with both neutral background and other large particles) are simulated via Monte Carlo method.

As a background gas, neon-xenon mixture was taken. Such a mixture is typical for commercial PDPs. The mixture contained 95 % neon and 5% xenon with total pressure of 500 Torr. Electrons, neon and xenon atomic ions, several sorts of excited neon and xenon atoms, Ne 2+, NeXe, Xe 2+ excimer ions and respective excited excimer molecules were taken as sorts of large particles. Excited atoms and excimers were taken into account because their influence on the discharge evolution and UV photon emission was quite significant [11, 18]. Three most significant sorts of UV photons (147 nm, 150 nm and 173 nm wavelength) and two sorts of infrared (IR) photons (600nm and 800nm) were also taken into account as well as the possibility of their reabsorption. IR photons are important for the formation of discharge UV radiation as well as for the discharge evolution (via reabsorption, see, e.g. [5, 7]).

More than 100 elementary processes (see Table 1) were taken into account in the simulations. Those processes included large particles' elastic collisions with neutral background and another large particles, excitation of neutrals related and further emission of photons described above, ionisation, charge transfer, excimer ions' and excited molecules formation and decay, photons' radiation and absorption. Processes on cell walls' surface included electrons' and ions adsorption (with corresponding charging of the wall) and secondary ion-electron emission (from the walls' section at the cell front side where such emission is significant).

Table 1. **List of elementary processes taken into account**

e + Ne-> e + Ne	Xe** + Xe->Xe* (3P1) + Xe	Xe_2* + Xe->Xe + Xe + Xe	Xe**->Xe* (3P2) + hν (800nm)
e + Xe-> e + Xe	Xe** + Xe + Ne->Xe_2* (3Zu+) + Ne	Xe_2*->2Xe + hν	Xe**->Xe* (3P1) + hν (800nm)
e + Ne-> e + Ne +	Xe** + Xe + Ne->Xe_2* (Ou+) + Ne	Xe_2* (Ou+) + Xe->Xe_2* (1Zu+) + Xe	Xe**->Xe***
e + Xe-> e + Xe +	Xe** + Xe + Xe->Xe_2** + Xe	Ne** + Xe->e + $NeXe^+$	Ne* + Ne*->Ne^+ + e + Ne
e + N e-> e + Ne*	Xe** + Xe + Ne->Xe_2* + Xe	Ne_2^+ + Xe->$NeXe^+$ + Ne	$NeXe^+$ + e->Xe* + Xe
e + Ne-> e + Ne**	Xe** + 2Xe->Xe_2* + Xe	Ne_2^+ + Xe->Xe^+ + 2Ne	$NeXe^+$ + e->Xe** + Xe
e + Xe-> e + Xe* (3P1)	Xe** + Xe->Xe* + Xe	Ne_2^+ + Xe + Ne->Xe^+ + 3Ne	Xe_2* + Xe2*->Xe_2^+ + e + 2Xe
e + Xe-> e + Xe* (3P2)	Xe**->Xe* + hν	Ne_2* + Xe->Xe^+ + 2Ne + e	Xe_2* + e->Xe_2^+ + e + e
e + Xe-> e + Xe**	Xe**->Xe	Xe*** + Xe + Xe->Xe2* + Xe	Xe_2* + hν->Xe_2^+ + e
e + Xe-> e + Xe***	Ne* + Xe + Xe->Xe_2* + Ne	Xe*** + Xe + Ne->Xe_2* + Ne	Xe_2* (Ou+)->2Xe + hν (150nm)
Xe* (3P2) + Ne->Xe* (3P1) + Ne	Ne* + Xe->e + Xe^+ + Ne	Xe*** + Xe->Xe_2^+ + e	Ne_2* + e->Ne_2^+ + 2e
Xe* (3P2) + Xe->Xe* (3P1) + Xe	Ne* + Xe->e + $NeXe^+$	Xe* (3P2) + Xe* (3P2)->e + Xe^+ + Xe	Ne_2*->2Ne + hν
Xe* (3P2) + Xe + Ne->Xe_2* (3Zu+) + Ne	Ne* + Ne + Ne->Ne_2* + Ne	Xe* (3P2) + Xe* (3P1)->e + Xe^+ + Xe	Ne**->Ne* + hν (600nm)
Xe* (3P2) + Xe + Xe->Xe_2* (3Zu+) + Xe	Ne* + Ne + Xe->Ne_2* + Xe	Xe* + e->Xe^+ + e + e	Xe_2^+ + e->Xe* + Xe
Xe* (3P1) + Xe->Xe* (3P2) + Xe	$NeXe^+$ + Xe->Xe_2^+ + Ne	Xe* + e->e + Xe	Xe_2^+ + e->X*** + Xe
Xe* (3P1) + Xe + Ne->Xe_2* (Ou+) + Ne	Xe^+ + 2Xe->Xe_2^+ + Xe	Xe* + e->Xe*** + e	Xe_2^+ + hν-> Xe_+ + Xe
Xe* (3P1) + Xe + Xe->Xe_2* (Ou+) + Xe	Xe^+ + Xe + Ne->Xe_2^+ + Ne	Xe* + hν->Xe^+ + e	Ne_2^+ + e->Ne* + Ne
Xe* + 2Xe->Xe_2* (3Zu+) + Xe	Xe^+ + Xe + Ne->$NeXe^+$ + Ne	Xe* (3P1) + Xe* (3P1) ->e + Xe^+ + Xe	Xe_2**->Xe (3P2) + Xe
Xe* + 2Xe->Xe_2* (1Zu+) + Xe	Xe^+ + 2Ne->$NeXe^+$ + Ne	Xe* (3P1) ->Xe + hν (147 nm)	Xe_2**->Xe (3P1) + Xe
Xe* + 2Xe->Xe_2* + Xe	Ne^+ + Ne + Xe->$NeXe^+$ + Ne	Xe** + Xe**->Xe^+ + e + Xe	Xe*** + X***->Xe^+ + e + Xe
Xe* + Xe + Ne->Xe_2* + Xe + Ne	Ne^+ + Ne + Xe->Ne_2^+ + Xe	Xe** + e->Xe^+ + e + e	Xe*** + e->Xe^+ + e + e
Xe* + Xe->2Xe	Ne^+ + Ne + Ne->Ne_2^+ + Ne	X** + e->X*** + e	Xe*** + e->Xe** + e
Xe** + Ne->Xe* (3P2) + Ne	Ne^+ + Xe->Xe^+ + Ne	Xe** + e->Xe* + e	Xe*** + e->Xe* + e
Xe** + Ne->Xe* (3P1) + Ne	Xe_2* (3Zu+) ->2Xe + hν (173 nm)	Xe** + e->e + Xe	Xe***->Xe** + hν
Xe** + Xe->Xe* (3P2) + Xe	Xe_2* (1Zu+) ->2Xe + hν (173 nm)	Xe** + hν->Xe^+ + e	Xe***->Xe + hν

Information about elementary processes' rates was obtained from many publications like [5, 7 ,9] and included both experimentally measured and theoretically calculated values. Different values of same reaction rates presented in different sources were averaged.

Typical dielectric PDP cell was treated (Fig. 1). Such a cell has a coplanar geometry: one of three electrodes (address electrode) is located at the bottom side of cell and two another (coplanar electrodes) are located upper left and upper right at a horizontal distance much smaller than vertical distance from both of them to address electrode. Cell dimensions were 700 μm in width and 200 μm in height. In real PDPs, front glass is located above coplanar electrodes so they are made from transparent conductive material like ITO. Despite the relatively small conductivity of such a material, relative potential gradient along them in real PDP is about 1 %, so in this simulation, all electrodes were considered equipotential. All electrodes are covered with dielectric sheath that consists of phosphor layer covering the dielectric wall (barrier rib) at left, right and bottom cell sides and transparent material with good secondary emission rate like MgO at the topside. MgO is applied for obtaining a significant amount of additional electrons from secondary ion-electron emission in order to make possible the discharge sustaining at lower applied voltages.

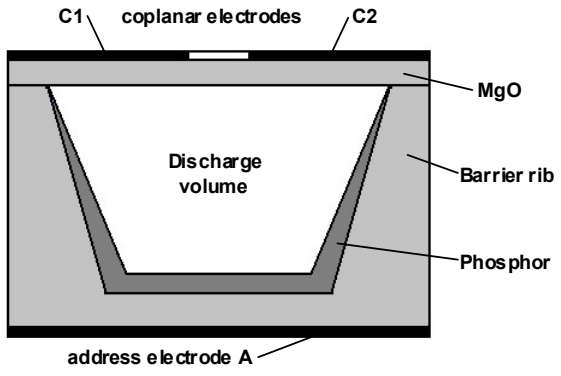

Fig. 1. Dielectric cell with coplanar electrodes' configuration

In this simulation, secondary ion-electron emission was taken into account from the upper MgO wall. Phosphor has much less secondary emission rate and it is bombarded by ions much weaker due to the coplanar discharge behaviour. So the secondary emission from phosphor (left, right and bottom walls) can be neglected.

Being dielectrically insulated, electrodes cannot absorb charged particles so reaching the dielectric wall these particles stay at surface forming the wall charge. That charge increases with time during the discharge evolution and finally shields the electric field of applied voltage causing the discharge decay. So the discharge current has a pulse shape even for the constant applied voltage. In real PDPs, discharge sustaining voltage is applied between coplanar electrodes (negative potential is applied to one coplanar electrode, another one is grounded). Address electrode is grounded in sustaining mode and has positive potential in the ignition mode. In this work, we considered **C2** coplanar electrode and address electrode grounded. Discharge driving voltage was taken with a shape of trapezoid pulses with 30 ns fronts' length and 1μs total pulse length, and it was applied to the **C1** coplanar electrode. So simulation corresponds to the sustaining mode of discharge in PDP cell. Amplitude of the applied voltage is varied in 175-290V band that corresponds to optimal discharge ignition conditions for considered cell size and gas composition and pressure.

Since the real particles' number in one large particle in this simulation is considered to be rather small (16), total amount of large particles is quite large (105–106), and there were enough particles in each small energy band. So energy distribution functions were obtained via direct calculation of particles' amount in each of these small bands, i.e. by definition.

3. Results and discussion. In order to increase the discharge UV radiation energetic efficacy, one must shift the electrons' energy distribution from equilibrium Maxwellian shape, especially in the high-energy band where electrons can efficiently excite and ionise neutral atoms. This section is devoted to the thorough analysis of electrons' energy distribution functions features and their evolution during discharge current pulses for different voltages in the band near the optimal discharge ignition conditions (175–290V). As it will be shown below, this band is naturally divided into three parts with different behaviour of microplasma discharge. These parts correspond to optimal applied voltages' band and adjacent bands of voltages slightly lower and higher than optimal.

For relatively low voltages (low-U band, 200 V and below), applied voltage is not enough for sufficient acceleration of electrons between collisions, so these electrons cannot effectively ionise neutral atoms of background gas. In that case, the discharge current is rather low as well as it's energetic effi-

cacy. Contrary, for the relatively large voltages of 260 V and above, initial electron avalanche is developed too fast and charged particles falling on dielectric walls form a significant charge there too early. So discharge quickly starts to decay, discharge pulse becomes too short and, consequently, energy efficacy also becomes lower. Between these bands, optimal voltage band lies (210–250V). In that band, efficacy of UV radiation from discharge is maximal.

3.1. Electrons' energy distributions for lower applied voltages. At first, we analyse the electron energy distribution for the discharge at rather low voltage of 175 V that lie deeply in low-U band. For such a voltage, electron and ion components of discharge current have a shape plotted on Fig. 2. One can see that electron avalanche is developed quite slowly and, as a result, total discharge current amplitude is rather small. This waveform has a shape of long pulse with almost equal forefront and backfront lengths.

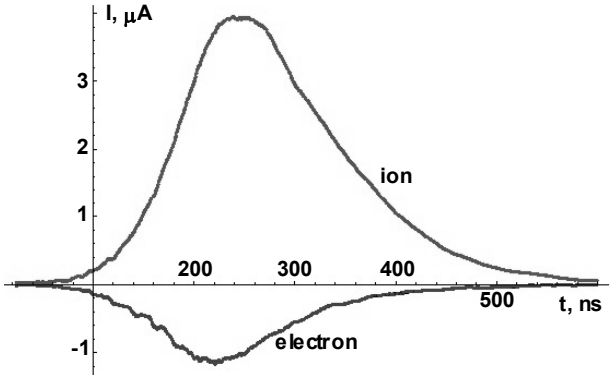

Fig. 2. Waveforms for ion end electron components of total discharge current. U = 175V

Electrons' energy distribution for that voltage has rather non-Maxwellian form with large noise component due to the small total amount of electrons present in the discharge volume at given time point. Such a distribution is shown on Fig.3 for the time point of total discharge current maximum (t = 250 ns).

Fig. 3. Electrons' energy distribution for time point of maximal discharge current, t = 250 ns. U = 175V

Note that maximum of distribution corresponds to relatively high energy and there are some electrons in high-energy band (8eV and higher) those are capable to effective ionization and excitation. However, total amount of these electrons is quite small so neutrals' excitation at following stage of discharge decay is not very effective.

Electrons' distribution upon the horizontal (vX) and vertical (vY) velocity components is shown on Fig. 4 as density plot (darker points contain more electrons). This distribution is anisotropic: one can see some additional portion of electrons in the lower vY band caused by the voltage applied between **C1** and **A** electrodes while there are no electrons in the right vx band that corresponds to the voltage applied between coplanar electrodes **C1** and **C2**. So at that low voltage the discharge mainly ignites between **C1** and **A** electrodes (so-called "volume discharge mode" contrary to "coplanar mode" that such a dielectric cell geometry was designed for).

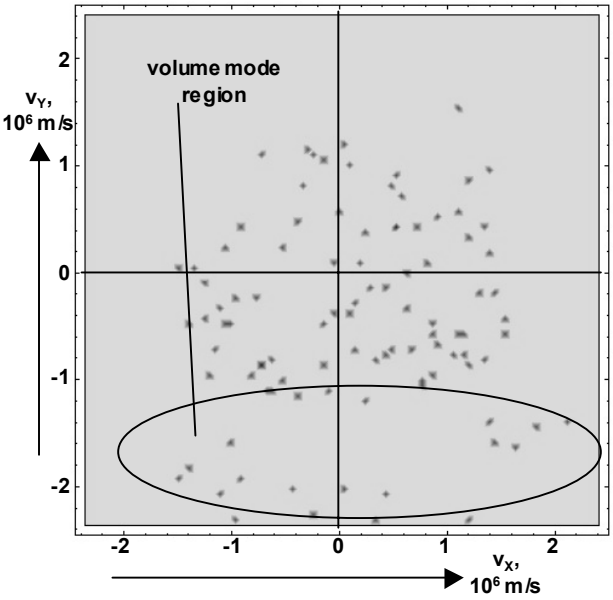

Fig. 4. Electrons' distribution upon v_X–v_Y velocity components for the time point of maximal discharge current, t = 250 ns. U = 175V

So the microplasma discharge at voltages significantly lower than optimal ones has completely another behaviour relatively to the cases of optimal and higher driving voltages. Very small discharge currents in that mode cause even smaller UV photons' emission and, consequently, make this discharge completely energetically inefficient.

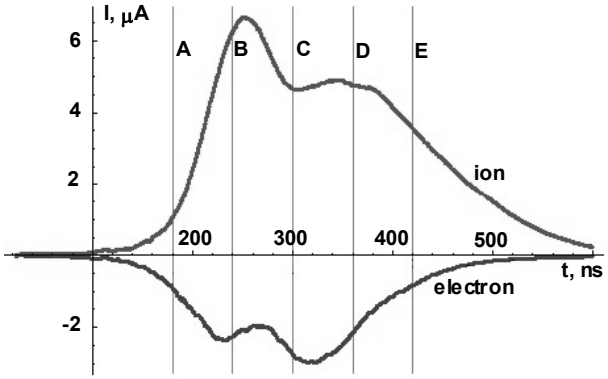

Fig. 5. Waveforms for ion end electron components of total discharge current. U = 190V

Closer to the optimal voltage band, discharge obtains more features of the really coplanar discharge mode. Fig. 5 shows waveforms of discharge current electron and ion components at the driving voltage of 190 V. One can see the second maximum formation (C-D time interval) that corresponds to the main current maximum for larger voltages. Note also that the discharge current pulse for 190V driving voltage is effectively longer than one for 175 V (Fig. 2) because the second (really coplanar) discharge stage at C-D interval takes place. That result is clear from comparison of electrons' distributions upon vX and vY velocity components at those two driving voltages (Fig. 4 and Fig. 6). Being absent for 175 V applied voltage (Fig. 4), coplanar mode region is quite expressed for the 190 V case (Fig. 6). Coplanar mode region (right region of plot) has a significant amount of electrons for

190V (Fig. 6) contrary to the 175 V case (Fig. 4). These electrons effectively ionise neutrals at consequent discharge stage and form the second maximum of the discharge current.

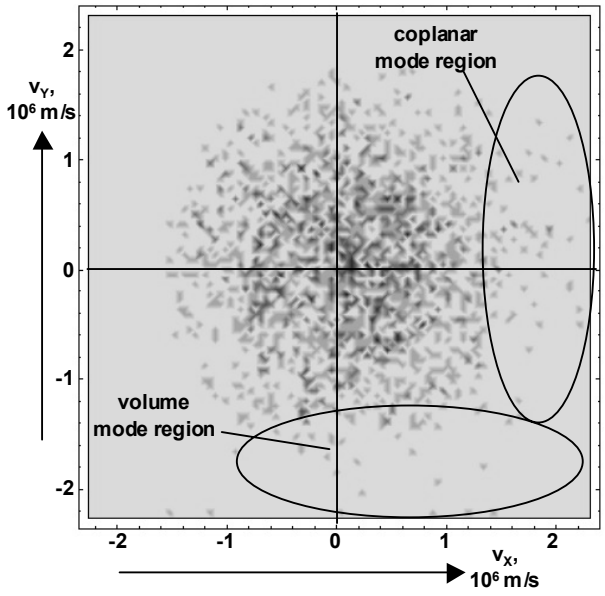

Fig. 6. Electrons' distribution upon v_X-v_Y velocity components for time point of maximal discharge current, t = 240 ns. U = 190V

Fig. 7 shows the electrons' energy distribution. Contrary to the Fig. 3 (175 V), that distribution can be approximated in good correspondence with some near Maxwellian distribution function (dashed curve at Fig. 7). That means the majority of electrons form an equilibrium energy distribution and their effective electron temperature can be determined.

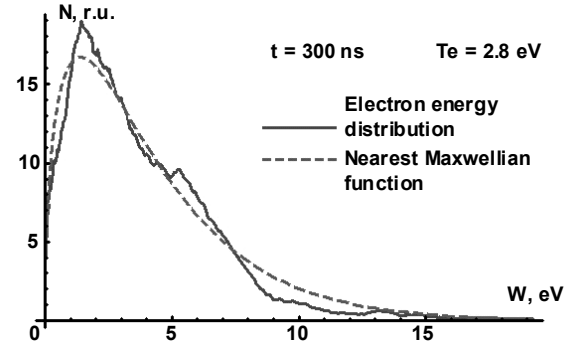

Fig. 7. Electrons' energy distribution and nearest Maxwellian function for time point of maximal discharge current, t = 240 ns, U = 190V

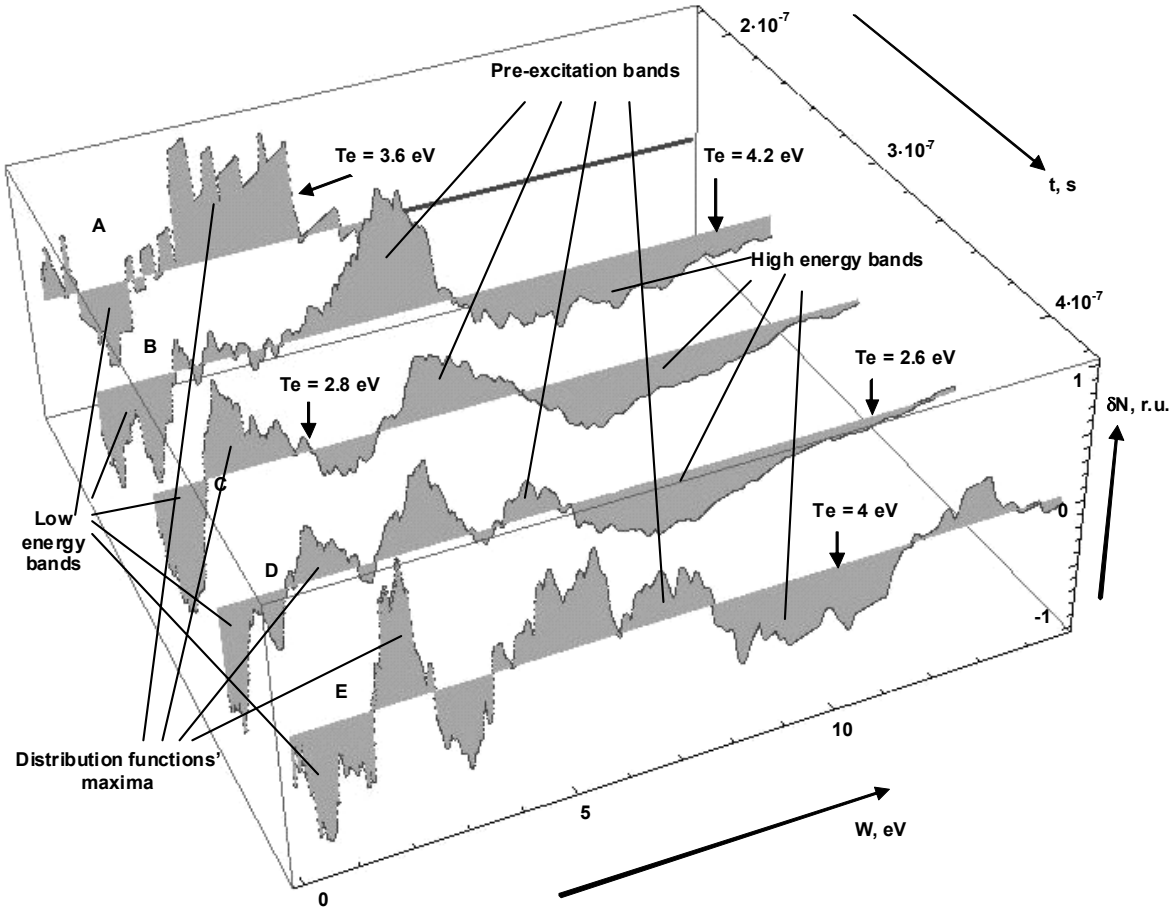

Fig. 8. Difference between electrons' energy distribution and nearest Maxwellian function during the discharge pulse, U = 190V

One can see that this distribution, being Maxwellian for most electrons, have some differences corresponding to additional non-equilibrium electrons (if real distribution lies above the nearest Maxwellian function) or lack of such electrons (if below). Of course, if non-equilibrium electrons are present in the energy band of effective excitation and ionization of backround gas neutrals, discharge will be more energetically effective.

Evolution of non-equilibrium electrons energy distribution during the discharge evolution for 19 0V driving voltage is presented on Fig. 8. Due to the complex behaviour of that function, 5 samples are presented instead the 3D plot. These samples were calculated for time points A-D shown on current waveforms at Fig. 5 (190 V) and corresponding to characteristic stages of microplasma discharge evolution.

The characteristic time points of discharge current pulse are chosen naturally from the shape of its waveform (Fig. 5) and include the start of initial electron avalanche (A), the first maximum corresponding to the electron current and volume stage of discharge evolution (B), the decay related to screening of the volume electric field by electrons falled onto the wall upon address electrode (C), the growth of coplanar discharge current up to its second maximum (D) and the start of the discharge final decay (E). Note that for each time point corresponding energy distribution for non-equilibrium electrons at Fig. 8 is normalized to its maximum. One can see that non-equilibrium electrons' energy distributions have quite complex shape and different behaviour in different energy bands. Practically, at all discharge stages there is a lack of non-Maxwellian electrons in the low energy band. That effect can be explained by the existence of discharge driving voltage and corresponding electrons' acceleration that results in disappearance of low energy electrons. Contrary, during all the discharge evolution, additional non-equilibrium electrons appear in the energy band near the distribution maximum. That bunch corresponds to electrons that lose practically all their velocity in the applied electric field direction after few first collisions. In that case, these electrons are accelerated again from the very beginning and can not reach higher energies. During all discharge pulse, bunches of additional non-Maxwellian electrons are also present at energies bit below the effective excitation band (co-called "pre-excitation band" for energies from 4 to 8e V). Such electrons' appearance can be related with energy losses for ionisation and excitation. Electrons participated in such non-elastic collisions, have already lost the certain portion of their energy so they must move from the high-energy band to lower one. Taking into account the continuous acceleration caused by the applied voltage, there is additional probability for electrons to fall into the pre-excitation band. Such electrons can participate in discharge current growth via step-by-step excitation and ionization elementary processes, but, of course, the role of those processes in the conditions of this simulation is quite inferior. As for the high-energy band, one can see the lack of electrons during the discharge. Losses of high-energy electrons due to the mechanism described above can not be compensated by acceleration in the electric field of driving voltage for those conditions. So discharge at voltage of 190 V, being more energetically effective than 175 V case (that demonstrates completely different discharge behaviour), still has rather small energetic efficacy. Effective electron temperature for equilibrium electrons decreases at first discharge stages from approximately 4e V at the initial stage to 2.6e V at the second maximum. At the decay stage electron temperature grows again so the energy supplied from the driving voltage during the discharge decay is spent mostly for the equilibrium electrons' heating instead of obtaining additional non-equilibrium electrons in the high-energy band.

3.2. Electrons' energy distributions for optimal applied voltages' band. Optimal discharge driving voltages band lies between 210 V and 250 V. In this band, discharge for applied voltage of 230 V is most energetically efficient. For that voltage, waveforms of discharge electron and ion current components are plotted on Fig. 9. One can see some features substantially different from the cases of lower voltages described above. First of all, the discharge pulse amplitude is much larger, but the pulse length is quite shorter. Also, one can see that for driving voltage of 230 V the second maximum related to the coplanar discharge stage (time point B) exceeds significantly the first maximum corresponding to the electron avalanche at the volume discharge stage (point A). Finally, discharge decay has slightly non-exponential shape (especially, at the B-C time interval and also at late discharge stages after 250 ns).

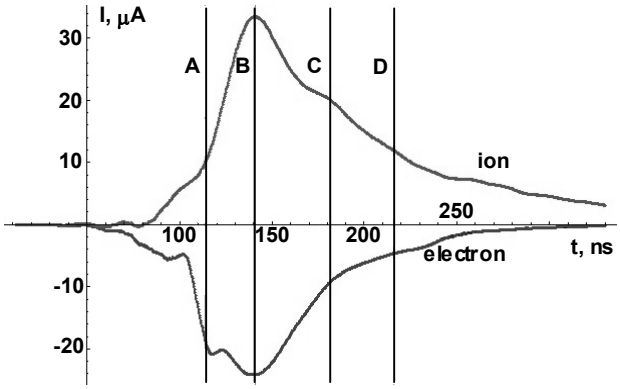

Fig. 9. Waveforms for ion end electron components of total discharge current. U = 230V

Fig. 10 shows the electrons' energy distributions at the most interesting time points of the first maximum of electron current (A), the second maximum of ion current (main for driving voltages above 210 V) related to the coplanar discharge stage (B), the stage of non-exponential slow decay (C) and the stage of the final decay (D). At the time point A (Fig. 10a) electron energy distribution has a smooth but non-Maxwellian shape mostly because in the high-energy band it decreases faster than Maxwellian function. Taking into account that it is a final time point of the rapidly growing electron avalanche, one can see that energy distribution has some transient shape of morphing from rapidly decreasing Druyvesteynian to Maxwellian case. Consequently distribution of non-equilibrium electrons at that time point has a large bunch of additional particles in pre-excitation band. However, that band corresponds to lower energies in comparison with such bands for lower voltages.

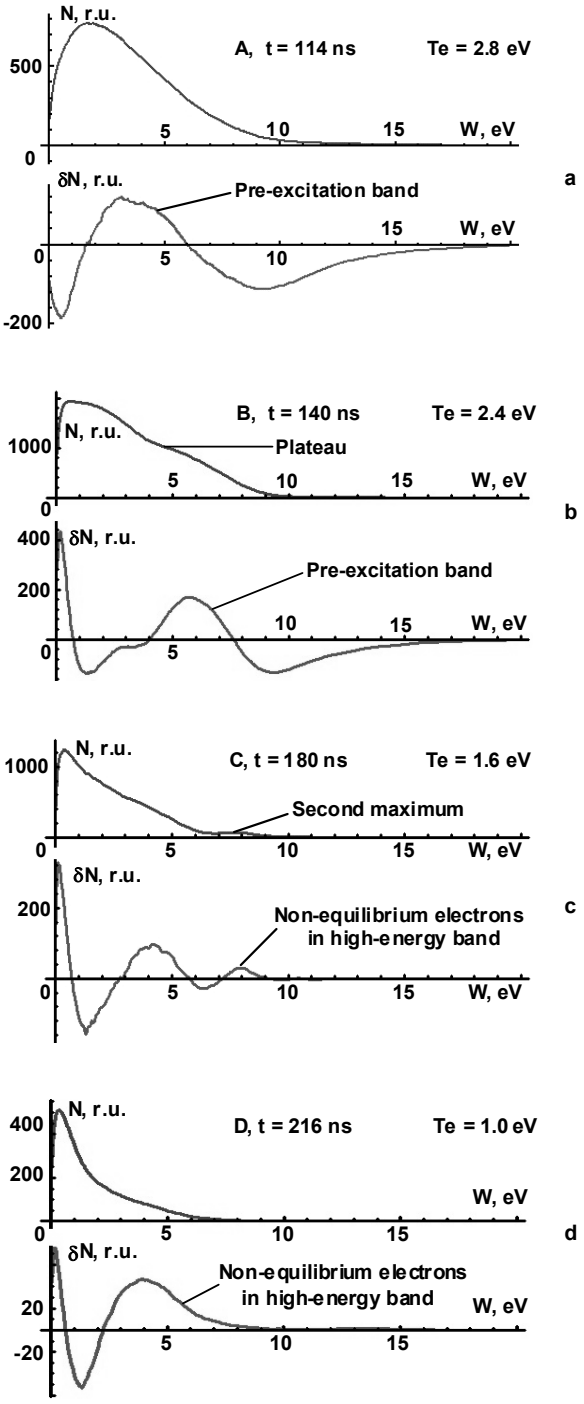

Fig. 10. Electrons' energy distributions and their differences from the nearest corresponding Maxwellian functions. U = 230V

In the high-energy band one can see a lack of non-equilibrium electrons. At the maximum of discharge current (time point B, Fig. 10b), most of electrons form more Maxwellian-like distribution. Non-equilibrium electrons' distribution has more high-energetic pre-excitation band in comparison with the previous time point. That band has a shape of plateau on the decreasing part of the main distribution. Formation of such a plateau can be explained by influence of electrons accelerated between coplanar electrodes during the previous discharge stage and formed some sort of electron beam there. One can see these electrons in coplanar mode region of their distribution function upon vX–vY velocity components at the initial discharge stage (Fig. 11a).

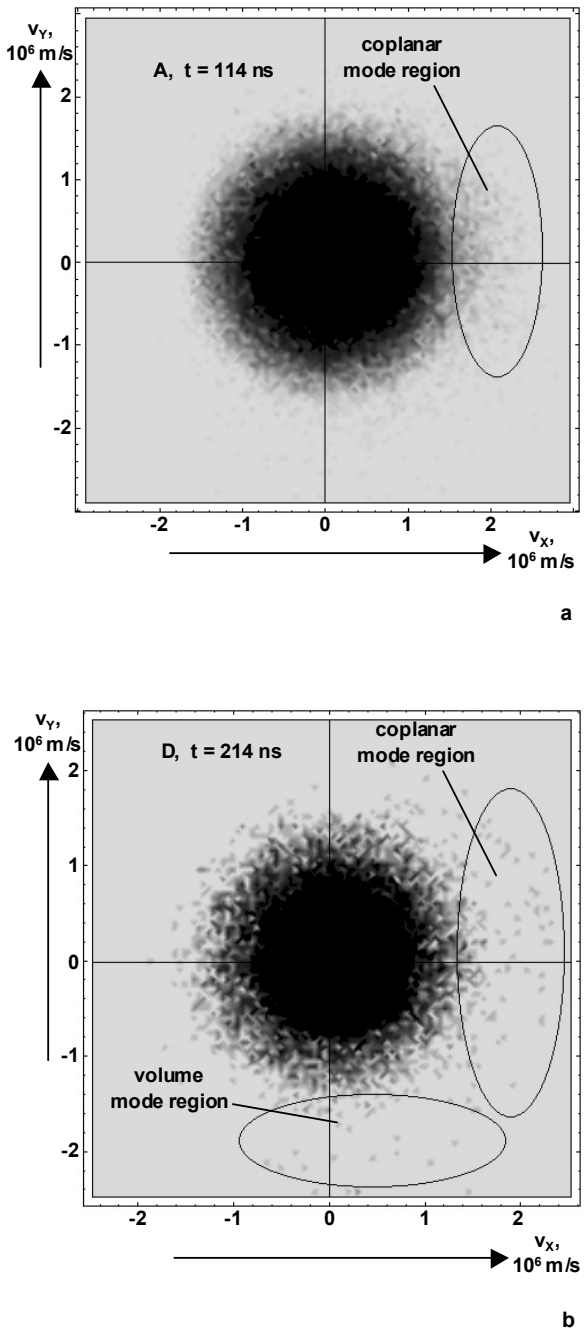

Fig. 11. Electrons' distributions upon v_X–v_Y velocity components for time points of discharge ignition (a) and decay (b). U = 230V

At the time point C one can see that discharge decay is slowed down and becomes non-exponential. That is a characteristic feature of microplasma pulse discharge in optimal voltage band. Electrons' energy distribution even has a second maximum at this moment (Fig. 10c). So some sort of electron beam is formed inside the cell at this time interval. Practically, such a beam exists between coplanar electrodes during all discharge stages with significant current (see coplanar mode regions at the vX–vY velocity distributions, Fig. 11). At the time point C this beam is producing a significant number of additional ionizations when the total current is already decaying. So these additional electrons show themselves as second maximum of total energy distribution, whereas at different time points

their amount is relatively small so only plateau is formed. Note that at late phase of discharge decay (time interval 250–260 ns, see Fig. 9) electron current decreasing becomes non-exponential once more. So one can see that role of additional ionisation in the coplanar electric field at the stage of discharge decay periodically becomes more significant than processes in the volume field that is practically localised near the **C1** coplanar electrode during this late discharge stage. One can also see that non-equilibrium electrons' energy distribution at the time point C is positive in the pre-excitation band as well as ones for previous time points but unlike them it has insignificant negative values in the high-energy band. Such a feature remains intact at later exponential decay stages (time point D, Fig. 10d) when non-equilibrium electrons amount is positive not only in the pre-excitation band but also in the high-energy band, so additional excitations and ionisations take place at discharge decay stage and this leads to energy efficacy increasing.

Fig. 11 shows the evolution of electrons distribution upon velocity components. As it was mentioned above, coplanar mode region here contains additional electrons practically during all of the discharge pulse. Even main isotropic part is slightly shifted towards the positive values of vX component. Volume mode region also contains additional non-equilibrium electrons but their amount is much smaller than for the coplanar one at the discharge first stages (Fig. 11a). At the late stages of discharge decay that difference is decreased because at that stages the volume electric field is localised near the **C1** coplanar electrode and can effectively accelerate electrons appearing here due to the secondary ion-electron emission.

3.3. Electrons' energy distributions for higher applied voltages. One can see that optimal discharge driving voltages' band is characterised by the existence of additional non-equilibrium electrons in the high-energy band, so additional excitation and ionisation occur and energy efficacy of discharge radiation is increased. That is not correct for higher applied voltages.

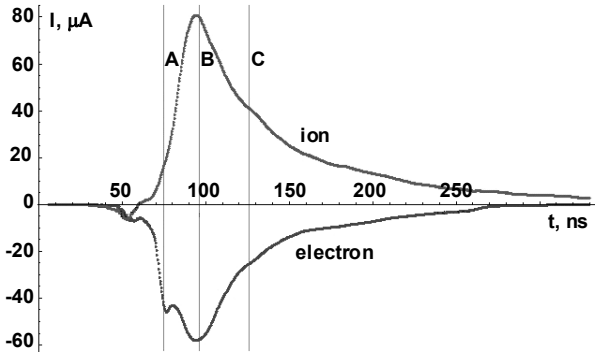

Fig. 12. Waveforms for ion end electron components of total discharge current. U = 290V

As one can see from Fig. 12, the pulse of discharge current here becomes shorter due to the faster accumulation of the wall electric charge shielding the applied voltage. The discharge current pulse is almost similar to the case of optimal voltages but its decay stage is closer to the exponential shape.

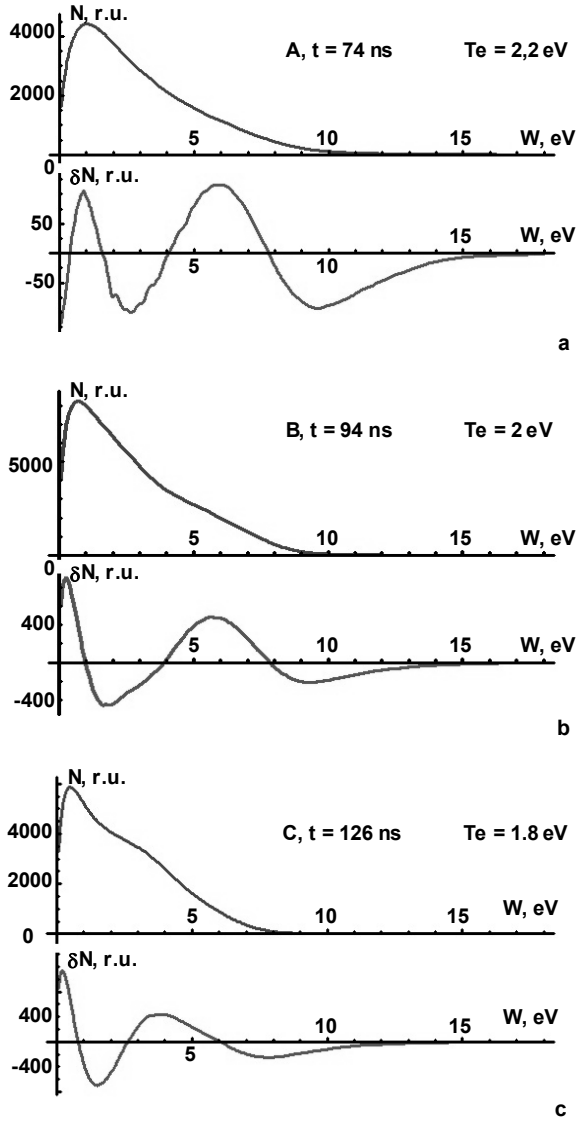

Fig. 13. Electrons' energy distributions and their differences from the nearest corresponding Maxwellian functions. U = 290V

Electrons' energy distributions at the time point of electron current maximum (point A on Fig. 12) is very close to Maxwellian shape as one can see from Fig.13a (amplitude of non-equilibrium electrons' energy distribution is only about 1 % of main distribution maximum value). At the main current maximum, difference between energy distribution and nearest Maxwellian function increases, but not to the values that characterize the optimal driving voltages' band (compare Fig. 13b and Fig. 10b). For instance, plateau at that time point for 290 V driving voltage is much less expressed than for the optimal voltage of 230 V. Moreover, at the later stage of the discharge decay one can see the lack of non-equilibrium electrons (Fig. 13c), like the case of low discharge driving voltages and quite unlike to the optimal driving voltages' band. That can be explained by the fact of more intensive elementary processes at initial discharge stages due to the larger energy obtained by each electron on its free path. So electrons fall from the high-energy band more effectively and, at the stage of discharge decay, their amount in that band is not enough for effective excitation and ionization. As a result, energy efficacy of UV photons radiation from the discharge decreases. At Fig. 13c, one can see the plateau formation on the main energy distribution function in the pre-excitation band (time point C on Fig. 12). But corresponding slowing of the discharge decay is significantly weaker than for the 230 V driving voltage case (compare Fig. 13c and Fig. 10 c).

From Fig.14 one can see that distribution upon vX–vY velocity components for higher driving voltages like 290 V has much more Maxwellian-like, rapidly decaying main isotropic part. Volume and coplanar modes' regions contain approximately equal amounts of non-equilibrium electrons because acceleration of electrons by the volume electric field is more effective in comparison to 230 V driving voltage. Taking into account the fact that excitation and ionization are more effective in the coplanar region one can conclude that such a distribution's capability of discharge sustaining and UV photons radiation is less in comparison with the 230 V driving voltage case (much more additional non-equilibrium electrons appear in the coplanar mode region for optimal discharge voltages).

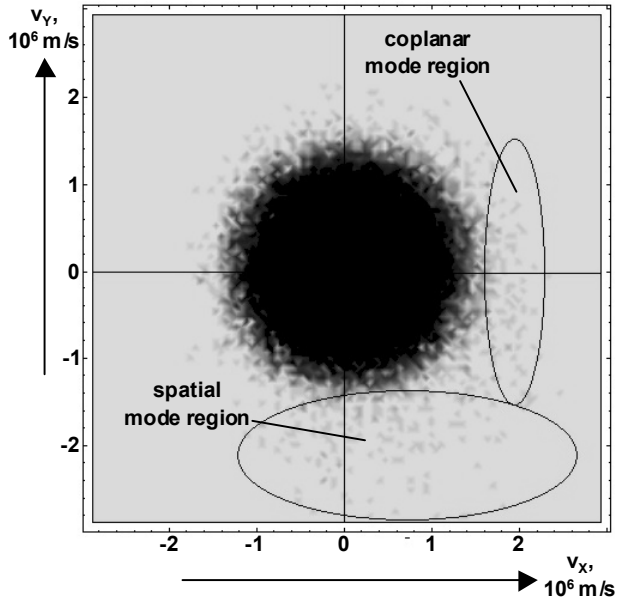

Fig. 14. Electrons' distribution upon v_X-v_Y velocity components for time point of maximal discharge current, t = 94 ns. U = 290V

3.4. Comparison of different voltage bands. Fig. 15 shows the electron temperature (average energy) evolution during the discharge pulse for driving voltages' values considered above. One can see that for lower applied voltages, higher electron temperatures characterize the discharge during all its pulse because larger part of energy supplied from the external voltage source is spent to excitation and ionization for more energetically efficient higher discharge voltages. For lower voltages, larger part of that energy is spent to electrons' heating.

For 175 V driving voltage, electrons' energy distributions have a quite irregular shape (see Fig. 3) with large noise component. So the electron temperature behaviour here is also different in comparison to the relatively close driving voltage value of 190 V. Electron temperature is monotonously decreasing with time for 175 V applied voltage but for the 190 V case one can see the expressed minimum corresponding to the time point between two maximums of the discharge current waveform (time point C on Fig. 5). Before that minimum (after the first maximum of discharge ion current), energy of the driving voltage source is effectively spent to excitation and ionisation. After that, most part of that energy is spent again for the electrons' heating because the electric potential configuration after that time point makes non-elastic collision insignificant.

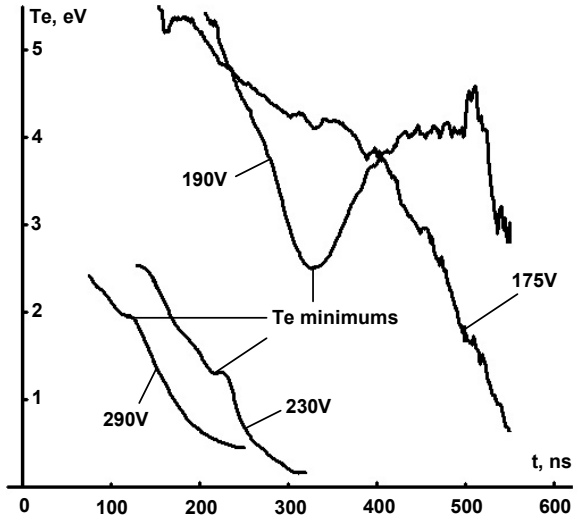

Fig. 15. Discharge electron temperature evolution for different driving voltages

For higher discharge voltages (230 V and 290 V), electron temperature minimum also exists but it is expressed much weaker so the electron temperature increase after it is inferior and quickly changes to decrease.

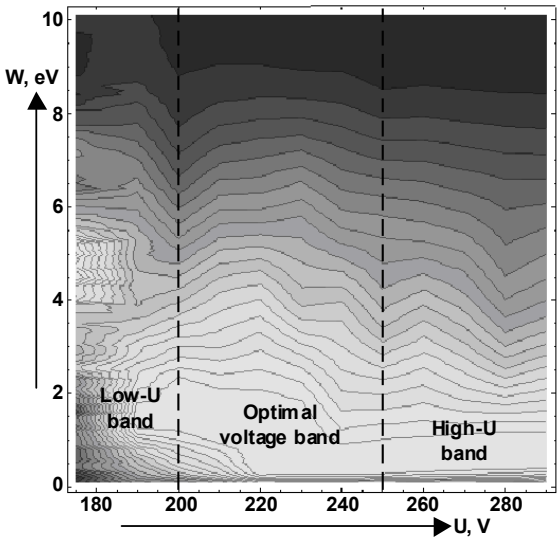

Fig. 16. Normalized electrons' energy distribution function for time points of discharge current maximum (contour plot) in the driving voltages' band 175V–290V

Note also that electron temperature for such voltages is decreased during the discharge pulse. It can be explained by larger electric field inside the cell that can accelerate electrons enough for effective ionisation and excitation up to the very last stages of the discharge current pulse. Spending more energy in non-elastic collisions, discharge for optimal driving voltage of 230 V reaches lower electron temperatures at decay stage.

Figs. 16–18 show the dependencies of different characteristics of microplasma discharge upon its driving voltage. First of all, Fig. 16 presents the normalized electrons' energy distribution function in the form of contour plot. Each contour represents equal level of such normalized distribution. Normalization was performed in order to make possible the comparison between functions that are very different in absolute values.

One can see that lower driving voltages like 175 V and 190 V are characterized by the irregular behaviour of the distribution function due to the significant noise component. For voltages above 200 V noise influence is much weaker. For the voltage band near the optimal values (200–250 V) distribution function is decreasing slower then ones for adjacent bands. Taking into account that electron temperature in that band is lower than one for low voltages (see Fig. 15), it means relatively larger numbers of high-energy non-equilibrium electrons those can form some plateau-like structure on decreasing part of energy distribution function. In that case energetic efficiency of the discharge UV radiation is increased. For driving voltages above 260 V, electron temperature at discharge current maximum is decreased even more and amount of additional non-equilibrium electrons is also decreased. Consequently the discharge energetic efficiency is decreased as well.

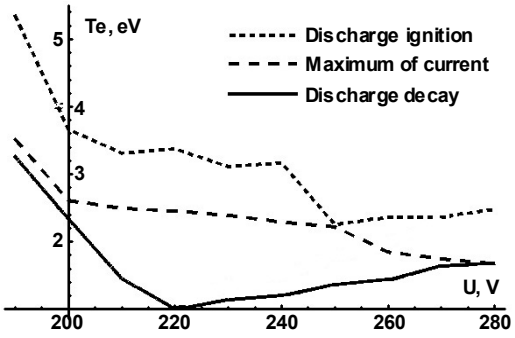

Fig. 17. Discharge electron temperature dependence upon the driving voltage

Electron temperature dependences upon the discharge driving voltage are shown on Fig. 17 for the characteristic time points of respective discharge current pulses, i.e. the ignition of discharge (sharp maximum of electron current, end of initial electron avalanche – time point A on Fig. 9 and Fig. 12), maximum of current – time point when disharge total current reachs its maximal value (time point B), discharge decay – time point when discharge current is halved in comparison to its maximum (near time point C). One can see that those plots are decreasing monotonously with discharge voltage increasing for first two stages and have a minimum near the optimal driven voltage for the discharge decay stage. As was mentioned above lower electron temperatures for higher applied voltages at the first stages of the discharge pulse can be explained by increasing of efficiency of the energy transfer from external applied voltage to excitation and ionisation. Contrary, at the stage of discharge decay such a transfer is most efficient in the optimal driving voltages' band near 220–230 V so the electrons' heating here is less efficient and electron temperature has a minimum.

According to Fig. 17, there can be some optimal shape of the driving voltage pulse that makes possible to obtain a maximal energetic efficacy. For instance, one can supply a larger voltage like 280–290V at first discharge stages and switch to the optmal voltage like 220–230V at the decay stage in order to keep energy transfer rate from the applied voltage to excitation and ionization on the highest level possible. Hovewer, behaviour of the discharge current pulse for the complex form of driving voltage pulse needs additional investigations.

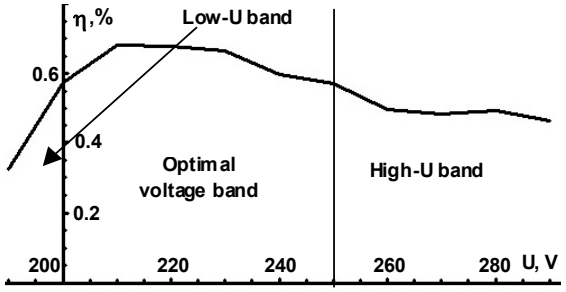

Fig. 18. Dependence of the UV photons (147, 150 and 173 nm wavelength) emission energetic efficacy upon the discharge driving voltage

Fig. 18 shows the energetic efiicacy of UV radiation (photons of three most important wavelengthes – 147, 150 and 173 nm) for various applied voltages. It reaches its maximal valuein the optimal discharge driving voltage band and decreasing both for the lower and higher voltages. Of course, in all cases energetic efficacy is quite low, but in the optimal driving voltages' band its value is about 50 % higher than respective one for adjacent bands.

3.5. Influence of striation structures' formation. According to the simulation results, formation of striation structures is possible in the optimal and high voltages' bands. These structures occur as additional bunches of ions that can significantly disturb the spatial profile of the electric potential inside the cell. Such structures are formed at the initial discharge stage and their magnitude reach maximum at the end of initial electron avalanche (time points A at current waveforms above). Fig. 19 shows these structures for optimal discharge driving voltage of 230 V. Here they are already formed and have significant influence on the electric potential profile.

Fig. 19a shows two additional ion bunches already formed near the main discharge column. They disturb the electric charge density profile and create additional maximums of positive space charge. Such a disturbance leads to the appearance of additional electric field near those striation structures. According to Fig. 19a, that field must have a component along the x axis (along the coplanar electric field) that can accelerate electrons in this direction adding their amount in the coplanar mode region (see Fig. 11 and Fig. 14). So, as a result, striation structures' formation can change the energy distribution function and improve the discharge UV radiation energetic efficiency.

Spatial profile of the electric potential with striation structures is shown on Fig. 19b. The main discharge column here is yet on the initial stage of evolution but negative wall charge in the address electrode region is already significant. Striation structures are present as localized potential maxima. In more details these structures are shown on Fig. 19c (scaling of Fig. 19b without large negative potentials' region) where additional electric field with significant x component is expressed well.

Similar plots for the higher applied voltage of 290 V are shown on Fig. 20. Note that striation structures at that conditions are even more significant and appears faster (along with the faster discharge evolution - main positive column on Fig. 20b is developed slightly more than one shown on Fig. 19b). But, on the other hand, lifetimes of these structures for higher voltages are also shorter so they produce electrons in coplanar mode region for smaller time than for optimal discharge voltage of 230 V.

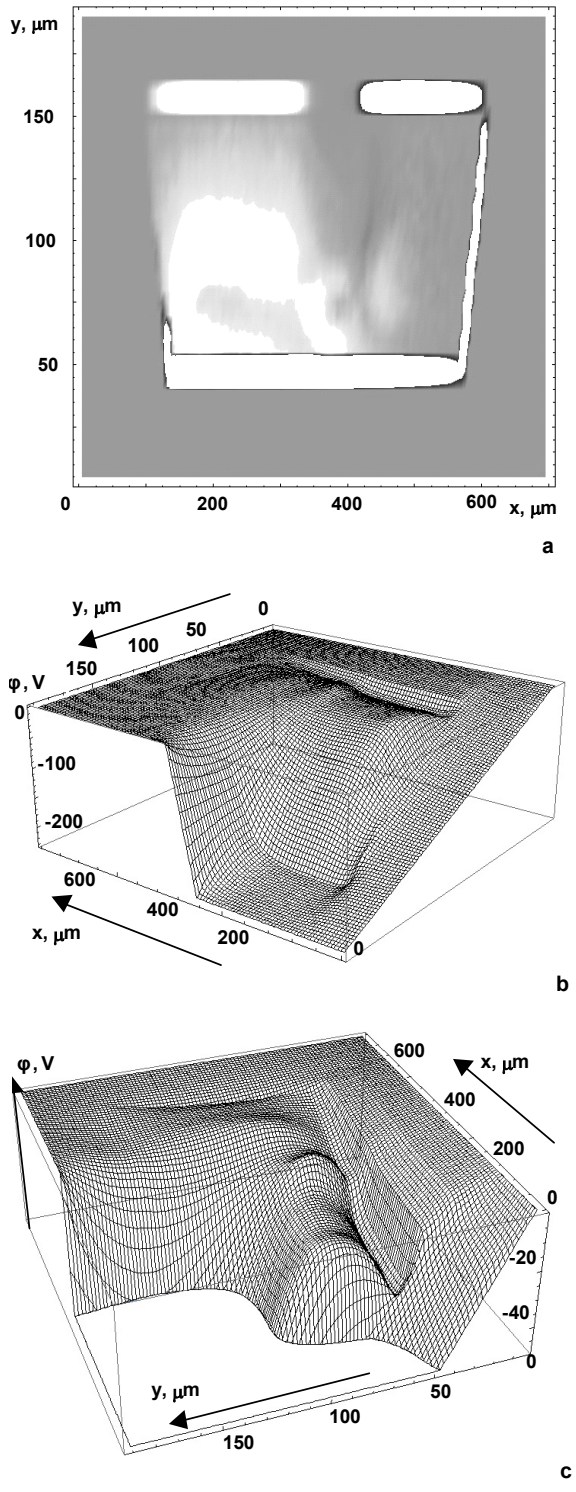

Fig. 19. Electric charge density (a) and potential (b,c) spatial distributions for the time point of first sharp electron current maximum, t = 114 ns. U = 230V

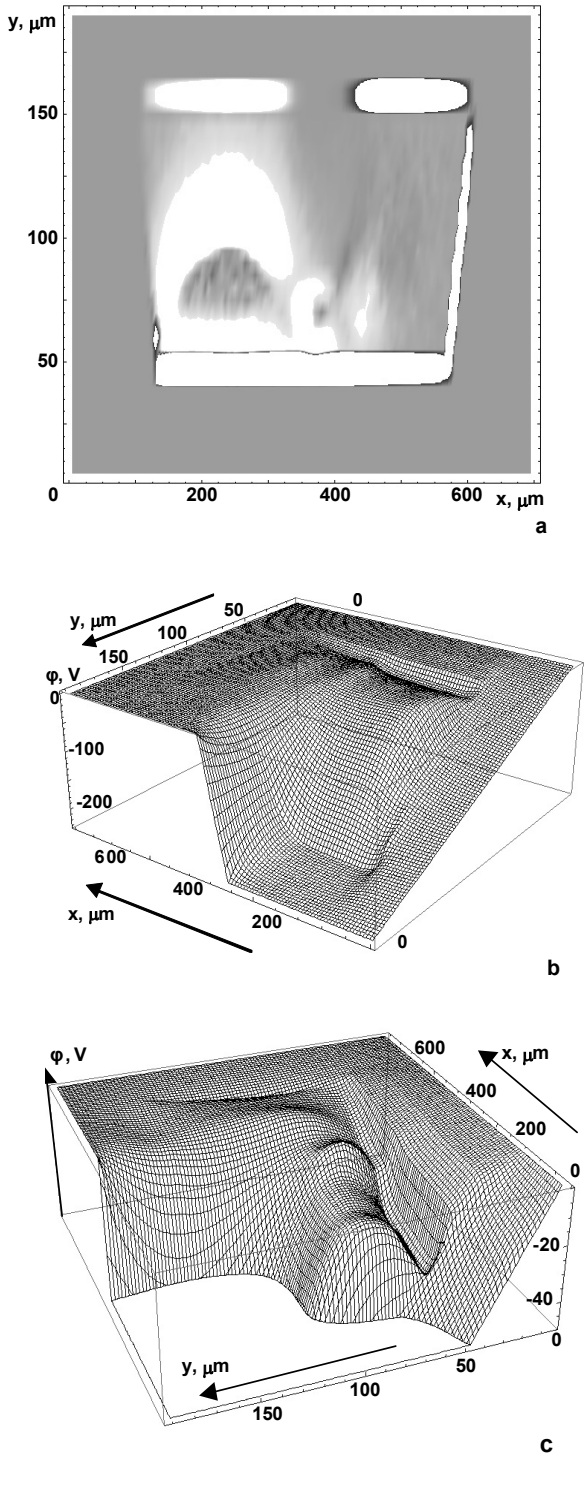

Fig. 20. Electric charge density (a) and potential (b,c) spatial distributions for the time point of first sharp electron current maximum, t = 94 ns. U = 290V

Note that both for 230 V and 290 V driving voltages, additional electric field of the striation structures accelerates electrons in positive x direction much more than in negative (Fig. 19c, Fig. 20c).

So striation structures are formed in optimal and high bands of applied voltages as positive space charge bunches those can accelerate electrons in the same direction with the coplanar electric field. That can increase the amount of electrons in high-energy band and improve the discharge UV radiation efficacy.

3.6. Ions' energy distribution. Ions in the discharge in Ne-Xe gas mixture have masses much larger than electrons so their motion is much slower as well as rates of elementary processes per one particle. Maxwellization time for ions is also much greater than for electrons. Consequently, ions' energy distribution function must be strongly different from the equilibrium one. Simulation results confirm this conclusion. Fig. 21a presents the energy distribution function for Xe+ atomic ions for the maximum of discharge current at the optimal driving voltage of 230V. At the different time points, energy distribution functions have a similar shape for all

sorts of ions and all driving voltages. One can see that Maxwellian approximation doesn't fit well to such a distribution. Contrary, Dryuvesteyn distribution function coincides with the distribution obtained from simulation with good accuracy, especially in the decreasing band. Such distributions are widely used [11, 18] for gas discharges where maxwellization for certain sort of particles is not yet completed. Width of the Dryuvesteynian energy distribution gives the estimation for average energy obtained by each ion between consecutive collisions. For our simulation, its value is about 2e V. From Fig. 21b one can conclude that ions' distribution upon vX-vY velocity components is effectively symmetrical but slightly shifted towards positive values of vY due to the ions' acceleration towards the negative **C1** coplanar electrode.

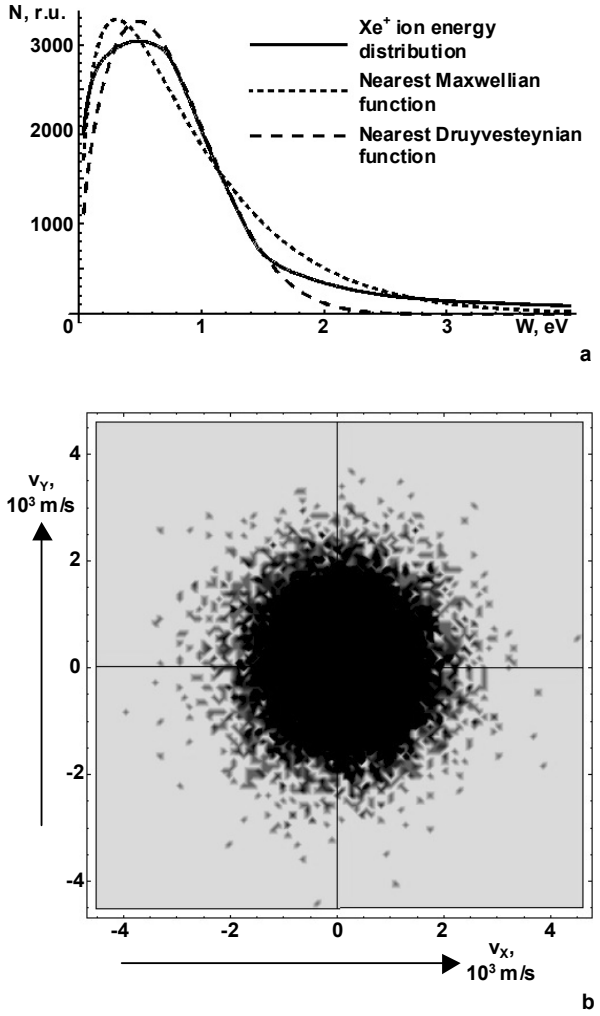

Fig. 21. Xe^+ ions' distributions upon their total energy (a) and v_X-v_Y velocity components(b) for time point of maximal discharge current. U = 230V

As one can see from chapter 3.5, strong difference between electrons' and ions' energy distributions corresponds to the formation of inhomogeneous structures of space charge inside the dielectric cell. Formation of main bunch of positive charge like shown on Fig. 20b leads to the slowing of electrons that move towards positive electrodes. That means the end of initial volume electron avalanche and beginning of coplanar discharge stage.

4. Conclusions. Microplasma pulse discharge inside the coplanar dielectric cell has a different operation modes corresponding to the different applied voltages. For very low voltages (175 V) that discharge have a volume behavior and quite small current, so energetic efficacy is quite low. For low driving voltages (190 V) discharge mainly switches to coplanar mode. Discharge current pulse has two maxima corresponding to coplanar and volume modes. Electrons' energy distribution during a discharge has a very Maxwellian-like shape with lack of high-energy electrons so energy transfer from driving voltage source to UV radiation is not quite efficient. There is an optimal driving voltages band between 210 V and 250 V. For these voltages, energy distribution functions have plateau-like features due to the electrons' acceleration in the coplanar electric field. There are additional non-equilibrium electrons in the high-energy band so additional elementary processes like excitation and ionization occur at the discharge decay stage. As a result, energy efficacy of UV radiation from discharge has maximal value. For higher voltages such processes take place at the first discharge stages, but there is a lack of high-energy electrons at the decay stage due to the spending of such electrons to elementary processes at previous stages. So energy efficacy here is larger than one for low voltages but smaller than for the optimal voltages. Ions' energy distribution is Dryuvesteynian-like due to their much larger maxwellization time. Striation structures appear near the address electrodes for optimal and higher voltages, provide additional electric field for electrons acceleration in coplanar direction and, consequently, increase the discharge energy efficacy.

This work was partially supported by LG Electronics Inc. Authors thank to I. O. Anisimov and E. V. Martysh for fruitful discussion and valuable advices.

1. *Boeuf J.-P.* Plasma display panels: physics, recent developments and key issues // J. Phys. D: App. Phys. – 2003. – Vol. 36. – P. R53–R79. 2. *Iza F., Yang S. S., Kim H. C., Lee J. K.*. The mechanism of striation formation in plasma display panels // J. App. Phys. – 2005. – Vol.98. – P. 043302-1-043302-5. 3. *Kelnyk O. I., Samchuk O. V.* Current waveforms for pulse microdischarge inside dielectric cell // Prob. Atom. Sci. & Tech. Ser.: Plasma Phys. – 2010. – Vol. 16. – coming. 4. *Kelnyk O. I., Samchuk O. V.*. Microplasma Discharge Striation in the PDP Cell // Prob. Atom. Sci. & Tech. Ser.: Plasma Phys. – 2010. – Vol. 16. – coming. 5. *Keto J. W., Gleason R. E., Walters G. K.* Production mechanisms and radiative lifetimes of argon and xenon emitting in the ultraviolet // Phys. Rev. Lett. – 1974. – Vol. 33. – P. 1365–1368. 6. *Khudik V., Nagorny V., Shvydky A.* Three-dimensional PIC/MC simulations of the sustain discharge pulse in an AC PDP // J. SID. – 2005. – Vol.13/2. – P. 147–153. 7. *Lainhart E., Dakin D. A., Maenchen J. E.* Characteristics of electron-beam-excited Xe2 at low pressures as a vacuum ultraviolet source // J. App. Phys. – 1988. – Vol. 64(4). – P. 1679–1690. 8. *Meunier J., Belenguer Ph., Boeuf J.-P.* Numerical model of an AC plasma display panel cell in neon-xenon mixtures // J. App. Phys. – 1995. – Vol. 78(2). –, P. 731–745. 9. *Oh Ju.-S., Sakai O., Tachibana K.* Influence of sustaining frequency on the production efficiency of excited Xe atoms studied in unit cell microplasma for ACPDPs using spectroscopic diagnostics // J. SID. – 2007. – Vol.15/5. – P. 297–308. 10. *Ouyang J.T., Callegari Th., Caillier B., Boeuf J.-P.* Large gap plasma display cell with auxiliary electrodes: macro-cell experiments and two-dimensional modelling // J. Phys. D: App. Phys. – 2003. – Vol. 36. – P. 1959–1966. 11. *Райзер Ю. П.* Основы современной физики газоразрядных процессов. – М., –1980. 12. *Samchuk O. V., Kelnyk O. I., Anisimov I. O.* Pulse discharge in the dielectric cell: simulation via PIC method // Prob. Atom. Sci. & Tech. Ser.: Plasma Phys. – 2007. – Vol. 13, № 1. – P. 148–150. 13. *Samchuk O. V., Kelnyk O. I.* Excimer ions' generation in the Ne-Xe pulse microdischarge inside the dielectric cell // Book Abstr. III Centr. Europ. Symp. Plasma Chem. – Kyiv, 2009. – P. 110–111. 14. *Самчук О. В., Кельник О. І.* Еволюція функції розподілу електронів у мікроплазмовому розряді всередині діелектричної комірки // Сучасні проблеми теоретичної фізики. Матер. наук. конф. ІТФ НАНУ. – Київ, 2009. – С. 60. 15. *Samchuk O. V., Kelnyk O. I.* Anisotropy of velocity distribution function in the microdischarge inside dielectric cell // Proc. X Int. Conf. App. Phys. – Kyiv, 2010. – P. 187–188. 16. *Shon Ch. H., Lee Ja. K.* Striation phenomenon in the plasma display panel // Phys. Plasmas. – 2001. – Vol. 8, № 3. – P. 1070–1080. 17. *Shuo F., Feng H., Ouyang Ji-T.* Mechanism of striation in dielectric barrier discharge // Chin. Phys. Lett. – 2007. – Vol.24, № 8. – P. 2305–2307. 18. *Смирнов Б. М.* Ионы и возбужденные атомы в плазме. – М., – 1974. 19. *Tae H.-S., Seo H. Ju., Jeong D.-Ch. et al.* Analysis of microdischarge characteristics induced by synchronized auxiliary address pulse based on cross-sectional infrared observation in AC plasma display panel // IEEE Trans. Plasma Sci. – 2005. – Vol. 33, № 2. – P. 931–939.

Submitted 19.09.10

UDC 533.9

A. Knurenko, post grad. stud.,
E. Martysh, Ph. D.,
V. Sidorenko, Ph. D.

SPACE WEATHER AND PROCESSES IN THE EARTH'S MAGNETOSPHERE

Вивчення взаємодії сонячного вітру (космічної погоди) з планетарними магнітосферами, в основному, базується на фізиці намагніченої плазми. Магнітне поле Сонця і викиди плазми з нього безпосередньо впливають на Землю і на всю Сонячну систему. Процеси взаємодії сонячного вітру з магнітосферою Землі можуть відбуватися на різних рівнях.

Геомагнітна активність може бути розділена на дві основні категорії: суббурі та бурі. Геомагнітні бурі можуть порушити зв'язок і навігаційне обладнання, пошкодити супутники та навіть привести до відключень електромереж. Сильні магнітні бурі є відносно рідкісним явищем. Енергія для створення таких бур надходить з сильного сонячного вітру. Фізичні процеси розсіювання цієї енергії поділяються на процеси з прямою передачею енергії і не прямими зв'язками. Головною особливістю суббур є прискорення і збудження частинок плазмового шару на геостаціонарній висоті.

Ключові слова: Космічна погода, геомагнітна активність, магнітосфера, суббурі, плазма.

The study of the solar wind and Space Weather interaction with planetary magnetospheres basically is the investigation of the physics of flowing magnetized plasmas. The Sun's magnetic field and releases of plasma directly affect Earth and the rest of the solar system. Processes in Earth's magnetospheres occur on a variety of scales.

Geomagnetic activity can be divided into two main categories: substorms and storms. These storms and substorms can disrupt communications and navigational equipment, damage satellites, and even cause blackouts. Magnetic storms are relatively rare phenomena. Energy for a substorm creation originates from the solar wind. The physical processes involved in dissipation of this energy are divided into directly driven processes and loading-unloading processes. The main feature of substorm is injection and excitation of plasma sheet particles into the geostationary altitude.

Key words: Space Weather, geomagnetic activity, magnetospheres, substorm, plasma.

Introduction. Space Weather is the concept of changing environmental conditions in near-Earth space. It is distinct from the concept of weather within a planetary atmosphere, and deals with phenomena involving ambient plasma, magnetic fields, radiation and other matter in space. "Space Weather" often implicitly means the conditions in near-Earth space within the magnetosphere, but it is also studied in interplanetary space.[1]

In own solar system, space weather is greatly influenced by the speed and density of the solar wind and the interplanetary magnetic field (IMF) carried by the solar wind plasma. A different of physical phenomena are associated with space weather, including geomagnetic storms and substorms, energization of the Van Allen radiation belts, ionospheric disturbances and scintillation, aurora and geomagnetically induced currents at Earth's surface. Coronal Mass Ejections and their associated shock waves are also important drivers of space weather as they can compress the magnetosphere and trigger geomagnetic storms. Solar Energetic Particles, accelerated by coronal mass ejections or solar flares, are also an important driver of space weather as they can damage electronics onboard spacecraft through induced electric currents, and threaten the life of astronauts. Space weather exerts a profound influence in several areas related to space exploration and development. Changing geomagnetic conditions can induce changes in atmospheric density causing the rapid degradation of spacecraft altitude in Low Earth orbit. Geomagnetic storms due to increased solar activity can potentially blind sensors aboard spacecraft, or interfere with on-board electronics. An understanding of space environmental conditions is also important in designing shielding and life support systems for manned spacecraft. There is also some concern that geomagnetic storms may also expose conventional aircraft flying at high altitudes to increased amounts of radiation.[2]

Processes in planetary magnetospheres occur on a variety of scales. .The Earth has a dipole magnetic moment of 8×10^{15} Tm3 that produces a magnetic field strength at the equator on the Earth's surface of about 3×10^{-5} T, and at 10 Earth radii (RE) of about 3×10^{-8} T. The solar wind interaction slightly more than doubles this value on the dayside so that the pressure in the magnetic field is about 2 nPa. The sun emits a magnetized plasma consisting of mainly protons and electrons with a density of about 7 cm^{-3} at the orbit of the Earth at a velocity of about 440 km s^{-1}. The pressure exerted by this flowing plasma is also about 2 nPa, thus balancing the pressure exerted by the magnetospheric field.

Consequence of space weather is geomagnetic activity. Geomagnetic activity can be divided into two main categories, substorms and storms.[3]

Space Weather and modern technologies. Space Weather events have been noted to affect, or even disrupt, human technologies since the development and deployment of the first electrical telegraphs in the 1840. Electrical currents induced in the Earth by ionosphere and magnetosphere processes caused serious disruptions of telegraphy for decades. Indeed, the great solar storm of 1859 disrupted telegraph operations around the world, causing articles to be published in many major newspapers at that time. Degradation and disruption of wireless signals by space weather effects on the ionosphere have been observed ever since Marconi sent his first transmissions across the Atlantic in December 1901.

Military needs for space situational awareness were evident long before the official beginning of the space age. During World War II, radar signals were a primary element of British defense against the Luftwaffe. Solar radio noise would at times fill the airways, prompting investigations of German jamming capabilities. In fact, particularly severe radar jamming during a large solar event in 1942 led to the discovery of solar radio bursts (only reported following the end of the war). The first measurement of high energy solar cosmic rays was also made during this solar event (by ground-based detectors) and was also reported following the war.

The first transatlantic telephone cable (between Newfoundland and Scotland) was disrupted by the geomagnetic storm of 1958. At the same time, the entire Toronto area lost electrical power because of the storm. Radio communications faltered during that storm in several locations. An Air Force plane loaded with passengers and flying from New Zealand to Antarctica made the 2,000-mile journey without radio contact. The first telecommunications satellite, Telstar 1, which launched on July 10, 1962, was put out of service after 8 months in orbit by a combination of natural and human-induced radiation in the Van Allen belts.

The advent of the space age demonstrated conclusively that ever-advancing technologies for both civilian and national defense purposes require an evermore sophisticated understanding of the space environment. Reliable forecasts of

changes in this environment space weather are now essential for ensuring reliable operations of both space- and ground-based systems. The operations of these systems have often encountered surprises because of solar-terrestrial effects (e.g., Barbieri and Mahmot 2004). Further, "older" problems, such as the disturbance of radar by solar radio noise, require revisiting and reanalysis in the context of newer communications technologies that use different frequencies and implementations than in the past (for instance, the Global Positioning System [GPS] and other positioning, navigation, and timing services; wireless telephony and data transmission services). Contemporary examples of space-weather impacts on many modern technical systems are schematically illustrated in figure 2–1. Details of some of these technological impacts are discussed in side-bar boxes in chapter 3 and at relevant points in the report narrative.

Space Weather Scale for Geomagnetic Storms (by National Oceanic and Atmospheric Administration's (NOAA) USA [4]**)**. Classification for geomagnetic storms has 5 types. Consider each types for geomagnetic storms and effects from these types of storms. The first of type is G5. With type is very extreme. With type storms has effects in different systems. Power systems are widespread voltage control problems and protective system problems can occur, some grid systems may experience complete collapse or blackouts. Transformers may experience damage. Spacecraft operations are may experience extensive surface charging, problems with orientation, uplink/downlink and tracking satellites. Other systems: pipeline currents can reach hundreds of amps, HF (high frequency) radio propagation may be impossible in many areas for one to two days, satellite navigation may be degraded for days, low -frequency radio navigation can be out for hours. Physical measure is Kp values, which determined every 3 hours for each substorms. For G5 Kp values is 9. Such storms are very rare. Kp values for the type of storm G5 is shown in Fig. 1.

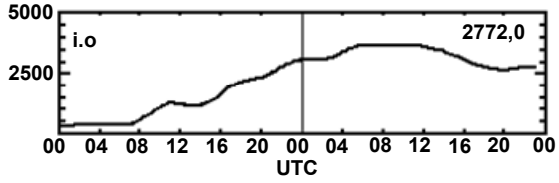

Fig. 1a. Storm magnitude index, 2003 October 29–30

The second of type is G4, severe. Power systems are possible widespread voltage control problems and some protective systems will mistakenly trip out key assets from the grid. Spacecraft operations are may experience surface charging and tracking problems, corrections may be needed for orientation problems.

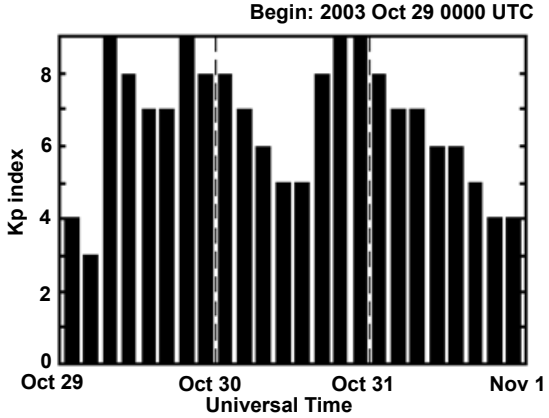

Fig. 1b. Estimated Planetary Kp index (3 hours data)

*Other systems***:** induced pipeline currents affect preventive measures, HF radio propagation sporadic, satellite navigation degraded for hours, low-frequency radio navigation disrupted. Values Kp may be equal 8 or 9. Kp values for the type of storm G4 is shown in Fig. 2.

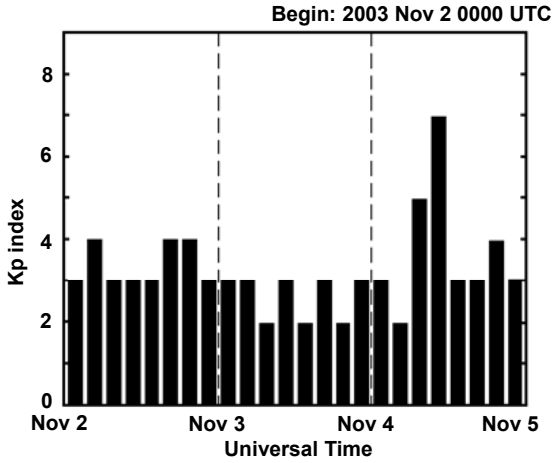

Fig. 2. Estimated Planetary Kp index (3 hour data)

The third of type is G3, strong. Power systems are voltage corrections may be required, false alarms triggered on some protection devices. *Spacecraft operations* are surface charging may occur on satellite components, drag may increase on low-Earth-orbit satellites, and corrections may be needed for orientation problems. *Other systems:* intermittent satellite navigation and low-frequency radio navigation problems may occur, HF radio may be intermittent. Values Kp is equal 7. Kp values for the type of storm G3 is shown in Fig. 3.

The fourth of type is G2, moderate. Power systems are high-latitude power systems may experience voltage alarms, long-duration storms may cause transformer damage. Spacecraft operations are corrective actions to orientation may be required by ground control; possible changes in drag affect orbit predictions. Other systems:

HF radio propagation can fade at higher latitudes. Values Kp is equal 6. Kp values for the type of storm G2 is shown in Fig. 4.

The fifth of type is G1, minor. Power systems are weak power grid fluctuations can occur. Spacecraft operations are minor impact on satellite operations possible. Other systems: migratory animals are affected at this and higher levels. Values Kp is equal 5. Kp values for the type of storm G1 is shown in Fig. 5.

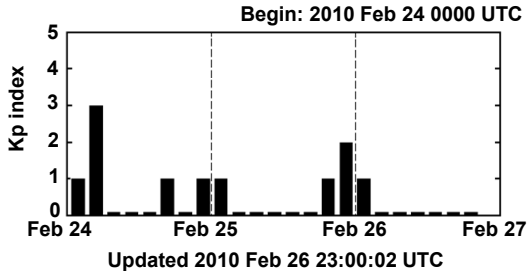

Fig. 3a. Estimated Planetary Kp index (3 hour data)

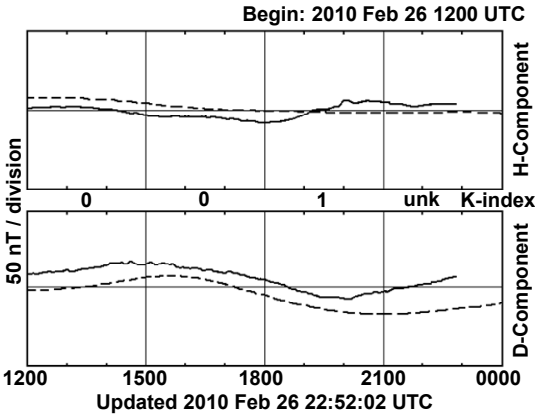

Fig. 3b. Data Boulder Magnetometer: 2010 February 26

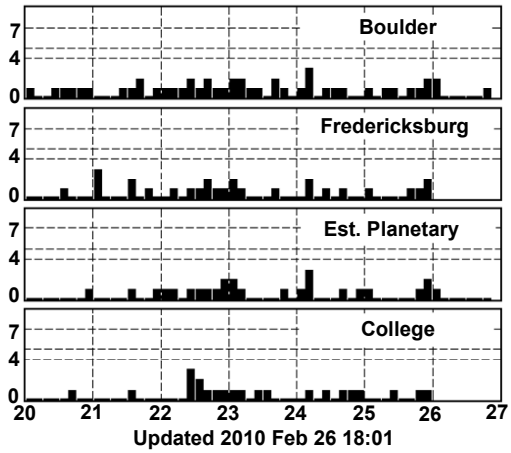

Fig. 4. 3-hour indices, 2010 February 20–27

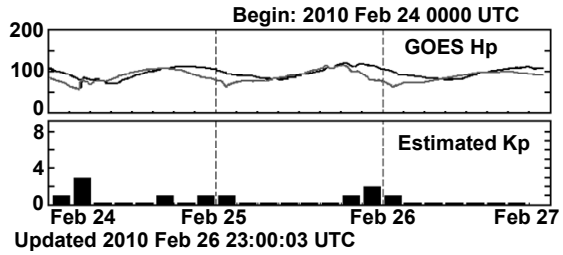

Fig. 5. Satellite Environment, 2010 February 24–26

The K-index. The K-index is a code that is related to the maximum fluctuations of horizontal components observed on a magnetometer relative to a quiet day, during a three hour interval. The conversion table from maximum fluctuation (nT) to K-index, varies from observatory to observatory in such a way that the historical rate of occurrence of certain levels of K are about the same at all observatories. In practice this means that observatories at higher geomagnetic latitude require higher levels of fluctuation for a given K-index. The conversion table for the Boulder magnetometer is shown below in Tab. 1.

Table 1. Conversion table for the Boulder magnetometer

K	nT	K	nT
0	0–5	5	70–120
1	5–10	6	120–200
2	10–20	7	200–330
3	20–40	8	330–500
4	40–70	9	> 500

We monitor the preliminary values of the K-index, minute by minute, and we notify our rapid alert customers when we exceed critical thresholds of 6, 7, and 8. The final real-time K-index is determined after the end of prescribed three hourly intervals (0000–0300, 0300–0600, ..., 2100–2400) and is used on our announcements and appears on our web site. The maximum positive and negative deviations during the 3-hour period are added together to determine the total maximum fluctuation. These maximum deviations may occur anytime during the 3-hour period. The relationship between K, Kp. The official planetary Kp index is derived by calculating a weighted average of K-indices from a network of geomagnetic observatories. Since these observatories do not report their data in real-time, it is necessary for an operations center such as ourselves to make the best estimate we can of this index based on available data. Space weather operations uses near real-time estimates of the Kp index.

Conclusions. Any country that wants to dominate the modern technologies and provide them with uninterruptible work should move to establish their National Space Weather Program. A nation must be prepared to mitigate the effects of space weather through the understanding processes in the Earth's magnetosphere.

Introduced is quite understandable for most people as a measure of magnetic activity from Space Weather. The K-index can be used both for the presentation of geomagnetic storms and to as parameter forecast providers in the future.

1. *T. D. G. Clark*, and *E. Clarke*. Space weather services for the offshore drilling industry. In Space Weather Workshop: Looking Towards a Future European Space Weather Programme. ESTEC, ESA WPP-194. – 2001. 2. *Carlowicz, M. J.*, and *R. E. Lopez*. Storms from the Sun // Surveys in Geophysics. – 2004. – Vol. 25, № 2. – P. 187–188. 3. Plasma magnetic field for near earth substorm: V International conference "Electronics and applied physics", Kyiv, 21–24 October, 2009. 4. National Oceanic and Atmospheric Administration's (NOAA). http://www.swpc.noaa.gov

Submitted 01.06.10

UDC 537.528

O. Nedybaliuk, post grad. stud.,
V. Chernyak, Dr. Sci.,
S. Olszewski, Ph. D.

DYNAMICAL PLASMA-LIQUID S Y S T E M "TORNADO-LE"

Досліджено параметри плазмово-рідинної системи із зворотно-вихровим потоком типу "торнадо". Виміряні вольт-амперні характеристики розряду в діапазоні струмів від 200 до 350 мА, при різних потоках повітря. Отримані емісійні спектри в діапазоні довжин хвиль від 200 до 1000 нм. Визначено коефіцієнти поглинання обробленої дистильованої води. Обраховані температури заселення збуджених рівніе (обертальних T_r^*, коливальних T_V^* та електронних T_e^*).

Ключові слова: плазма, розряд, плазмово-рідинна система, рідкий електрод.

Parameters of plasma-liquid system with reverse vortex flow of "tornado" type were studied. Current-voltage characteristics of discharge in current range from 200 to 350 mA at different air flows were measured. Emission spectra in wavelength from 200 to 1000 nm were registered. Absorption coefficients of pretreated distilled water were measured. Excitation temperatures (rotational T_r^*, vibrational T_V^* and electronic T_e^*) were calculated.

Key words: plasma, discharge, plasma liquid system, liquid electrode.

Introduction. Different types of discharges are used for creating plasma of atmosphere pressure: transversal arc [5], discharge in gas channel with liquid wall [6] and etc. But, these discharges are unstable. Vortex flow is used for stabilization of discharge in high-powered plasmatrons of high-pressure [4]. Reverse vortex flow of "tornado" type (RVFTT) in low-power discharges of high-pressure for stabilization in space was used [3]. Investigations were made only for discharges with solid electrodes. Discharges with liquid electrode stabilized by RVFTT were not investigated. Plasma-liquid systems of high-pressure are very interesting for medicine at present day [8]. Water cleaning from heavy metal ions is not solved problem till now.

Using discharge with liquid electrode stabilized by reverse vortex flow of "tornado" type for nanomaterials recovery at plasma quenching [1] in gas volume, with using ecological fuel like ethyl alcohol C_2H_5OH, is very perspective technology.

Results of plasma parameters investigation in plasma-liquid system with RVFTT are present in this paper. Distilled water was used as working liquid.

Experimental setup. Plasma-liquid system reactor was prepared with the DC discharge in a reverse vortex gas flow of tornado type with a "liquid" electrode (TORNADO-LE) as is shown in Fig. 1. It consists of a cylindrical quartz vessel (1) by diameter of 90 mm and height of 50 mm, sealed by the flanges at the top (2) and at the bottom (3). The vessel was filled by the work liquid (4) through the inlet pipe (5) and the level of liquid was controlled by the spray pump. The basic cylindrical T-shaped stainless steel water-cooled electrode (6) on the lower flange (3) made from stainless steel is fully immersed in the liquid.

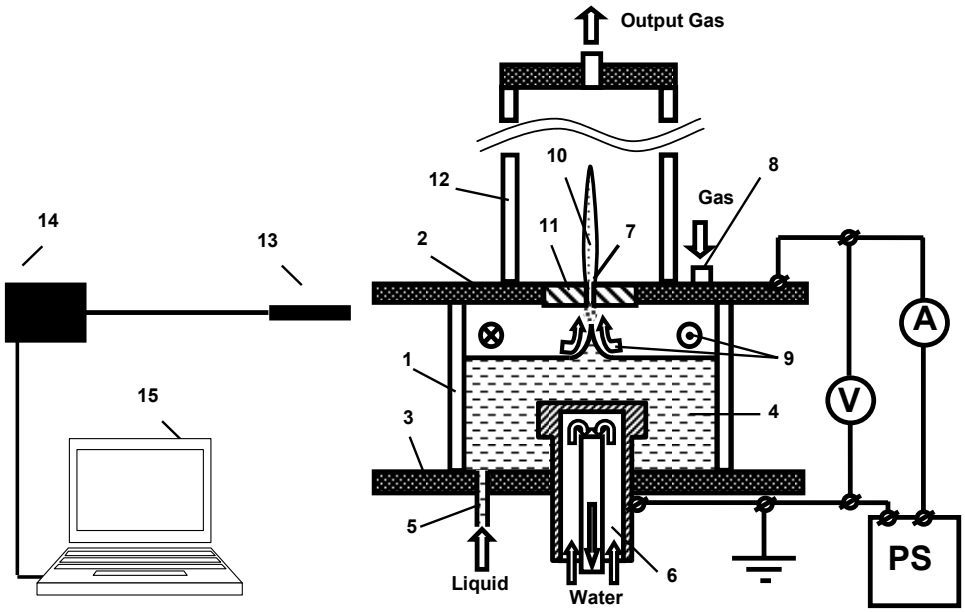

Fig. 1. Scheme of plasma-liquid system with reverse vortex flow of "tornado" type

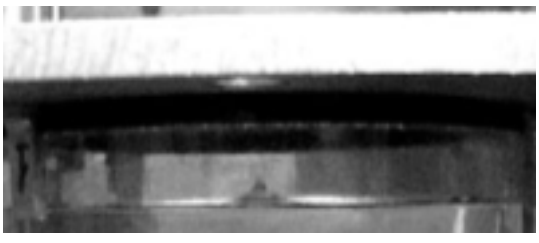

a

b

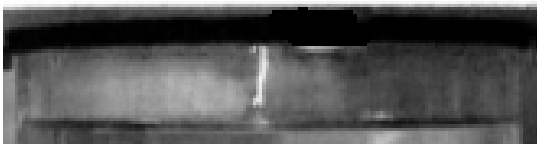

c

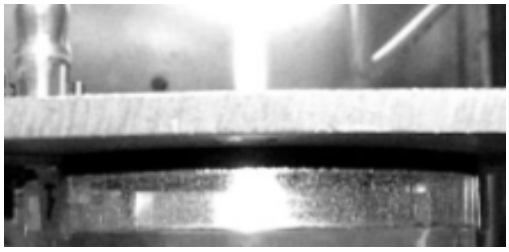

d

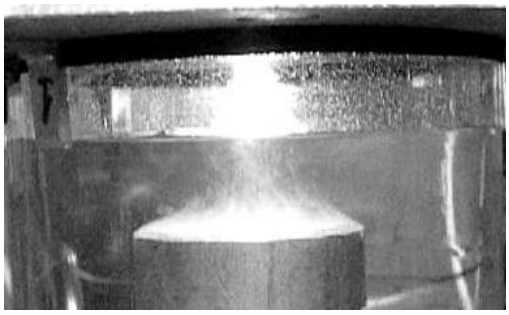

e

Fig. 2. Photo of experimental setup working on distilled water: stable water cone – a; break away of liquid drops – b); breakdown of gas gape – c; stable discharge burning – d; stable discharge burning with water electrolysis – e

The electrode on the upper flange (2) made from duralumin had a special copper hub (11) with the axial nozzle (7) by diameter 2 mm and length of 6 mm. The gas was injected into the vessel through the orifice (8) in the upper flange (2) tangentially to the cylinder wall (l) and created a reverse vortex flow of tornado type, so the rotating gas (9) went down to the liquid surface and moved to the central axis where flowed out through the nozzle (7) in the form of jet (10) into the quartz chamber (12). Since the area of minimal static pressure above the liquid surface during the vortex gas flow is located near the central axis, it creates the column of liquid at the gas-liquid interface in the form of the cone with the height of ~5 mm above the liquid surface (without electric discharge).

The voltage was supplied between the upper electrode (2) and the lower electrode (6) in the liquid with the help of the DC power source powered up to 10 kV. Two modes of the discharge operation were studied: the mode with "liquid" cathode (LC) and the mode with "solid" cathode (SC): "+" is on the flange (2) in the LC mode, and "-" is on the flange (2) in the SC mode. The conditions of breakdown in the discharge chamber were regulated by three parameters: by the level of the work liquid; by the gas flow rate G ; and by the value of voltage U . The ignition of discharge usually began from the appearance of the axial streamer; the time of establishment of the self-sustained mode of operation was ~1–2 s. The range of discharge currents varied within 100–400 mA. The pressure in the discharge chamber during the discharge operation was ~1.2 atm; the static pressure outside the reactor was ~1 atm. The elongated ~50 mm plasma torch (10) was formed during the discharge burning in the camera.

Diagnostics of the plasma was conducted by means of optical emission and absorption spectroscopy. A high-speed CCD-based spectrometer (14) "Plasma-spec" with a spectral resolution ~0.6 nm was used for the spectra registration in the range of wavelengths 200–1100 nm. Optical system consists of optical fibber (13), spectrometer (14) and computer (15).

The characteristic temperatures corresponding to excited states of atoms (electronic temperature T_e^*), and molecules (vibrational T_v^* and rotational T_r^* temperatures) in discharge plasma were determined by different methods. To determine vibrational T_v^* and rotational T_r^* temperatures an original technique with using the SPECAIR was used [2; 7]. A high-speed photo camera Nikon L100 for visual observation was used.

Results and Discussion. Pressure inside of system consists of static and dynamic components. Speed of air flow on periphery is less then near the center. Pressure in center of system is less then on periphery. It creates the column of liquid at the gas-liquid interface in the form of the cone (Fig. 2a). Liquid drops by diameter of 0,5–1,0 mm are break away from liquid cone tip at air flow more then 150 cm^3/s (Fig. 2b). Liquid flow rate increased with increasing of air flow. When voltage achieved U_b between fully immersed in liquid electrode and upper flange, gas gape was breakdown (Fig. 2c). Current was increased with decreasing of voltage. Breakdown voltage was 5,5 kV in the mode LC and 4,5 kV in mode SC. The time of establishment of the self-sustained mode of operation was ~1–2 s (Fig. 2d). Water electrolysis accompanies discharge burning.

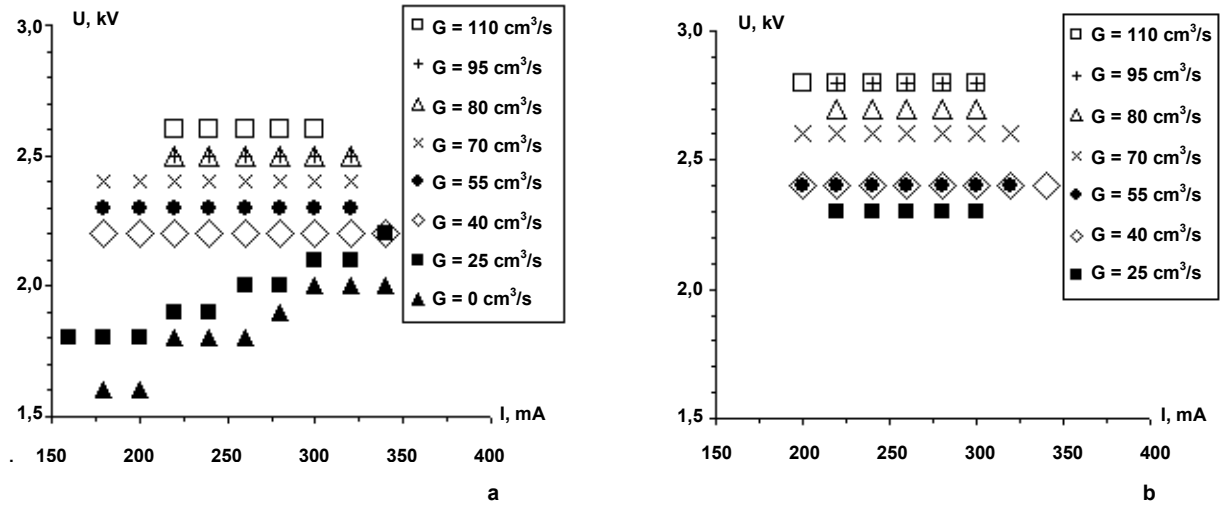

Fig. 3. Current-voltage characteristics of discharge at different air flows: "solid" cathode – a; "liquid" cathode – b

Bubbles are created on surface of T-shaped stainless steel electrode. Then they rise up to the surface, where liquid was contacted with plasma (Fig. 2e). Bubbles were not created in area where plasma contacted with liquid surface. This phenomenon needs further inquiry.

Current-voltage characteristics of the TORNADO-LE in the mode with "solid" and "liquid" cathode working in water at different airflow rates are shown in Fig. 3. The discharge in plasma-liquid system is a glowing type.

Absorption coefficients of pretreated distilled water in TORNADO-LE as a function of wavelength were measured. Gas flowed out from quartz chamber into refrigerating chamber with creating condensate. Absorption coefficients of pretreated water in main chamber and condensate in the mode LC (current 300 mA, voltage 2,8 kV, air flow 110 cm^3/s) are shown in Fig. 4a. Ratio of hydrogen peroxide concentration in condensate (outside of main chamber) to concentration in main chamber at energy input in plasma 50 kJ was 15/1. Nitrous acid HNO_2 was present only in condensate (Fig. 4a). Concentration of hydrogen peroxide inside of reactor was independent from energy input into plasma (Fig. 4b).

Typical emission spectra of plasma in TORNADO-LE inside and outside of reactor are shown in Fig. 5. All this spectra were normalized on maximum at wavelength $\lambda_n = 306{,}7$ nm. Bands hydroxyl OH and nitrogen N_2 and lines of hydrogen H_α (656.3 nm), H_β (486.1 nm), copper Cu and oxygen multiplet O (777.2 nm; 844.6 nm; 926.6 nm) are on emission spectra. Band of nitrogen $N_2(C-B)$ and lines of copper Cu were presented only outside of system.

The excitation electronic temperature T_e^* was determined by relative intensities of oxygen multiplet lines emission (777.2 nm; 844.6 nm; 926.6 nm). Excitation temperature inside of reactor was $T_e^* = 5000 \pm 500$ K and outside - $T_e^* = 4750 \pm 500$ K.

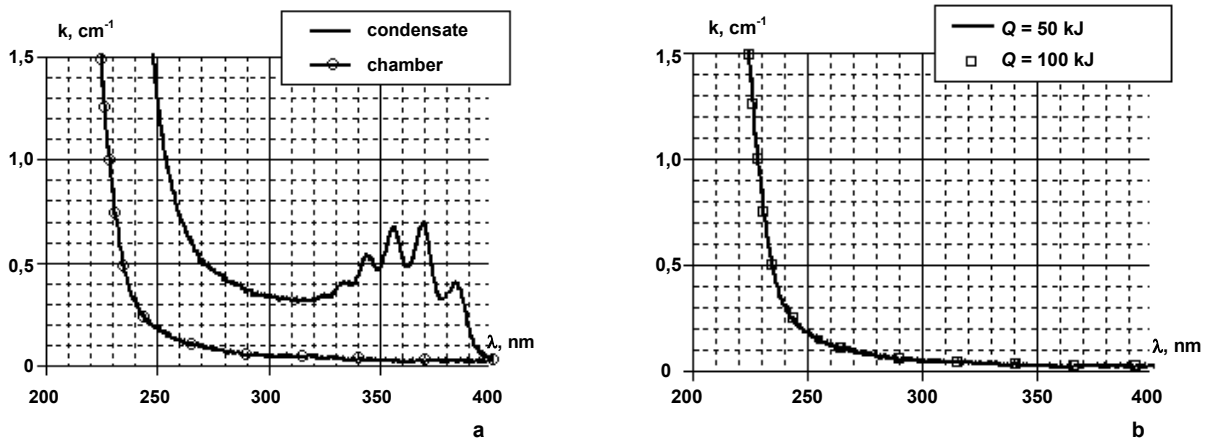

Fig. 4. Absorption coefficients of pretreated distilled water in TORNADO-LE as a function of wavelength: condensate and liquid at energy input in plasma 50 kJ – a); liquid in main chamber at different energy input in plasma 50 kJ and 100 kJ – b)

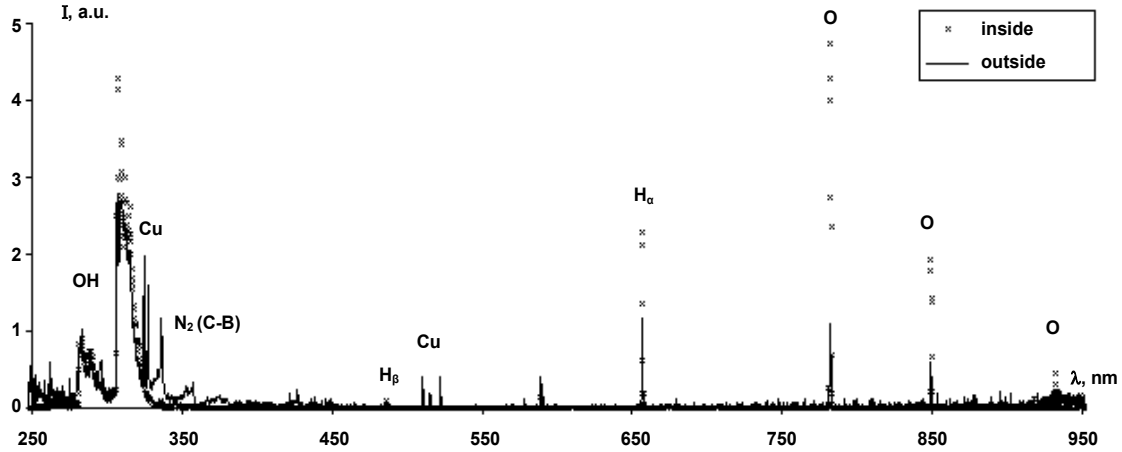

Fig. 5. Typical emission spectra of plasma in plasma-liquid system with reverse vortex flow of "tornado" type inside and outside of main chamber measured in mode "liquid" cathode (current 300 mA, voltage 2,8 kV, air flow 110 cm^3/s)

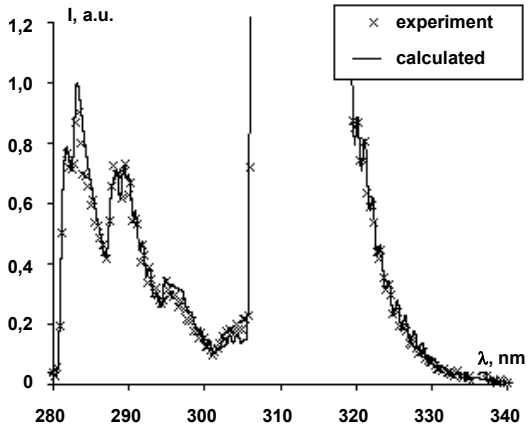

Fig. 6. Emission spectra measured in mode LC (current 300 mA, voltage 2,8 kV, air flow 110 cm^3/s) inside of main chamber and calculated by SPECAIR code at excitation temperatures $T_r^* = 4000 \pm 500$ K, $T_r^* = 4000 \pm 500$ K and $T_e^* = 5000 \pm 500$ K

Emission spectra bands of hydroxyl OH registered inside of reactor and calculated for $T_r^* = 4000 \pm 500$ K, $T_v^* = 4000 \pm 500$ K are shown in Fig. 6. They are correlated very well. Excitation temperatures $T_r^* = 3000 \pm 500$ K, $T_v^* = 4500 \pm 500$ K outside of plasma-liquid system reactor were obtained by band of hydroxyl OH.

We compare plasma parameters in TORNADO-LE with transversal arc and discharge in gas channel with liquid wall at closely inputted energy in plasma. Excitation temperatures in transversal arc were $T_r^* = 2000 \pm 500$ K, $T_v^* = 4000 \pm 500$ K, $T_e^* = 6000 \pm 500$ K [1] and in discharge in gas channel with liquid wall - $T_r^* = 3500 \pm 500$ K, $T_v^* = 4000 \pm 500$ K and $T_e^* = 6000 \pm 500$ K [2].

Conclusions.

1. Plasma is less non-equilibrium in dynamic plasma-liquid system with reverse vortex flow of "tornado" type then in transversal arc and discharge in gas channel with liquid wall.

2. Excitation temperatures were measured outside ($T_r^* = 3000 \pm 500$ K, $T_v^* = 4500 \pm 500$ K and $T_e^* = 4750 \pm 500$ K) and inside of reactor $T_r^* = 4000 \pm 500$ K, $T_v^* = 4000 \pm 500$ K and $T_e^* = 5000 \pm 500$ K).

3. Plasma is more non-equilibrium outside of reactor $T_r^* < T_v^* < T_e^*$ than inside $T_r^* = T_v^* < T_e^*$.

1. *Baddour R. F., Timmins R. S.* The application of plasmas to chemical processing // The M.I.T. PRESS. – 1967. 2. Internet source: http://www.specair-radiation.net. 3. *Kalra C. S., Kossitsyn M., Gutsol A.* Electrical discharges in the Reverse Vortex Flow – Tornado Discharges // El. Proc. Of 16th Int. Symp. on Plasma Chem., Taormina. – 2003. 4. *Koroteev A. S., Mironov V. M., Svirchyk Yu.S.* Plasmatrons: constructions, characteristics, calculation: M, – 1993. (in Russian). 5. *Prisyazhnevich I. V., Chernyak V. Ya., Naumov V. V. et al.* // Ukr. J. Phys. – 2007, V.52, N. 11. 6. *Prisyazhnevich I. V.,.Chernyak V. Ya, Scalný J. D. et al.* Sources of Non-equilibrium Plasma at atmospheric Pressure // Ukr. J. Phys. – 2008, V. 53, N. 5. 7. *Prysiazhnevych I., Lomonos L., Chernyak V.* Tecniquesof determining vibrational and rotational excitation temperatures by OH (A-X) AND N_2 (C-B) bands for plasma diagnostics // Proc. IV Int. Conf. El. and App. Ph., Kyiv, 2009. 8. The 63rd Gaseous Electronics Conference and 7th International Conference on Reactive Plasmas, October 4–8, – 2010, Paris, France.

Submitted 17.11.10

UDC 519.9

V. Obukhovsky, Dr. Sci.,
O. Ilchehko, stud.,
V. Lemeshko, Ph.D.,
V. Nikonova, post. grad. stud.,
O. Balashov, stud.

INVESTIGATION OF INTERMOLECULAR INTERACTION IN AQUEOUS SOLUTION OF ETHANOL USING RAMAN SCATTERING

Досліджено спектри комбінаційного розсіювання світла розчину етилового спирту у воді при різних концентраціях компонент. Враховується, що в результаті міжмолекулярної взаємодії утворюються складні комплекси. Показано, що взаємодія молекул етилового спирту з молекулами води відбувається за рахунок О…О – Н взаємодії (водневий зв'язок). Порівняльним аналізом спектрів показано, що аномально широка смуга валентних ОН-коливань як молекул H_2O, C_2H_5OH, так і їх суміші обумовлена впливом саме кластерних утворень.

Ключові слова: комбінаційне розсіювання світла, концентрація етилового спирту, валентне ОН-коливання води, водневий зв'язок, кластер.

Raman scattering spectra of aqueous solution of ethanol at different concentrations of components have been investigated. Forming of the complex aggregates as a result of intermolecular interaction must taken into consideration. Interaction of ethanol molecules with water molecules has been shown to occur due to O ... O – H interaction (hydrogen bond). The anomalously wide band of valence OH-vibrations of both H_2O, C_2H_5OH molecules and their mixtures has been shown by comparative analysis of the spectra to be caused by the cluster structures.

Key words: Raman scattering, ethanol concentration, valence OH-vibrations of water, hydrogen bond, cluster.

Introduction. The existing models of water structure are based on existence of tetrahedral coordination of the molecules in liquid water and consequently on presence of spatial three-dimensional grating of hydrogen bonds. The last can be either spatially homogeneous (continuous or continuum model) or heterogeneous (mixed or discrete model) [9]. Existence of H_2O monomolecules in liquid water (water molecules not linked by H – bond) is an essential feature of the last model, whereas the monomolecules are absent in the first model.

Recently, the processes determining the structure of partially ordered liquids such as alcohols [21, 23, 24, 11, 31] are interesting. As a rule, the molecular structure of associates is studied using oscillation spectroscopy [23].

Recent experimental and theoretical methods open a new stage of research in this field. Femtosecond spectroscopy techniques provide information about the time of both rupture and recovery of hydrogen bond [21, 24, 25, 29]. Cluster isolation methods in Ar and He nanodrops gave an opportunity to study clusters of different sizes separately [11, 30]. On the other hand, modern computer programs let us to carry out quantum-chemical calculations and to obtain data of the structure and spectral properties of molecular systems.

The parameters of hydrogen bond in alcohol are close to similar parameters in water. But the alcohol molecules have carbon atoms that do not participate in the formation of H-bond. It allows studying the processes in the medium not only by the oscillatory band of hydroxyl (O-H) but by Raman scattering spectra of vibrations of C-O, C-H bonds. The alcohols are known to form H-bonds of medium power (5–15 kcal / mol) [28].

Despite the fact that a lot of investigations [18, 19, 26, 28, 31] are devoted to the study of properties of water-ethanol solutions, the problems of the structural features of these solutions have been still far from resolving.

This article is devoted to investigation of Raman scattering spectra of water-ethanol mixtures at different concentrations of components. Studying hydrogen bonds in aqueous solutions at different concentrations of ethanol, proving the availability of cluster formations by comparative analysis of Raman scattering spectra of H_2O, C_2H_5OH and their mixtures were the main aims of the investigation.

Experiment. The modernized and automated spectral-computing system based on double monochromator DFS–52 (Fig. 1) has been used.

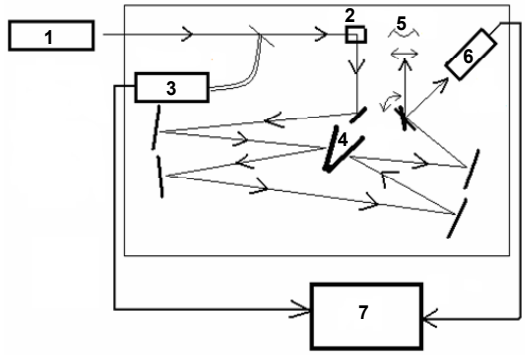

Fig. 1. A scheme of spectral-computing complex based on double monochromator DFS-52. 1 – helium-cadmium laser, 2 – ditch, 3 – comparison channel photomultiplier, 4 – diffraction grating, 5 – eyepiece, 6 – registration channel photomultiplier, 7 – computer

The comparison channel was added to registration scheme (the change of laser radiation intensity was taken into account). Both channels transmit data to the computer through an analog-digital converter. The software building Raman scattering spectrum on these data has been designed. Panoramic spectra within the range 200 ... 4000 cm^{-1} with a spectral resolution of 2 cm^{-1} were recorded when registering a consistent signal. Accumulation time of the spectrum amounted to a range of 40 minutes.

Helium-cadmium laser (wavelength 441 nm, power 5–10 mW) was used as a source exciting the Raman scattering. Heating the sample during the measurement of Raman scattering spectra did not practically occur, due to small value of absorption coefficient under excitation frequency.

Scattered light is observed at 90° relatively to the direction of incident laser beam. The spectra were recorded with the width of input and output gaps, which did not exceed 200 μ. The temperature of liquid samples was within the range 293 ÷ 295 ° C. As it was noted in [8, 32], the average shift factor of OH-vibration band is – 2,1 ± 0,9 cm^{-1}/K. Accordingly, the specified difference in temperature was within the error of monochromator measurement.

Results and Discussion. A part of the spectrum of Raman scattering within the range 2800–3800 cm-1 for a mixture of ethanol and water at different concentrations of mixture components is shown in Figure 2.

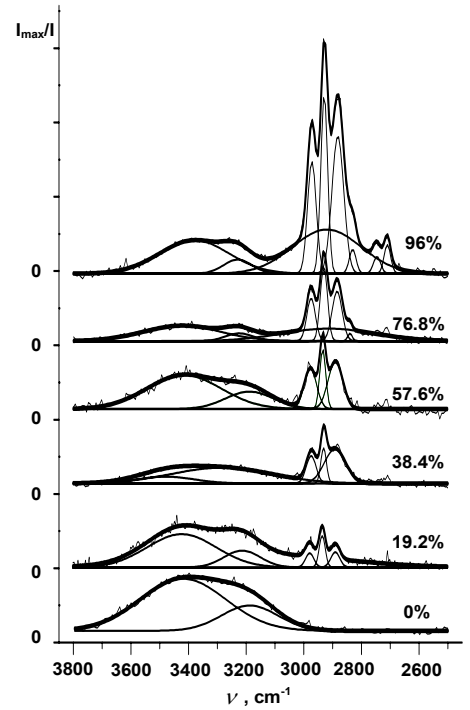

Fig. 2. Raman scattering spectra for water-ethanol mixture at different concentrations of ethanol

Using techniques of complex contour separation for Gaussian components, five types of oscillations were defined in this frequency band (Fig. 3):

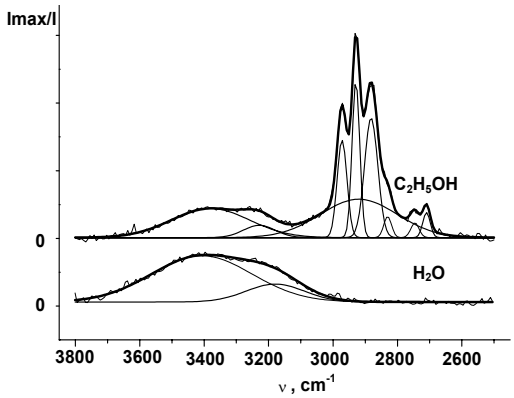

Fig. 3. Raman scattering spectra of ethanol and water

valence symmetric vibrations of group CH_2- (~ 2877 sm^{-1}), valence symmetric vibrations of group CH_3 (~ 2928 sm^{-1}), valence asymmetric vibrations of group CH_3 (~ 2974 sm^{-1}), valence vibrations of group OH (3000 ~ 3800 sm^{-1}) [5, 22, 33]. Just that very frequency range was chosen among all the bands of molecular vibrations, on the assumption of the following considerations. First, the characteristic lines of vibrations of both mixture components that have the highest intensity relative to other vibration classes throughout the molecular spectrum are there in this part of the spectrum. Secondly, the characteristic vibrations of CH-bonds of ethanol have sufficient intensity for analyzing of their parameters even at low concentrations C2H5OH in the mixture just in this frequency range. Thirdly, all other classes of oscillations hardly change their position when changing the concentration [3].

Two types of oscillations are highlighted in Fig. 3 within the frequency range 3000 ~ 3800 sm-1. These two oscillations are often considered as one unusually broad OH-valence vibration when analyzing Raman scattering spectra of water [1, 7, 8]. Fig. 3 shows that these oscillations are present both in water molecule and ethanol molecule.

Let us consider the options of anomalous broadening of OH-vibration bands (with maxima at frequencies ν_1~ 3200 sm^{-1}, ν_2 ~ 3400 sm^{-1}). It is known that the symmetry group of molecules H2O is C_{2v}, O-H bond length is 0,9572 Å (a free molecule in gas phase) and the angle between the bonds is 104, 52° [20]. All three vibrational modes, i.e. valence symmetric (A1), deformation symmetric (A1) and valence antisymmetric (B1), are active both in Raman and in IR scattering. The frequencies of internal vibrations of free H_2O molecule are well known: 3656.65 cm^{-1} ($\nu_{sym.val.OH}$), 1594,59 cm^{-1} ($\nu_{def.OH}$) and 3755.79 cm^{-1} ($\nu_{asym.val.OH}$) [12].

Such parts of vibrational spectrum are distinguished in Raman scattering spectrum of liquid water [10, 17]:

50 ~ 200 cm-1 - intermolecular translational vibration bands with the maxima at frequencies about 60 and 190 cm-1;

300 ~ 900 cm-1 - intermolecular libration band with a maximum about 700 cm-^{1};

1600 ~ 1700 cm^{-1} - deformation band with a maximum of ~ 1650 cm^{-1};

2000 ~ 2400 cm-^{1} - weak associative band with a maximum of ~ 2200 cm^{-1};

3000 ~ 3800 cm-1 - band of valence vibrations of OH groups with a maximum of ~ 3400 cm^{-1}.

The largest change of both frequency and half-width of the bands mentioned above are observed in the valence band of OH-vibrations at various concentrations of ethanol in the mixture. However, the vibration lines of C-C-O, C-C, C-O and C-H groups of ethanol practically do not change the corresponding characteristics [6] when changing the concentration of solution. Therefore, it is advisable to pay attention just to the band of valence vibrations of OH group with a maximum ~ 3400 cm^{-1}.

Valence oscillations of H_2O molecule in liquid phase are displaced by 400 cm^{-1} to low frequency region as the experimental data show [4] (Fig. 3). This shift can be explained by influence of hydrogen and Van der Waals interactions formed between individual molecules. The chemical bond energy is known to be ~ 500 kJ/mol, the hydrogen bond energy is ~ 100 kJ/mol, the Van der Waals bond energy is ~ 1 kJ / mol [20]. The Van-der-Waals interaction energy to the chemical bond energy ratio is $\Delta\nu_1 \sim 5 * 10^{-3}\nu$, and hydrogen bond interaction to chemical bond ratio is $\Delta\nu_2 \sim 5 * 10^{-2}\nu$. For the frequency of symmetric valence vibration of free H_2O molecule ($\nu_{sym.val.OH}$ = 3656.7 cm^{-1}), the total frequency shift $\Delta\nu_{total.sym.OH}(\Delta\nu_1 + \Delta\nu_2)$ should be:

$$\Delta\nu_{total.sym.val.OH} = \left(\frac{\Delta\nu_1}{\nu} + \frac{\Delta\nu_2}{\nu}\right) * \nu_{sym.val.OH} \approx 201 cm^{-1}$$

This shift corresponds to the peak value with greater intensity (ν ~ 3400 cm^{-1}) within the range 3000–3800 cm^{-1} (Fig. 3). Hence it follows that i`t is this oscillation (ν ~ 3400 cm^{-1}) of H_2O molecules in the liquid phase that corresponds to valence vibrations of H_2O molecule in the gas phase ($\nu_{sym.val\ OH}$ = 3656.7 cm^{-1}), but shifted to ~ 200 cm^{-1} towards lower frequencies due to the influence of both Van der Waals and hydrogen interaction.

The position of antisymmetric valence OH-vibration ($\nu_{asym.val.OH}$ = 3755.8 cm^{-1}) of free H_2O molecule in liquid water should be calculated as well:

$$\Delta\nu_{total.asym.val.OH} = \left(\frac{\Delta\nu_1}{\nu} + \frac{\Delta\nu_2}{\nu}\right) * \nu_{asym.val.OH} \approx 207 cm^{-1}$$

Accordingly, in the Raman scattering spectrum of liquid water, antisymmetric valence OH-vibration should appear in the region ~ 3550 cm^{-1}. Indeed, a weak peak can be observed within the frequency range 3540 ~ 3600 cm^{-1} (Fig. 3). According to the above considerations, let us interpret it as antisymmetric OH-valence vibrations of liquid water.

The position of the third peak in abnormally broad band of OH-vibration of water takes a value ~ 3200 cm^{-1}. It can be interpreted as an overtone of the deformational OH-vibration of water (1630 cm^{-1}·2 = 3260 cm^{-1}). Moreover in [13], the authors argue that abnormally wide zone of water oscillations in the region 3000 ~ 3800 cm^{-1} can be explained by resonance interaction of deformation vibration overtone Δ_0 and symmetric valence vibrations Δ. The process of Fermi resonance interaction can be expressed by the relation:

$$\Delta^2 = \Delta_0^2 + 4W^2,$$

where W is Fermi resonance constant.

As evidence of Fermi resonance existence, a number of experiments for research of both intensity and shape of OH-vibration band (3000 ~ 3800 cm-1) of liquid water at different concentrations of alkali and two-valence metals have been carried out in [2, 14, 15]. A general trend was observed that with increasing in concentrations of appropriate compounds in the water, OH-vibration band converged while moving in the high frequency region. That was explained by weakening of hydrogen bonds with increasing in concentration of impurity compounds, and, consequently, decrease of Fermi resonance interaction.

Investigation of change of both intensity of deformation OH-vibrations of water (~ 1640 cm^{-1}) and shape of valence OH-band (3000 ~ 3800 cm^{-1}) at different concentrations of H_2O in D_2O is considered to be another proof of Fermi resonance existence., The valence band of OH groups has symmetrical domelike shape under low concentrations of H_2O. Deformation band of Raman scattering spectrum of H_2O molecules misses, there is no Fermi resonance. Deformation band of H_2O molecules appears under the concentration of 30 molar % of H_2O in D_2O, at the same time the valence band of OH groups takes asymmetrical shape [16]. Comparing the Raman scattering spectra of the valence OH-vibrations of liquid water and ethanol, we can note that there are two expressed peaks in each of the substances in the region ~ 3200 cm^{-1}, and in the region ~ 3400 cm^{-1}. When explaining the asymmetric shape of valence OH-vibration band of water by existence of Fermi resonance between deformation OH-vibration overtone (~ 3200 cm-1) and valence OH-vibration (~ 3400 cm^{-1}) of water, the problem to explain a similar asymmetric shape of OH-vibration band in ethanol arises. The fact is that deformation OH-vibration band in the Raman scattering spectrum of C_2H_5OH misses. Accordingly, overtones of these vibrations may not exist in ethanol. Just presence of clusters formed by hydrogen bonds can explain that there are two peaks in abnormally broad OH-vibration band in both compounds. As it was mentioned above, influence of hydrogen and Van-der-Waals bonds determines the frequency shift of symmetric valence OH-vibrations of water in the gas phase (3657 cm^{-1}) by ~ 200 cm^{-1} to low frequency region (~ 3400 cm^{-1}). When forming of the cluster, which consists of a number of molecules of water and ethanol, hydrogen interaction between molecules increases as the cluster is energetically favorable stable structure during a certain period of time.

Provided the clusters exist in solution (discrete model) we can explain the anomalous broadening of OH-vibration band and the presence of two peaks. According to these considerations, the peak in the region ~ 3200 cm^{-1} can be interpreted as the valence OH-vibration band shifted from the value of ~ 3400 cm^{-1} to the value of ~ 3200 cm^{-1} just due to cluster forming both in the associates of H_2O (or C_2H_5OH) and in complexes $[C_2H_5OH]^n$ $[H_2O]^m$.

1. *Бункин, О. А.* Вынужденное комбинационное рассеяние назад на водяном аэрозоле в атмосфере / О. А. Бункин, У.Х. Копвиллем, В. М. Чудновский // Оптика и спектроскопия. – 1985. – Т. 59. – №2. – С. 306–310. 2. *С. А. Буриков, Т. А. Доленко, В. В. Фадеев.* Идентификация неорганических солей и определение их концентраций в многокомпонентных водных растворах по валентной полосе КР воды с помощью искусственных нейронных сетей. Нейрокомпьютеры: разработка, применение, 2007, № 5, с. 62–72. 3. *Буриков С. А., Доленко Т. А., Пацаева С. В., Южаков В. И.* Диагностика водно-этанольных растворов методом спектроскопии комбинационного рассеяния света. М., "Оптика и спектроскопия" – 2009 – № 11 – 1082–1088 с. 4. *Бэкингем Э.* Основы теории межмолекулярных сил. Применение к малым молекулам. // Межмолеку-лярные взаимодействия: от двухатомных молекул до биополимеров. Т. 2. / Ред. Б. Пюльман. – М.: Мир, 1981. – С. 70. 5. *Казыцина Л. А., Куплетская Н. Б.* Применение УФ-, ИК- и ЯМР-спектроскопии в органической химии. Учеб. Пособие для вузов. М.: Высш. Школа, 1971. 264 с. 6. *Колесов Б.А.* Спектры КР одиночных H2O, изолированных в полостях кристаллов // Журнал структурной химии. – 2006 – Т. 47, № 1. – С. 27 – 40. 7. *Наберухин, Ю. И.* Что такое структура жидкости? / Ю. И. Наберухин // Журнал структурной химии. – 1981. – Т. 22. – № 6. – С. 62–80. 8. *Першин, С. М.* Наблюдение льдоподобного состояния в переохлажденной воде и его разрушение импульсами лазера / С. М. Першин // Оптика и спектроскопия. – 2003. – Т. 95. – № 4. – С. 628–636. 9. *Сущинский, М. М.* Спектры комбинационного рассеяния молекул и кристаллов / М. М. Сущинский. – М.: Наука, 1969. 10. *Эйзенберг Д., Кауцман В.* Структура и свойства воды. Л.: Гидрометеоиздат, 1975. 280 с. 11. *Buck U., Huisken F.* Infrared spectroscopy of size-selected water and methanol clusters // Chem.Rev. – 2002. – Vol.100, N 11. – P. 3863–3890. 12. *Buckingham A. D.* / J. Mol. Struct. – 1991. – 250. – P. 111 – 118. 13. *S. A. Burikov, T. A. Dolenko, V. V. Fadeev*. The Role of Fermi Resonance information of valence band of water Raman scattering. Research Letters in Optics, Vol. 2008 (2008), ID 204828, 4 pages, doi: 10.1155/2008/204828. 14. *S. A. Burikov, T. A. Dolenko, V. V. Fadeev*. Identification of inorganic salts and determination of their concentrations in water solutions from the Raman valence band using artificial neural networks. Pattern Recognition and Image Analysis, 2007, Vol. 17, N 4, pp. 554–559. 15. *S. A. Burikov, T. A. Dolenko, V. V. Fadeev, and I. I. Vlasov*. Revelation of Ions Hydration in Raman Scattering Spectral Bands of Water. Laser Physics, 2007, Vol. 17, N 9, pp. 1–7. 16. *S. A. Burikov, T. A. Dolenko, P. A. Velikotny, A. V.* Sugonyaev, and V. V. Fadeev. The Effect of Hydration of Ions of Inorganic Salts on the Shape of the Raman Stretching Band of Water. Optics and spectroscopy, 2005, Vol. 98, № 2, pp. 235–239. 17. *Chaplin M.* Water Structure and Bihavior // www.lsbu.as.uk/water. 18. *Cleveland D., Carlson M., Hudspeth E. D.*, et al. Raman Spectroscopy for the Undergraduate Teching Laboratory: Quantification of Ethanol Concentration in Consumer Alcoholic Beverages and Qualitative Identification of Marine Diesels Using a Miniature Raman Spectrometer // Spectrosc. Lett. 2007. Vol. 40. Iss 6. P. 903–924. 19. *Egashira K., Nishi N.* Low-Frequency Raman Spectroscopy of Ethanol-Water Binary Solution: Evidence for Self-Association of Solute and Solvent Molecules // J. Phys.-Chem. B. 1998. Vol. 102. № 21. P. 4054–4057. 20. *Eisenberg D., Kauzmann W.* The structure and properties of water. – Oxford University Press, 1969. 21. *Gaffney K., Davis P., Piletic I.* et al. // Hydrogen bond dissociation and reformation in methanol oligomers following hydroxyl stretch relaxation // J.Phys.Chem. A. – 2002. – Vol.106, N 50. – P. 12012–12023. 22. *Gnyba M., Jędrzejewska-Szczerska M., Kerdnen M., Suhonen J.* Sol-gel materials investigations by means of Raman spectroscopy // Proc XVII IMEKO World-Congress, June 22–27,2003. Dubrovnik. Croatia. P. 237–240. 23. *Handgraaf J.-W.,* van Erp T.S., Meijer E.J. Ab initio molecular dynamics study of liquid methanol // Chem.Phys.Lett. 367 (2003) P. 617. 24. *Laenen R., Gale G. M., Lascoux N.* IR spectroscopy of hydrogen-bonded methanol: vibrational and structural relaxation on the femtosecond time scale. // J.Phys.Chem. A. – 1999. – Vol. 103, N 50. – P. 10708–10712. 25. *Mukamel S., Zhuang W.* Coherent femtosecond multidimentional probes of molecular vibrations // PNAS. – 2005. – Vol. 102, N 39.– P. 13717–13718. 26. *Nose A., Hojo M.* Hydrogen bonding of water-ethanol in alcoholic beverages // J. of Bioscience and Bioengineering. – 2006. Vol. 102. N 4. P. 269–280. 27. *Nose A., Hojo M., Ueda T.* Effects of Salts. Acids, and Phenols on the Hydrogen-Bonding Structure of Water-Ethanol Mixtures // J.Phys. Chem. B. – 2004. Vol. 108. P. 798–804. 28. *Pimentel J., McClellan O.* The Hydrogen bond / Freeman, San Francisco & London., 1960. 29. *Tanimura I. I., Mukamel S.* Two-dimensional femtosecond vibrational spectroscopy of liquids // J. Chem. Phys. – 1993. – Vol.99. – P. 9496–9511. 30. *Toennies J.P., Vilesov A. F.* Superfluid helium droplets: a uniquely cold nanomatrix for molecules and molecular complexes // Angew. Chem. Int. Ed. – 2004. – Vol. 43. – P. 2622–2648. 31. *Sanford C. L., Mantooth B. A., Jones B. T.* Determination of Ethanol in Alcohol Samples Using a Modular Raman Spectrometer // J. Chem. Educ. 2001. Vol. 78. P. 1221–1225. 32. *Scherer, J.* Raman spectra and structure of water from -10 to 90° / J. Scherer, K. Go, S.Kint // Physical chemistry. – 1974. – Vol. 78. – № 13.– P. 1304–1313. 33. *Yu Y., Lin K.,Zhou X., Wang H., Liu S., Ma X.* New C–H stretching vibrational spectral features in the Raman spectra of gaseous and liquid ethanol // J. Phys. Chem. 2007 Vol. 111. N 25. P. 8971–8977.

Submitted 27.05.10

UDC 621.315.59

S. Pavlyuk Ph.D.,
O. Oberemok Ph.D.,
I. Tishchenko stud.

CURRENT PINCHING IN FORWARD-BIASED UNIPOLAR MICROTRANSISTORS

У роботі досліджено протікання імпульсу струму з густиною до 10^4 А/см^2 крізь прямозміщений p-n перехід КНІ польового транзистора. Отримані осцилограми дозволили побудувати вольт-амперну характеристику, з S-подібною областю. Показано, що ця область пов'язана з утворенням шнура струму. Візуальні спостереження підтвердили появу одного повного шнура та декілька його зародків.

Ключові слова: Шнурування струму, прямозміщений p-n перехід, КНІ транзистори.

In this work the flowing of current pulse with density 10^4 A/sm^2 through forward-biased p-n junction of FET transistors is studied. Oscillograms been obtained allowed to build Volt-ampere description with S-similar region. It is shown that this region is caused by the formation of current pinch. Visual observation has confirmed the appearance of a one full pinch and several its nucleuses.

Introduction. During microminiaturization of semiconductor devices and large integral chips which used micro and nanotechnique arise the problem that associated with growing of flowed current density by the preserving it absolute value. Decreasing of parts size of microchips brings to significant arising of density of flowed current up to $10^5 \cdot A/sm^2$. This encourages an appearing of new effects in semiconductors that limit it operating range. Studying of given kinds of effects is urgent and is interesting as for developer of modern semiconductor devices as for physicists.

In recent years a flowing of current with large density ($\geq 10^5$ A/sm^2) in structures "silicon on insulator" (SOI) was investigated. Used structures were differed as the relation $d_{si} < l_{si}$ between thicknesses of the working layer of silicon d_{Si} and depletion layer in it L_{Si} was satisfied. Thus due to the relation $d_{si} < l_{si}$ and the presence in SOI structures so-called "back gate" a resistance of working silicon layer under the current flowing, became significantly inhomogeneous. Under these conditions in the structures the various effects were observed: voltage and current fluctuations [3], its regular stratification [4], emission of light [5] and an appearing of termodiffusion solitons [6].

As it had been shown in [5] when FET transistor was powered by generator of current then in electric circuit a fluctuations of voltage and current had been appeared.

It was found that on the beginning of S-similar region of VAC the voltage fluctuations had a relaxing nature. With increasing power, they gradually changed their form from relaxation to quasi-sinusoidal and again - to relaxation, but with another fluctuation ratio [5]. Similar changes of fluctuations' shape also were observed when at control gate of FET transistor a potential of different sign was applied [6].

Parameters of such kind processes and the physical model that explains the effects observed are in [3–6].

Experiments showed that current and voltage fluctuations occur in the unipolar FET transistors and silicon diffusion resistors only in n^+-n-n^+ structures [6]. In the structures with the hole conductivity no any oscillations occurred. Studies of singularities of transient processes during current pulse flowing in p^+-p-p^+ FET unipolar transistors gave an explanation for absence of current and voltage fluctuations in these structures [7].

Effects observed in structures where realized relation $d_{si} < l_{si}$ For that purpose silicon diffusion resistors (SDT), made of technology "silicon with dielectric isolation", (SWDI) were studied.

With the current increasing the voltage on silicon diffusion resistors (SDR) increases as step-wise. At the same time in SDR occurs a strip that glows. It is located perpendicular to the direction of current flow. Further increasing of current results to the occurring between the contacts a longitudinal pinch instead of stripe, which also glows, and finally causes to drastically damaging of structures, due to its overheating [9].

These effects can be explained by formation of THD high-field domain in silicon [10], "warming up" in this field of electrons and holes and their subsequent radiation recombination.

All above mentioned effects were observed in control gate with the backward biasing relative to *p-n* junction.

A studying of extreme current flow in the forward direction relative to the *p-n* junction was not carried out. But such influence of this current may be essential. This is confirmed by the fact that with the passage of extreme currents in the forward direction through the crystal semiconductor diode in the forbidden zone an additional recombination centers appeared, which significantly influenced on the parameters of diodes.

It is known that the existence of deep recombination centers and their concentration significantly determine the lifetime of minority charge carriers in semiconductors. Of course, these centers introduced to the semiconductor due it's affecting by ionization radiation [4] or due it's doping by corresponding impurities (an example, silicon – gold) [3]. As a result in semiconductor appear structural defects that lead to appearance in the forbidden zone of system of electrically active centers, including deep.

In [12] has been suggested that the different structural defects and related electrically active centers in the forbidden zone of the semiconductor may occur and fix in it under inhomogeneous heating of the crystal. It had been studied a change of effective lifetime of minority charge carriers $\tau^*\rho$ in the base of power silicon p+-n diode type of CD-209 under short time inhomogeneous heating due to the direct current pulse of regular amplitude and duration. At that time a current density in a crystal reaches 10^4 A/sm^2, specific power that applied to the diode, reached 10^6 W/sm^3. In the investigated diodes the $\tau^*\rho$ value decreased down to 10 times.

The aim of given work is studying of flowing of pulse of current with extreme density under forward biasing of *p-n* junction of FET transistor.

The experimental results. Transistor's design. Fig. 1 presents a schematic of the investigated FET transistors (control gate isn't shown). Their length of silicon film n-type was for 2, 3, 10, 45 μ, the width w of the film was 100 μ, and thickness d – 0.4 μ. Thicknesses of included oxide, silicon substrate, polisilicon control gate and under-gate oxide was 1, 400, 1 and 0.1 μ correspondingly.

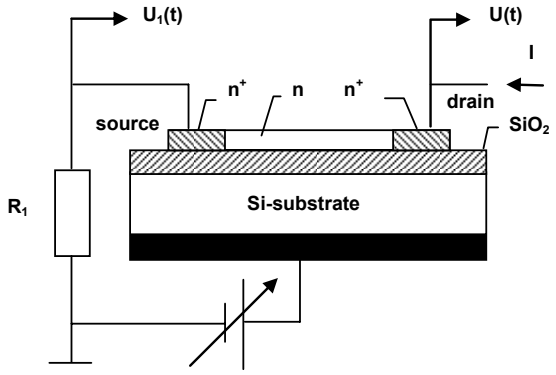

Fig. 1. Scheme of FET transistor

Part of transistors used had no control gate. Their phosphorsilica glass layer thickness of 1 mkm protected the top surface of the silicon film. During measurements the control gate was left at floating potential, and substrates was linked to leak, however a bias voltage V could applied to them.

Silicon films of some transistors had two lateral probes for measurement its Hall voltage. The concentration of electrons and their mobility in these films were 5.10^{14} sm^{-3} and 1400 $sm^2/(Vs)$, respectively.

Research technique. Using a special generator a single rectangular pulse of current passed through FET transistor in forward relative to p-n junction direction. Duration of pulse was between 10 μs and 1 s. During studding of kinetics of changing of voltage falling at the beginning of current pulse it duration varied from 20 μs to 200 μs .

For maximum and minimum values of voltage the volt-ampere descriptions were plotted for different time moments.

Simultaneously with the passage of current pulse by a microscope it could be seen FET transistor. In this case the duration of pulse current was defined in such way that it was possible to fix the glow of this cord. This duration was 10 ms – 100 ms.

Oscillograms of voltage falling on FET transistor

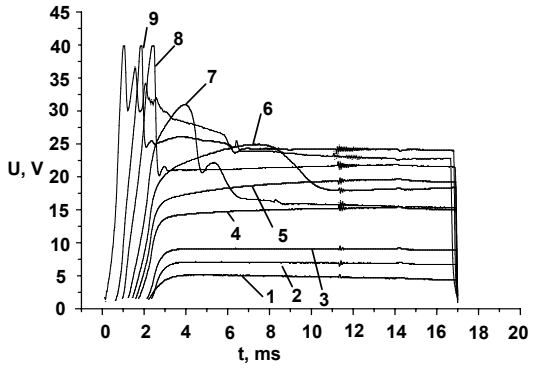

Fig. 2. Oscillograms of voltage falling on FET transistor

Fig. 2 shows the oscillograms of voltage falling on FET transistor.

As it seen from oscillograms when currents are low the voltage falling replicated rectangular shape of current pulse (oscill.1–3). Rising of magnitude of current pulse adduced to rising of voltage falling at the end of pulse (oscill.4,5), further formation of voltage peak, shifting of the peak to the pulse beginning (oscill.6–10). On oscillograms 8–10 an appearing of additional transient processes is observed. Between current peak and its stationary value the additional voltage minima are appeared. After forming of voltage peak the value of its falling at the end of pulse is stabilized and turned as unchanged in time. In some of structures with growing of magnitude of current pulse the stabilization of current falling value was observed too.

Volt-ampere descriptions. Volt-ampere descriptions are shown on the figure 3. As it seen from figure the Volt-ampere description has a few regions. Until the peak of voltage is not observed the VAD has a standard form (interval A on curve 1 and 2). After the peak of voltage had appeared on the VAD the S-similar region (interval B on curve 1) is appeared. Further it transformed in region with increased value of voltage (interval B on curve 1) and then to the second S-similar region (interval C on curve 1).

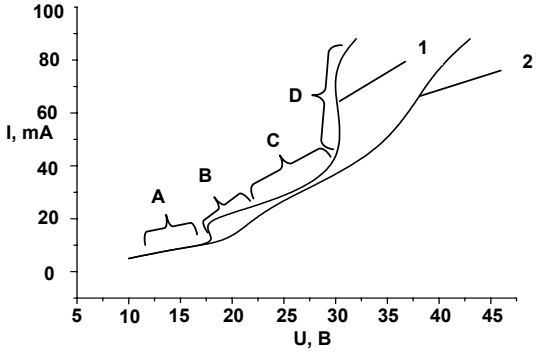

Fig. 3. Volt-ampere descriptions of FET transistor

Volt-ampere description is shown as curve 2 has bolted for maxima values of voltage falling, i.e. for voltage peak. On it there is no any S-similar regions observed (fig. 3).

Results discussions. From [8] it is known that in system with S-similar description the current pinching has to be appeared. This pinch begins to shunt a part of base area that causing to voltage falling on it. An increasing of current within some range does not change the value of voltage falling. It may be explained as the pinch diameter is increased when the current is increased.

The second jump of voltage is related to appearance of the second pinch of current, that is located on certain distance from the first. In accordance with [8], in such systems there must to be stratification of current on pinches. It is possible to assume that in a wide and short specimen may to appear a much more pinches.

As indirect proving of rightness of above explanation can be a fact, that in a microscope was observed one pinch, that passes from the one contact to the other one and, depending on the size of current, a few embryos of other pinches, as areas which glow, near the positive contact of p-n junction.

Conclusions. 1. The S-similar region was fond on VAD of FET transistor.

2. After appearing of S-similar region the one pinch and a few embryos of other pinches were observed.

1. *Bakanowski A. E., Forster J. H.* // Electrical Properties of Goal-Doped Diffused Silicon Computer Diodes. Bell Syst. Techn. Journ., 43, – 1972. 2. *Вавилов В. С.* Действие излучений на полупроводники, Физматгиз, – М.,– 1963. 3. *Dobrovolsky V. N., Ninidze G. K., Balucani M., Ferrari A., Lamedica G.* High-Amplitude High-Frequency Oscillations of Temperature, Electron-Hole Pair Concentration and Current in the Silicon-on-Insulator Structures. // Journal of Applied Physics, – 2000. – V. 88, № 11. 4. *Dobrovolsky V. N., Ninidze G. K., Balucani M., Ferrari A,* High-Amplitude and High-Frequency Oscillations of Temperature and Current in SOI Structure // Microelectronic Engineering, – 1999, V. 72, № 1–4. 5. *Dobrovolsky V. N., Ninidze G. K., Ishchuk I. V., Pavljuk S. P., Plichko Y. O.* Self-organization in SOI FET "Microelectronic Engineering", V. 72, № 1–4. – 2004. Добровольський В. Н., Нінідзе Г. К. Випромінювання світла термічно генерованою електронно-дірковою плазмою в польовому КНІ-транзисторі. УФЖ, 2002, Т. 47, № 5. 6. *Добровольский В. Н., Павлюк С. П.* Термический градиентно-дрейфовый домен в электронно-дырочной плазме полупроводников ФТП. – 1981, – Т. 15, № 1. 7. *Зи С.* Физика полупроводниковых приборов.М, "Мир", – 1984. 8. *Нінідзе Г. К., Павлюк С. П., Ищук Л. В., Кушниренко В. В.* Использование КНИ-транзистора в качестве генератора колебаний напряжения. "Технология и конструирование радиоэлектронной аппататуры",№ 3 (57), – 2005. 9. *Кушниренко В. В., Нинидзе Г. К., Павлюк С. П., Коноваленко Л. Д.* Исследование кремниевых диффузионных резисторов при протекании импульса тока большой плотности. // ТКЕА, № 5 (59), 2005. 10. *Кушниренко В. В., Павлюк С. П.* Особливості перехідних процесів у р +- р – р + польових транзисторів, виготовлених за технологією "кремній на ізоляторі" Вісник КНУ. Радіофізика та електроніка", вип. 10. 2007. 11. *Павлюк С. П., Кушниренко В. В., Нинидзе Г. К., Савицкий С. М., Третяк О. В.* Воздействие импульсов прямого тока на время жизни неосновных носителей заряда в р + - п диоде. "Технология и конструирование радиоэлектронной аппататуры", № 1 (67), 2007.

Submitted 20.10.10

UDC 537.6/.8

O. Prokopenko, Ph.D.

MICROWAVE SOURCES BASED ON SPIN-TORQUE NANO-OSCILLATORS

Розглянуто можливість застосування магнітних наноконтактів (МНК) для створення мікрохвильових генераторів сигналів для телекомунікаційних систем. Якісно розраховано потужність мікрохвильового сигналу, що віддає МНК у вільний простір (у дальній та ближній зонах), у мікрохвильові лінії передачі та резонатори. Показано, що ця потужність є малою порівняно з потужністю мікрохвильового сигналу, яка може бути виміряна за допомогою магніторезистивного ефекту. Однак, безпосереднє вимірювання потужності мікрохвильового сигналу, який генерується МНК, може бути зручним у випадку масиву з багатьох контактів. Зроблено пропозиції щодо практичного застосування МНК у телекомунікаційних системах з урахуванням отриманих у статті результатів та аналізу недавніх експериментів.

Ключові слова: магнітний наноконтакт, потужність мікрохвильового сигналу, мікрохвильова лінія передачі, мікрохвильовий резонатор.

A possibility of application of spin-torque nano-oscillators (STNO) as a microwave signal source for the telecommunication systems is considered. The output power of microwave signal from the STNO is qualitatively estimated for the cases of typical STNO into a free space (far- and near-field zones), microwave transmission lines and resonators. The microwave power radiated from a STNO is shown to be low in comparison with the power measured by the magnetoresistance (MR) effect. However, the direct measuring of microwave power emitted from a STNO may be convenient for the case of oscillator arrays with many oscillators. The propositions about the practical application of STNOs in telecommunication devices have been made using the obtained results and the analysis of recent experiments.

Key words: spin-torque nano-oscillator, microwave power, transmission line, microwave resonator.

Introduction. One of the most perspective and fascinating tendencies of micro- and nanoelectronics evolution is the spin-wave nanoelectronics [2, 4, 13, 34, 44]. Nowadays the element base of this branch of science and technology is being quickly developed. Most of presently used spin-wave devises are created using thin ferromagnetic films (for instance, yttrium-iron garnet films [1, 3, 10]) and intended for the realization of nonlinear interaction between two or more microwave signals [1, 3, 10, 22, 42, 49]. But today there are no generators and amplifiers of spin waves with acceptable scale and performance for the electronics of the future [34, 43–44]. This problem can be solved by using recently developed new active nano-scale magnetic devices – the spin-torque nano-oscillators (STNO) (Fig. 1) – and/or the systems based on them [26–27, 31].

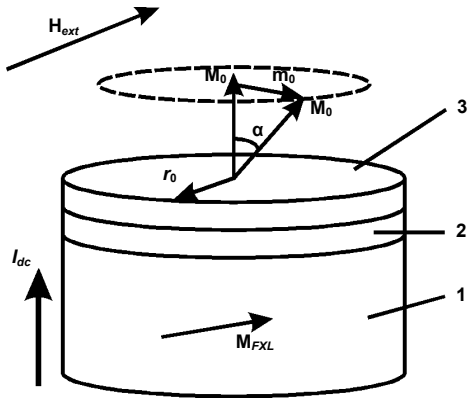

Fig. 1. The simplest model of spin-torque nano-oscillator (STNO) consists of three layers: "fixed" magnetic layer (1), thin non-magnetic spacer (2) and thin "free" magnetic layer (3). $\mathbf{M}_{FXL}$ is the magnetization vector in the "fixed" magnetic layer (1), defined by an external magnetic field $\mathbf{H}_{ext}$, geometry of the structure, etc. $\mathbf{M}_0$ is the magnetization vector in the "free" magnetic layer (3). If direct current I_{dc} passing the structure from "fixed" to "free" layer a microwave precession of magnetization with the magnetization vector $\mathbf{M}_0$ is excited; α is the precession angle and $\mathbf{m}_0$ is the excited microwave component of magnetization vector

The discovery of the spin-transfer-torque effect in magnetic multilayers, theoretically predicted by J.C. Slonczewski [45, 46] and L. Berger [7] and after that experimentally observed by many authors [9, 15, 16, 17, 19, 20, 26, 27, 38–40, 48], opened a possibility for a new method of generation of microwave oscillations that does not involve any semiconductor materials or devices [44]. The spin-transfer-torque effect turned out, that electric direct current I_{dc} passing through a magnetized magnetic layered structure becomes spin-polarized and, if the current is sufficiently high (greater than current threshold I_{th}), this spin-polarized current can transfer enough spin angular momentum between the magnetic layers to destabilize the static equilibrium orientation of magnetization in the thinner ("free") magnetic layer of the multilayered structure (see fig. 1). Depending on the actual geometry and properties of the magnetic structure and the magnitude of the external bias magnetic field, this phenomenon can lead either to the magnetization switching (reversal of the magnetization direction) [17, 28], or to the magnetization precession with the frequency close to the frequency of the ferromagnetic resonance (FMR) in the magnetic layer [19–21, 37–39]. In the last case the frequency of the current-induced precession is close to the frequency of the most unstable spin wave mode of the "free" magnetic layer (i.e. it is close to the FMR frequency), depends on the current magnitude, and, typically, lies in the microwave range. The typical eigen frequency of a STNO is 1 ÷ 50 GHz [13–14, 16], but there is theoretical prediction that it can be increased up to 200 GHz [14, 36–38].

The major advantages of the STNOs are its small sizes (the typical radius r_0 of the structure is 10÷500 nm, height of the structure is 10÷100 nm), compatibility of STNO fabrication technology with the standard micro- and nanoelectronics fabrication technology, the possibility of generation frequency tuning in a wide range [34, 44].

Practical applications of above described magnetization dynamics in non-volatile magnetic random access memory, microwave nanometer-scale oscillators, detectors, mixers and other devices are under development [9, 18, 50], and non-equilibrium states of magnetization induced by spin-transfer-torque are of fundamental interest in nonlinear science [14, 44, 52]. Also spin-transfer-torque effect is used in spin torque ferromagnetic resonance measurements of spin waves in magnetic nano-structures [8, 41, 48].

Microwave spin-torque nanometer-scale auto-oscillators based on either fully metallic giant magnetoresistance (GMR) spin valves or magnetic tunnel junctions, having a thin dielectric spacer and employing tunneling magnetoresistance (TMR) effect, are very attractive for potential applications in active nanometer-scale devices in microwave spintronics [44, 25–27, 30–33, 47]. The major problem that arises during the development and application of such devices is the small microwave output power that can be extracted from a single STNO. In the case of a STNO based on the GMR effect this power is relatively small (around one nW) [19–21, 23], while in the case

of a STNO based on the TMR effect it can reach 1 μW [15, 24, 48]. But in most cases the microwave power emitted from a typical STNO is 1–10 pW [16, 19, 23].

In all known experiments (for instance, see [9, 15, 16, 17, 19, 20, 26, 27, 38–40, 48]) the microwave signal generated by a STNO is registered, typically, as oscillations of the multilayer resistance through to the effects of giant magnetoresistance [19–21, 23] or tunneling magnetoresistance [15, 24, 48] due to the fact that in the course of precession the orientation of the magnetization of the "free" layer relative to the static magnetization of the "fixed" layer oscillates with microwave frequency. In this case, in fact, the time-dependent resistance of the STNO $R(t)$ is measured. The resistance $R(t)$ depends on time t due to the existence of a microwave magnetization precession with angular frequency $\omega_0 = 2\pi\nu_0$ in the "free" magnetic layer of the STNO, so we can separate the direct and microwave components of the resistance with amplitudes R_{dc} and R_{rf}, respectively:

$$R(t) = R_{dc} + R_{rf}\cos(\omega_0 t). \qquad (1)$$

If the direct bias current I_{dc} passing through the STNO then the characteristic microwave power W_{MR} generated by a STNO can be estimated as

$$W_{MR} \sim \frac{1}{2} I_{dc}^2 R_{dc} \left(\frac{R_{rf}}{R_{dc}}\right)^2. \qquad (2)$$

The value of R_{rf} is several percents of R_{dc} (typically 1–5 %) in real STNO devices [9, 15, 16, 17, 19, 20, 24, 26, 27, 38–40, 48]. So anyone can see, the efficiency of standard method of experimental observing the microwave power generated by a STNO is proportional to the magnetoresistance (MR) coefficient R_{rf}^2 / R_{dc}^2 and due to this circumstance is low ($\sim 10^{-4}$).

In the paper we qualitatively analyze another opportunities of detection of microwave power generated by a STNO. We consider a possibility of microwave signal detection in the near field zone of a STNO, and also a possibility of direct observation of a microwave electromagnetic radiation from a STNO. We also compare the standard method of microwave power detection based on the MR-effect and the proposed method.

Further we consider the microwave power radiated by a STNO into a free space and the microwave power generated by a STNO in a near field-zone. We also analyze a possibility to pump out the microwave power from a STNO placed in the transmission lines (rectangular waveguide and parallel-plate waveguide) and microwave resonators (rectangular cavity and parallel-plate resonator). In the last part of the paper we analyze a possibility to further increase of microwave output power generated by a single STNO or an array of synchronized STNOs.

Model. We make several natural assumptions during our analysis. First, we consider the STNO as the point object, because the any size of typical STNO is much smaller than the wavelength λ_0 of the microwave signal. Second, we use the macrospin approximation and assume the microwave component of magnetization $\mathbf{m}_0 = \mathbf{x}m_x + \mathbf{z}m_z$ is circularly polarized, so we can simply write $\mathbf{m} = (\mathbf{x} + \mathbf{z})m_0$ (see fig. 1). Third, using first and second assumptions we can consider a microwave magnetization precession in the "free" magnetic layer of the STNO as the oscillations of two point linear magnetic dipoles oriented along *x*- and *z*-axis.

During the analysis we consider the case of STNO with following typical parameters: frequency of magnetization precession $\nu_0 = 10$ GHz, saturation magnetization of the STNO "free" layer $\mu_0 M_0 = 800$ mT, STNO radius $r_0 = 100$ nm, thickness of STNO "free" layer $d_0 = 5$ nm, so the volume of STNO "free" layer is $V_0 = \pi r_0^2 d_0 \approx 153$ nm^3. We analyze only the case of maximal magnetization precession angle $\alpha_0 = 90°$. The last case is typically realized if direct current I_{dc} passing the structure is greatly exceeds the current threshold I_{th}.

In the following we do only qualitative analysis of microwave signal power emitted from a STNO. Thus, we can assume that the permittivity ε and permeability μ of the media are approximately equal to the vacuum permittivity ε_0 and vacuum permeability μ_0, respectively.

Theory. *STNO in a free space.* For the first time an approach to the analysis of electromagnetic fields generated by a STNO was presented in the recent work by N. Amin, H. Xi, and M.X. Tang [6]. The authors of the paper [6] have obtained the expressions for the electromagnetic fields of a STNO considering it as a point magnetic dipole, but no quantitative study of the microwave power emitted from the STNO has been made. Taking this into account, further we shall obtain the expression of microwave radiation power W_{FS}, emitted from a STNO into a free space in the far-field zone, and quantitatively analyze the dependence of W_{FS} on the oscillator geometry, saturation magnetization, and precession angle. Also we shall consider a possibility to takeoff a microwave power from a STNO in the near-field zone.

Using the field expressions for linear magnetic dipole [6, 35]:

$$E_\varphi = -\frac{i\omega_0 \mu m(\alpha)}{4\pi} e^{-ikr}\left(\frac{ik}{r} + \frac{1}{r^2}\right)\sin\theta\, e^{i\omega_0 t},$$

$$H_r = \frac{i\omega_0 \mu m(\alpha)}{2\pi} e^{-ikr}\left(\frac{1}{Zr^2} + \frac{1}{i\omega_0 \mu r^3}\right)\cos\theta\, e^{i\omega_0 t}, \qquad (3)$$

$$H_\theta = \frac{i\omega_0 \mu m(\alpha)}{4\pi} e^{-ikr}\left(\frac{i\omega_0 \varepsilon}{r} + \frac{1}{Zr^2} + \frac{1}{i\omega_0 \mu r^3}\right)\sin\theta\, e^{i\omega_0 t},$$

where $i = \sqrt{-1}$, μ – media permeability, ε – media permittivity, $k = 2\pi/\lambda_0$, $Z = \sqrt{\mu/\varepsilon}$ – media impedance, $m(\alpha)$ – microwave magnetization, α is the precession angle (see fig. 1), one can obtain the expression for microwave radiation power of the dipole in the far-field zone:

$$W_{dip}(\alpha) = \frac{4}{3}\pi^5 \frac{\mu_0}{c^3}\nu_0^4 m_0^2(\alpha) r_0^4 d_0^2, \qquad (4)$$

where μ_0 is the vacuum permeability, c – speed of light, ν_0 – frequency of magnetization precession in a "free" magnetic layer, $m_0(\alpha)$ – the microwave component of magnetization in a "free" magnetic layer of a STNO as the function of precession angle α (we can assume $m_0(\alpha) = M_0 \sin\alpha$, M_0 is the saturation magnetization), r_0 – the radius of a STNO, and d_0 is the thickness of "free" layer (see Fig. 1).

The formula (4) is valid for the distance between the center of STNO and a point where the power is measured $r \gg \lambda_0 = c/\nu_0$. If we substitute in Ex. (4) the typical parameters of a STNO (see Section "Model") and assume the precession angle is $\alpha = \alpha_0 = 90°$, we get the maximal microwave power radiated from the typical STNO:

$$W_{FS}^{\max} = 2W_{dip}^{\max} \approx 3.86 \cdot 10^{-22}\ \text{W}. \qquad (5)$$

In real systems, however, the direct bias current I_{dc} usually is only slightly exceed the current threshold I_{th} and due to this circumstance the precession angle is noticeably less than $90°$. One can see from Ex. (4), the microwave power in this case is

$$W_{FS}(\alpha) = W_{FS}^{\max} \sin^2 \alpha \qquad (6)$$

and nonlinearly depends on the precession angle α. So, the microwave power radiated by a STNO into a free space is near 10^{-22} W for the typical value of precession angle $\alpha = 30°$ (the case $|-1 + I_{dc}/I_{th}| \ll 1$). It is certainly such ultra low power cannot be detected by any of existing instruments. To increase the microwave radiation power of a STNO we have to increase volume of STNO "free" layer $V_0 = \pi r_0^2 d_0$ and/or the frequency of magnetization precession ν_0. But this is not convenient for many reasons and in the best case we can get the maximal radiation power only near $W_{FS}^{\max} \approx 2.5 \cdot 10^{-16}$ W, for $\nu_0 = 40$ GHz, $r_0 = 500$ nm, $d_0 = 10$ nm. Thus, the idea to use the STNO as the source of microwave radiation in a free space is not a fruitful one.

The microwave power emitted by a STNO into a free space is very low, because the amplitudes of electric and magnetic fields are very small in a far-field zone due to the dependence of the field on distance r in this zone as $E, H \sim r^{-1}$ for $r \gg \lambda_0$. In order to increase the working level of microwave power of a STNO device we have to operate with the device in a near field zone, where $r < \lambda_0$. But the microwave electromagnetic field of a STNO cannot produce the radiation in this zone [35]. We even cannot introduce time-average Poyinting vector $\mathbf{P} = 0.5\,\mathrm{Re}\left\{\left[\mathbf{E} \times \mathbf{H}^*\right]\right\}$ as it was done in the far-field zone [35]; here $\mathrm{Re}\{...\}$ is the real part of the function; **E** and **H** – complex amplitudes of the electromagnetic field, and sign "*" is marked the conjugated function. Due to this circumstance, we consider two simplest alternative methods of pumping out the microwave power from a STNO device. The first method is based on the application of a conducting loop and the second one on the application of plane capacitor.

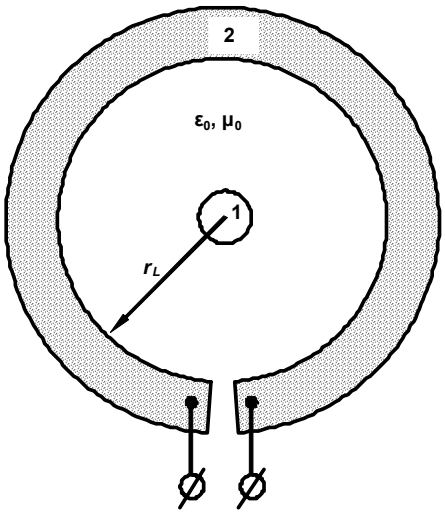

Fig. 2. A top view of a STNO (1) in the center of conducting loop (2) of radius r_L

Method of conducting loop. Let's place a STNO in the center of small conducting loop with radius $r_L \gg r_0$ (fig. 2). The magnetic flux penetrating the loop cross-section will oscillate with angular frequency $\omega_0 = 2\pi\nu_0$, because the electromagnetic field is oscillated with this frequency. The voltage $|V_L| = |d\Phi/dt|$ is arisen in the loop in this case in agreement to Faraday's law, where $\Phi = \mu_0 \,\mathrm{Re}\left\{ e^{i\omega_0 t} \int\limits_{S_L} \mathbf{H} d\mathbf{S} \right\}$ is the magnetic flux, and $S_L \approx \pi r_L^2$ is the cross-section of the loop. Further we shall obtain the voltage $|V_{dip}|$ generated in the loop by one magnetic dipole and then calculate the voltage generated in the loop by a STNO as $|V_L| \sim 2|V_{dip}|$. Using the expressions for the fields of magnetic dipole in the near field zone (3), where we neglect all terms depending or distance r except r^{-3}, we can evaluate $|V_{dip}|$ as

$$|V_{dip}(\alpha)| = 2\pi\mu_0\omega_0 \left| \int\limits_{r_0}^{r_L} H(r,\alpha)\, r dr \right| \sim$$

$$\sim \pi^2 \mu_0 \nu_0 m_0(\alpha) r_0^2 d_0 \left| \int\limits_{r_0}^{r_L} \frac{dr}{r^2} \right|, \qquad (7)$$

where $H(r,\alpha) \sim m_0(\alpha) r_0^2 d_0 / 4r^3$ is the component of magnetic field perpendicular to the loop cross-section. We note that the low integral bound in (7) is not a zero but r_0, because $H(0,\alpha) \to \infty$. Taking into account $r_0 \ll r_L$, we can get from (7) the simple expression for the $|V_L(\alpha)|$:

$$|V_L(\alpha)| \sim 2\pi^2 \mu_0 \nu_0 M_0 r_0 d_0 \sin\alpha. \qquad (8)$$

The maximal voltage $|V_L^{\max}|$ is approximately $80\ \mu$V for the typical STNO parameters. If we assume the loop has the radius $r_L = 10\ \mu$m and the loop wire has square cross-section of 50×50 nm^2 (50 nm is the typical STNO thickness), and the loop is made of gold, then the characteristic resistance of the loop would be $R_L \approx 503$ Ohm. The maximal characteristic microwave power that can be taken off by the conducting loop from a STNO then would be

$$W_L^{\max} \sim |V_L^{\max}|^2 / 2R_L \sim 6\ \text{pW}. \qquad (9)$$

However, in real experiment this power would be less, because the precession angle α typically is less than $90°$: $W_L(\alpha) = W_L^{\max} \sin^2\alpha$.

Method of plane capacitor. Let's place a STNO in the center of plane square capacitor with the characteristic size of capacitor plate $l_C \gg r_0$ and the distance between the plates d_C (Fig. 3). The space within the capacitor plates is filled with dielectric with permittivity $\varepsilon \sim \varepsilon_0$ in our simple model. Using the expressions for the fields of magnetic dipole in the near field zone [35], where we neglect all terms depending or distance r except r^{-2}, we can evaluate the voltage $|V_{dip}|$ applied to the capacitor as

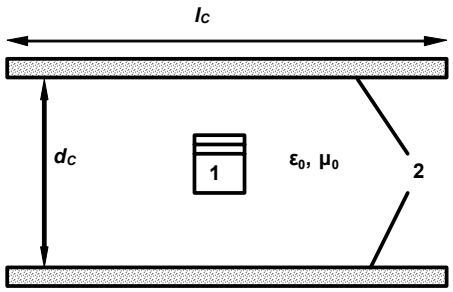

Fig. 3. A front view of a STNO (1) between the plates (2) of plane capacitor

$$\left|V_{dip}(\alpha)\right| = \int E(r,\alpha)\,dr \sim$$

$$\pi\mu_0\nu_0 m_0(\alpha) r_0^2 d_0 \left| \int_{r_0}^{d_C/2} \frac{dr}{r^2} \right| \sim \pi\mu_0\nu_0 m_0(\alpha) r_0 d_0 , \quad (10)$$

where $E(r,\alpha) \sim \mu_0\nu_0\, m_0(\alpha)\pi r_0^2 d_0 / 2r^2$ is the component of electric field of the dipole. We note that the low integral bound in (10) is not a zero but r_0, because $E(0,\alpha) \to \infty$. Also we took into account $r_0 \ll d_C$ in (10). The voltage generated by a STNO in the capacitor is

$$\left|V_C\right| \sim 2\left|V_{dip}\right| = 2\pi\mu_0\nu_0 M_0 r_0 d_0 \sin\alpha . \quad (11)$$

The maximal voltage is approximately $25\ \mu\text{V}$ for the typical STNO with written above typical parameters and $\alpha_0 = 90°$. This voltage is applied to the characteristic capacitance $C = \varepsilon_0 l_C^2 / d_C$. If we assume the capacitor sizes are $l_C = 10\ \mu\text{m}$ and $d_C = 1\,\mu\text{m}$, then the characteristic capacitance would be $C \approx 8.8\cdot 10^{-16}$ F. The maximal characteristic microwave power $W_C^{\max}$ that can be taken off by the capacitor from a STNO then would be

$$W_C^{\max} \sim 0.5\cdot\nu_0 C\left|V_C^{\max}\right|^2 \sim 2.8\cdot 10^{-15}\ \text{W} . \quad (12)$$

However, in real experiment this power would be less, because the precession angle α typically is less than 90° and $W_C(\alpha) = W_C^{\max}\sin^2\alpha$.

We have shown the microwave power that can be taken off from a STNO is much greater in the near-field zone than the radiation power in the far-field zone. But the absolute value of the power that can be pumped out from a STNO in the near field zone is very small. The maximal value of microwave power is about of 6 pW for the method of conducting loop and approximately 3 fW for the method of plane capacitor. One can see these two methods allow increasing the level of microwave power that one can pump out from the STNO. But nevertheless this power is very low, so these simple methods may be not useful in the real experiment.

STNO in transmission lines: general analysis. Further we shall analyze the excitation of a rectangular waveguide (due to the simplicity of this task) and a parallel-plate waveguide (the simplest model of a microstrip line) by a microwave precession magnetization in a "free" layer of a STNO. We shall demonstrate the increasing of a microwave power radiated by a STNO into these transmission lines in comparison with the microwave power emitted from a STNO into a free space.

In the following we assume the microwave precession of magnetization excites the electromagnetic field in the transmission line. This problem can be easily analyzed if we introduce the magnetic current with density

$$\mathbf{j}^m = 2\pi\mathrm{i}\nu_0 m_0(\alpha)(\mathbf{x}+\mathbf{z}) . \quad (13)$$

This current describes the source of the electromagnetic field in our problem. Thus, using the Lorentz' lemma for any electromagnetic fields $\mathbf{E}_1, \mathbf{H}_1$ and $\mathbf{E}_2, \mathbf{H}_2$ in the transmission line [30, 35], we can obtain the amplitude of excited *s*-wave mode in the line in the form:

$$C_s = -\frac{\int_{V_0} \mathbf{j}^m \mathbf{H}_{-s}\,dV}{\int_{S_\perp} \left\{\left[\mathbf{E}_s\times\mathbf{H}_{-s}\right] - \left[\mathbf{E}_{-s}\times\mathbf{H}_s\right]\right\}\mathbf{z}\,dS} , \quad (14)$$

where index *s* corresponds to the wave propagating in the direction + *z*, and index –*s* corresponds to the wave propagating in the direction – *z*; volume V_0 is the volume of a "free" layer of a STNO, where $\mathbf{j}^m \neq 0$; $S_\perp$ is the cross-section surface for the transmission line. The microwave power transmitted in the transmission line in + *z* direction from a STNO can be evaluated as

$$W_s = \frac{1}{2}\mathrm{Re}\left\{\int_{S_\perp}\left[\mathbf{E}_s\times\mathbf{H}_s^*\right]\mathbf{z}\,dS\right\} =$$

$$= \frac{1}{2}\mathrm{Re}\left\{\int_{S_\perp}\left(E_{sx}H_{sy}^* - E_{sy}H_{sx}^*\right)dS\right\} , \quad (15)$$

where the field components are proportional to the C_s given by (14).

Rectangular waveguide. The rectangular hollow waveguide with cross-section $a\times b$ (*a* is the size of wide wall, *b* is the size of narrow wall) is one of the simplest transmission lines used in a microwave band (that is the main reason why we analyze this structure). In the following we assume that only a fundamental mode (TE_{10} mode) of the waveguide is excited by a STNO. Also we assume there are no losses in the system.

The field components of mode TE_{10} of rectangular waveguide with unit amplitude can be written in the form [30, 35]:

$$H_{\pm z} = \cos\left(\frac{\pi}{a}x\right)e^{\mp\mathrm{i}\beta z} ,$$

$$E_{\pm y} = -\mathrm{i}\omega_0\mu_0\frac{a}{\pi}\sin\left(\frac{\pi}{a}x\right)e^{\mp\mathrm{i}\beta z} , \quad (16)$$

$$H_{\pm x} = \pm\mathrm{i}\beta\frac{a}{\pi}\sin\left(\frac{\pi}{a}x\right)e^{\mp\mathrm{i}\beta z} ,$$

where $\beta = \sqrt{\frac{\omega^2}{c^2} - \frac{\pi^2}{a^2}}$ is a propagation constant.

We introduced the magnetic current density $\mathbf{j}^m$ as a vector function with non-zero *x*- and *z*-components. Taking this into account, we can divide the problem of waveguide excitation on two sub-problems: excitation by the magnetic current with density $\mathbf{x}j_x^m$ and excitation by the magnetic current with density $\mathbf{z}j_z^m$, where j_x^m and j_z^m are the *x*- and *z*-components of $\mathbf{j}^m$, respectively. In the first case the amplitude of the excited wave is (see Ex. (14))

$$C_s \equiv C_x = \frac{\pi m_0(\alpha)V_0}{a^2 b}\sin\left(\frac{\pi}{a}x_0\right), \quad (17)$$

where x_0 is the coordinate of the point, where the STNO is located. In the second case the amplitude of the wave is

$$C_s \equiv C_z = \mathrm{i}\pi^2\frac{m_0(\alpha)V_0}{a^3 b\beta}\cos\left(\frac{\pi}{a}x_0\right). \quad (18)$$

One can see from (17)–(18) the amplitude of excited wave is strongly enough depends on the coordinate of the STNO position within the waveguide. If we assume $x_0 = a/2$, then $C_z = 0$. In the opposite case, when $x_0 = 0, a$, $C_x = 0$. Further, we shall analyze two cases of optimal excitation ($C_x = \max, C_z = 0$ and $C_z = \max, C_x = 0$).

Using the expression (16) for field components, Ex. (15) can be simplified to

$$W_{RW} = Z_0 \frac{a^3 b}{\lambda_0^2} C_s^2 \sqrt{1-\left(\frac{\lambda_0}{2a}\right)^2}, \qquad (19)$$

where W_{RW} is a microwave power transmitted in the rectangular waveguide in $+z$ direction from a STNO, $Z_0 \approx 377$ Ohm. If $C_x = \max, C_z = 0$ then the power is

$$W_{RW} \equiv W_x = \pi^2 Z_0 \frac{m_0^2(\alpha) V_0^2}{ab\lambda_0^2} \sqrt{1-\left(\frac{\lambda_0}{2a}\right)^2}. \qquad (20)$$

In the case $C_z = \max, C_x = 0$, the power would be

$$W_{RW} \equiv W_z = \pi^4 Z_0 \frac{m_0^2(\alpha) V_0^2}{\lambda_0^2 a^3 b\beta^2} \sqrt{1-\left(\frac{\lambda_0}{2a}\right)^2}. \qquad (21)$$

Using these formulae we obtain the maximal values of power

$$W_x^{\max} \approx 2.7 \cdot 10^{-17} \text{ W}, \quad W_z^{\max} \approx 2.0 \cdot 10^{-17} \text{ W} \qquad (22)$$

for the typical STNO with parameters shown in Sec. "Model", $\alpha = 90°$, and the waveguide with sizes $a = 23$ mm, $b = 50$ nm.

One can see the microwave power that can be emitted in the waveguide from a STNO is less than in case of conducting loop or plain capacitor but greater than the power emitted into a free space. The reason of this is the existence of cutoff frequency for the waveguide fields that limits the cross-section size of the transmission line. In order to increase the emitted power we must use the transmission line with much smaller size of the cross-section. It can be done for the transmission lines with zero or very low cutoff frequency, for instance, for the microstrip line.

Microstrip line. The precise theory of the microstrip lines is complex enough. Since our task is to make a qualitative analysis, we will analyze the simplest case of the microstrip line, the parallel-plate transmission line. So, we shall consider the microstrip line as the two parallel each other metallic plates of width a with a dielectric layer of permittivity $\varepsilon \sim \varepsilon_0$ between the plates. The thickness of dielectric layer (that is the distance between the metallic plates) is b. The other limitations of our model are:

1) We assume there is no electromagnetic field out of the cross-section $a \times b$ bounded by the metal plates. So the energy of the electromagnetic field is zero if $-a/2 > x > a/2$; $-b/2 > y > b/2$.

2) We will analyze the excitation only a fundamental TEM-wave in the microstrip line.

Using Ex. (14) the amplitude of excited TEM-wave can be obtained in the form:

$$C_s = -\mathrm{i} \frac{\pi \nu_0 \mu_0}{2ab} m_0(\alpha) V_0. \qquad (23)$$

The power transmitted into a microstrip line is given by an Ex. (15):

$$W_{MSL} = \frac{1}{2}|C_s|^2 \frac{1}{Z_0} ab = \frac{\pi^2}{8} \frac{\mu_0^2}{Z_0} \frac{\nu_0^2}{ab} m_0^2(\alpha) V_0^2. \qquad (24)$$

The maximal value of microwave power transmitted in the microstrip line $W_{MSL}^{\max} \approx 10^{-13}$ W for the typical STNO and the microstrip line with sizes $a = 1\,\mu$m, $b = 50$ nm.

One can see, the method of exciting the transmission lines by a microwave magnetization precession of a "free" layer of STNO has less efficiency than the methods based on the pumping out the microwave power in the near field zone of STNO. To increase the power level, we have to investigate the excitation of microwave oscillations in the resonator by the microwave components of magnetization in a STNO "free" layer.

STNO in resonators: general analysis. Further we shall analyze the excitation of oscillations in microwave resonators by a STNO. The cases of rectangular and microstrip resonators will be considered.

We begin the analysis by writing Maxwell's equations for the electromagnetic field $\mathbf{E}$, $\mathbf{H}$, excited by an external magnetic current with density $\mathbf{j}^m$:

$$\mathrm{rot}\,\mathbf{E} + \mathrm{i}\omega\mu\mathbf{H} = -\mathbf{j}^m, \quad \mathrm{rot}\,\mathbf{H} - \mathrm{i}\omega\varepsilon\mathbf{E} = 0, \qquad (25)$$

where ε and μ – permittivity and permeability of the media inside the resonator. The fields $\mathbf{E}$, $\mathbf{H}$ can be presented as a series expansion by eigen fields $\mathbf{E}_n$, $\mathbf{H}_n$ of the resonator and some gradient functions [1]:

$$\mathbf{E} = \sum_n A_n \mathbf{E}_n - \mathrm{grad}\,\Psi_e, \quad \mathbf{H} = \sum_n B_n \mathbf{H}_n - \mathrm{grad}\,\Psi_h, \qquad (26)$$

where n is the generalized mode index. The eigen fields $\mathbf{E}_n$, $\mathbf{H}_n$ are the solution of the uniform equations:

$$\mathrm{rot}\,\mathbf{E}_n + \mathrm{i}\omega_n\mu\mathbf{H}_n = 0, \quad \mathrm{rot}\,\mathbf{H}_n - \mathrm{i}\omega_n\varepsilon\mathbf{E}_n = 0. \qquad (27)$$

The eigen fields and gradient functions satisfy the following orthogonal conditions [1]:

$$\int_V \mathbf{E}_n^* \varepsilon \mathbf{E}_{n'} dV = N_n^e \Delta_{nn'}, \quad \int_V \mathbf{H}_n^* \mu \mathbf{H}_{n'} dV = N_n^h \Delta_{nn'},$$

$$\int_V \mathbf{E}_n^* \varepsilon\, \mathrm{grad}\,\Psi_e dV = \int_V \mathbf{H}_n^* \mu\, \mathrm{grad}\,\Psi_h dV = 0,$$

$$\Delta_{nn'} = \begin{cases} 1, & n = n' \\ 0, & n \neq n' \end{cases}. \qquad (28)$$

From Ex. (25)–(28) one can obtain the expressions for the coefficients A_n and B_n:

$$A_n = \frac{\omega\omega_n}{\omega_n^2 - \omega^2} \frac{G_n}{N_n^h}, \quad B_n = \frac{\omega^2}{\omega_n^2 - \omega^2} \frac{G_n}{N_n^h}, \qquad (29)$$

where $G_n = \int_V \mathbf{H}_n^* \mu \mathbf{m} dV$. It is certainly A_n and B_n are infinite at the frequency $\omega = \omega_n$. But this case is the most important and interesting. To analyze the excitation of the resonator at the frequency $\omega \approx \omega_n$ we introduce the Q-factor of the resonator $Q_n = \frac{\omega_n}{|\omega_n - \omega|}$ and assume $Q_n \gg 1$. In that case Ex. (29) is transformed to the following

$$A_n \approx \frac{1}{2} Q_n \frac{G_n}{N_n^h}, \quad B_n \approx \frac{1}{2} Q_n \frac{G_n}{N_n^h}. \qquad (30)$$

Neglecting the gradient functions in (26), the power pumped in a n-resonance mode by the STNO can be calculated as

$$W_n = \frac{\nu_n}{2Q_n}\left(A_n^2 N_n^e + B_n^2 N_n^h\right). \qquad (31)$$

Rectangular resonator. We shall analyze the excitation H_{101} mode of hollow rectangular cavity of volume $V = a \times b \times l$ by the STNO. The electromagnetic fields of H_{101} mode have the form [6, 35]:

$$E_y = A_n \sin\left(\frac{\pi}{a}x\right)\sin\left(\frac{\pi}{l}z\right),$$

$$H_x = -\mathrm{i}\frac{A_n}{Z_0}\frac{\lambda_0}{2l}\sin\left(\frac{\pi}{a}x\right)\cos\left(\frac{\pi}{l}z\right),$$

$$H_z = \mathrm{i}\frac{A_n}{Z_0}\frac{\lambda_0}{2a}\cos\left(\frac{\pi}{a}x\right)\sin\left(\frac{\pi}{l}z\right). \quad (32)$$

The power W_{H101} pumped in the resonator by STNO can be calculated using Ex. (31) and the maximum value of the electric field (see Ex. (32)):

$$W_{H101} = \frac{\varepsilon_0}{2}\int_0^a dx\int_0^b dy\int_0^l dz\left|E_{y\max}\right|^2 = \frac{\nu_n}{Q_n}\frac{\varepsilon_0 A_n^2}{8}abl. \quad (33)$$

We can consider the STNO as the "point" object located in the point (x_0, y_0, z_0) inside the cavity, so

$$G_n = \mathrm{i}\mu_0 m_0(\alpha)V_0\frac{1}{Z_0}\frac{\lambda_0}{2}\times$$

$$\times\left[\frac{1}{l}\sin\left(\frac{\pi}{a}x_0\right)\cos\left(\frac{\pi}{l}z_0\right) - \frac{1}{a}\cos\left(\frac{\pi}{a}x_0\right)\sin\left(\frac{\pi}{l}z_0\right)\right]. \quad (34)$$

The norm N_n^h is

$$N_n^h = \mu_0\frac{1}{Z_0^2}\frac{abl}{16}\lambda_0^2\left(\frac{1}{l^2}+\frac{1}{a^2}\right), \quad (35)$$

so the excitation coefficient A_n is

$$A_n \approx 4\mathrm{i}Q_n\frac{1}{\lambda_0}\frac{m_0(\alpha)V_0Z_0}{abl}\frac{l^2a^2}{a^2+l^2}\times$$

$$\times\left[\frac{1}{l}\sin\left(\frac{\pi}{a}x_0\right)\cos\left(\frac{\pi}{l}z_0\right) - \frac{1}{a}\cos\left(\frac{\pi}{a}x_0\right)\sin\left(\frac{\pi}{l}z_0\right)\right]. \quad (36)$$

If, for instance, $x_0 = a/2$, $z_0 = 0$, then

$$A_n = 4\mathrm{i}Q_n\frac{1}{\lambda_0}\frac{a}{b}m_0(\alpha)V_0Z_0\frac{1}{a^2+l^2} \quad (37)$$

and

$$W_{H101}(\alpha) = 2\varepsilon_0 Q_n\frac{\nu_n}{\lambda_0^2}\left(\frac{a}{b}\right)^2\times$$

$$\times m_0^2(\alpha)V_0^2Z_0^2\left(\frac{1}{a^2+l^2}\right)^2 abl. \quad (38)$$

For the values $a = 23$ mm, $b = 50$ nm, $\nu_n = \nu_0$, $Q_n = 10^5$, $l(\lambda_0) = \dfrac{\lambda_0 a}{\sqrt{4a^2-\lambda_0^2}}$ and the typical STNO parameters one can obtain $W_{H101}^{\max} \approx 1.6\cdot 10^{-13}$ W.

Microstrip resonator. In this section of the paper we analyze the excitation of TEM_1 mode in a microstrip resonator of cross-section $a \times b$ and length $l = \lambda_0/2$; its volume is $V = a \times b \times l$. The electromagnetic field of TEM-mode in the resonator has the form:

$$E_y = A_n\sin\left(\frac{\pi}{l}z\right),\ H_x = -\frac{A_n}{Z_0}\cos\left(\frac{\pi}{l}z\right). \quad (39)$$

The microwave power W_{MSR} pumped in the resonator from the STNO can be calculated using the maximum value of the electric field:

$$W_{MSR} = \frac{\nu_n}{Q_n}\frac{\varepsilon_0}{2}\int_0^a dx\int_0^b dy\int_0^l dz\left|E_{y\max}\right|^2 = \frac{\nu_n}{Q_n}\frac{\varepsilon_0}{4}\left|A_n\right|^2 abl, \quad (40)$$

where

$$A_n \approx \frac{1}{2}Q_n\frac{G_n}{N_n^h} = -Q_n\frac{m_0(\alpha)V_0Z_0}{abl}\cos\left(\frac{\pi}{l}z_0\right),$$

$$G_n = -\mu_0\frac{m_0(\alpha)V_0}{Z_0}\cos\left(\frac{\pi}{l}z_0\right),$$

$$N_n^h = \mu_0\frac{1}{2Z_0^2}abl.$$

If, for instance, $z_0 = 0$, then

$$W_{MSR} = \frac{\nu_0}{Q_n}\frac{\varepsilon_0}{4}\left|A_n\right|^2 abl =$$

$$= \nu_0\frac{\varepsilon_0}{4}Q_n\frac{m_0^2(\alpha)V_0^2Z_0^2}{abl}. \quad (41)$$

For the values $a = 10$ μm, $b = 50$ nm, $Q_n = 10^3$, and typical STNO parameters, one can obtain the maximal power $W_{MSR}^{\max} \approx 4.2$ pW.

Results and discussion. The major obtained results are summarized in the Table 1, shown below. The table contains 5 columns including the column "Expression", which describes the expression used for calculation of the maximal registered microwave power, emitted from the analyzed system; the next column "Parameters" describes the parameters of the system used for calculations (default parameters of a STNO is shown earlier, in Section "Model") and the last column shows the value of calculated power in watts.

So, we have shown (see Table 1) the microwave signal power that can be gained from a STNO is very small for the case of signal observation in the near-field zone of STNO or for the case of radiation signal observation. One can see from the Table 1 the microstrip resonator has little advantages in comparison with the other systems. It has small sizes, can be made using planar technology and allow to detect high enough microwave power emitted from a STNO (comparable to the microwave power registered through the MR effect for the case of GMR STNOs). Taking this into account we shall analyze the results of recent experiments and make some conclusions about applications of microstrip systems with STNOs.

The recent experiments carried out in U.S. Army Research Laboratory (ARL) [51] have shown a potential possibility of creation communication devices based on STNOs. Since the microwave power radiated by a single STNO is very small, in ARL experiment the ac voltage output from a STNO was applied to the coaxial cable connected to the waveguide horn antenna. This horn antenna was the transmitter of the microwave signal. Another horn antenna, located at the distance of approximately one meter from the transmitter, was the receiver. The power of received signal in ARL experiment was about 250 pW. In this case the power output from a STNO (maximal power applied to the coaxial cable) is given by Ex. (2). This power is low (typically $\sim 1 \div 10^2$ nW), but it is greater than the characteristic microwave power radiated by a STNO into a transmission line.

Table 1. Summary results for all considered systems with a single STNO that has typical parameters (see Section "Model")

№	Analyzed system	Expression for maximal microwave power	Parameters	Maximal microwave power, Watt
1.	Registering the power from a STNO through magnetoresistance effect	$W_{MR} \sim \frac{1}{2} I_{dc}^2 R_{dc} \left(\frac{R_{rf}}{R_{dc}} \right)^2$	Typical GMR based STNO: Typical TMR based STNO:	$10^{-12} \div 10^{-9}$ $10^{-9} \div 10^{-6}$
2.	STNO in a free space (far-field zone)	$W_{FS} = \frac{8}{3} \pi^5 \frac{\mu_0}{c^3} \nu_0^4 M_0^2 r_0^4 d_0^2$	See Section "Model"	$3.9 \cdot 10^{-22}$
3.	STNO in the center of a conducting loop (near-field zone)	$W_L \sim \frac{2\pi^4 \mu_0^2 \nu_0^2 M_0^2 r_0^2 d_0^2}{R_L}$	$r_L = 10\ \mu\text{m}$, $R_L \approx 503$ Ohm	$6 \cdot 10^{-12}$
4.	STNO between the plates of plane square capacitor (near-field zone)	$W_C \sim \frac{2\pi^2 \mu_0^2 \nu_0^3 M_0^2 r_0^2 d_0^2 \varepsilon_0 l_C^2}{d_C}$	$l_C = 10\ \mu\text{m}$, $d_C = 1\ \mu\text{m}$	$2.8 \cdot 10^{-15}$
5.	STNO in rectangular waveguide	$W_{RW} = \pi^2 Z_0 \frac{M_0^2 V_0^2}{ab\lambda_0^2} \sqrt{1 - \left(\frac{\lambda_0}{2a} \right)^2}$ $W_{RW} = \pi^4 Z_0 \frac{M_0^2 V_0^2}{\lambda_0^2 a^3 b \beta^2} \sqrt{1 - \left(\frac{\lambda_0}{2a} \right)^2}$	$a = 23$ mm, $b = 50$ nm, $\lambda_0 = 3$ cm, $\beta = \sqrt{\frac{\omega^2}{c^2} - \frac{\pi^2}{a^2}}$.	$2.7 \cdot 10^{-17}$ $2 \cdot 10^{-17}$
6.	STNO in parallel-plate transmission line (model of microstrip line)	$W_{MSL} = \frac{\pi^2}{8} \frac{\mu_0^2}{Z_0} \frac{\nu_0^2}{ab} M_0^2 V_0^2$	$a = 1\ \mu\text{m}$, $b = 50$ nm	10^{-13}
7.	STNO in rectangular cavity	$W_{H101} = 2\varepsilon_0 Q_n \frac{\nu_0}{\lambda_0^2} \left(\frac{a}{b} \right)^2 \times$ $\times M_0^2 V_0^2 Z_0^2 \left(\frac{1}{a^2 + l^2} \right)^2 abl$	$a = 23$ mm, $b = 50$ nm, $Q_n = 10^5$, $l(\lambda_0) = \frac{\lambda_0 a}{\sqrt{4a^2 - \lambda_0^2}}$	$1.6 \cdot 10^{-13}$
8.	STNO in parallel-plate resonator (model of microstrip resonator)	$W_{MSR} = \nu_0 \frac{\varepsilon_0}{4} Q_n \frac{M_0^2 V_0^2 Z_0^2}{abl}$	$a = 10\ \mu\text{m}$, $b = 50$ nm, $Q_n = 10^3$	$4.2 \cdot 10^{-12}$

Although the ARL experiment has shown for the first time the possibility of creation communication devices based on STNOs, its experimental realization is not very convenient for the practical applications. The major discomfort is arisen due to the use of waveguide horn antenna. The use of such type of antenna takes us away from the micro- and nanoelectronics. In this situation we propose to use a microstrip antenna. In order to minimize the sizes of the system this can be a quarter-wave microstrip antenna. It can have the trapezium shape in plane. The one side of the antenna could have a typical size of STNO (~200 nm) and the second side could have a size of millimeter or less (for the best matching to a free space). The length of the antenna is less than 7.5 mm for the STNO operating at frequency 10 GHz. If we use the antenna on a dielectric substrate with permittivity $\varepsilon \gg \varepsilon_0$ than the antenna sizes would be smaller. In real system such antenna could be a part of the microchip shell.

It was shown in ARL experiment the typical STNO is a real resistance device. The value of this resistance is typically 10 Ohm. In order to increase the efficiency of the system, the microstrip antenna must match STNO and a free space, i.e. the resistance of the antenna has to be

$$\sqrt{10\ \text{Ohm} \cdot 377\ \text{Ohm}} \approx 61.5\ \text{Ohm} \text{ at 10 GHz.} \qquad (42)$$

Taking into account the very small microwave power radiated in space by a single STNO, the most perspective way of creation communication devices is the use of arrays of synchronized STNOs. Similar problems have almost already solved in low-temperature and high-temperature superconducting electronics for the Josephson junctions [11, 25]. The difference between the Josephson junction and the STNO is the substantial and principal non-linearity of the last one. Due to this circumstance the well-known Kuramoto' model [5] frequently used for the analysis of various processes in Josephson junction arrays is not always correct for the arrays of STNOs.

The characteristic value of operating level microwave power of modern telecommunication devices is around 10 ÷ 1000 μW, thus, one can see in order to create a practical source of microwave signals based on STNOs it would be useful to use arrays of coupled and synchronized STNOs [32–33, 40, 44].

There are two approaches to create such an array of STNOs. The first (traditional) approach is to form an array of N oscillators connected in parallel or in series and coupled by a common bias current. In such a case, as it was shown in [12], the output power extracted through the magnetoresistance mechanism (GMR or TMR) from an array of N synchronized STNOs is N times larger than the power of a single STNO. The second approach is to place N STNOs (coupled through their electromagnetic fields) inside a resonator with a high Q-factor and extract the power through the direct emission mechanism, described in the paper. In that case, as it was shown in [1, 29], the output power of the N oscillator array can be N^2 times larger than the power of a single oscillator. If we use the microstrip resonator with parameters $a = 1\ \mu\text{m}$, $b = 50$ nm, $Q_n = 10^3$, and an array of 10 almost identical STNOs with typical parameters (see Section "Model"), we can achieve the total output power from the array is near 0,5 nW. It is no doubt this power is high enough to be detected by existing instruments.

The last but important problem remains in this area of electronics can be formulated as: in order to use a single STNO and oscillator arrays in telecommunication devices it is necessary to provide a special device, which from the one hand allow to effectively transmit the microwave signal generated by a STNO or an array of synchronized STNOs, receive the external microwave signal (which can be a signal from another STNO), and on the second hand allow to effectively match the impedance of a single STNO (or STNO ar-

rays) with the impedance of a transmission line. The simplest type of above described device is a matched microwave antenna, which application allows solving all considered problems simultaneously. This is no doubt the developing of such antenna with ultra-low sizes and acceptable performance can lead to the development of novel class of microwave devices based on STNO and STNO arrays that utilizes the direct electromagnetic emission from a STNOs.

Conclusion. In summary, one have analytically studied on a qualitative level the possibility of application of STNOs and its arrays as the microwave signal sources. One have demonstrated that the microwave power radiated from a single STNO in a free space is ultra low and cannot be measured by any of existing instruments. If one shall measure the microwave signal in near-field zone of STNO or measure the power emitted by a STNO in transmission lines, one can achieve only the power level of several pW or less. But for the STNO inserted in the resonance system one can achieve the microwave power of several tens of pW. Although this power level is not very high, the direct measuring of microwave power emitted from a STNO may be convenient for the case of arrays with many (N) synchronized oscillators due to the dependence of registered microwave power on N as N^2. Using obtained results and the results of recent experiments it is possible to conclude that STNO may be a usable as base element of various microstrip planar telecommunication devices operating in microwave frequency band and tuned by an external dc magnetic field and/or by the bias dc current.

The author would like to thank Prof. Andrei Slavin and Dr. Vasil Tiberkevich for their encouragement and fruitful discussions.

This work was supported in part by grant M/90–2010 from the Ministry of Education and Science of Ukraine and by grant UU34/008 from the State Fund for Fundamental Research of Ukraine.

1. *Гуревич А. Г., Мелков Г. А.* Магнитные колебания и волны. – М., 1994. 2. *Мелков Г., Прокопенко О.* Умови надвисокочастотної синхронізації для магнітних наноконтактів, розташованих у шарі магнітовпорядкованої речовини // Вісник Київського національного університету імені Тараса Шевченка. Серія: радіофізика та електроніка. – 2007. – № 10. 3. *Мойсеенко В. А., Мелков Г. А., Васючка В. І., Прокопенко О. В., Слободянюк Д. В.* Кореляційна обробка інформації в плівках залізо-ітрієвого гранату // Вісник Київського університету. Серія: фізико-математичні науки. – 2008. – № 4. 4. *Прокопенко О. В., Верба Р. В., Борисенко М. О.* Вузькосмуговий режим вимушеної фазової синхронізації магнітних наноконтактів // Вісник Київського національного університету імені Тараса Шевченка. Серія: фізико-математичні науки. – 2008. – № 3. 5. *Acebron J. A., Bonilla L. L., Perez Vicente C. J., Ritort F., Spigler R.* The Kuramoto model: a simple paradigm for synchronization phenomena // Review of Modern Physics. – 2005. – Vol. 77. 6. *Amin N., Xi H., Tang M. X.* Analysis of electromagnetic fields generated by a spin-torque oscillator // IEEE Transaction on Magnetics. – 2009. – Vol. 45. 7. *Berger L.* Emission of spin waves by a magnetic multilayer traversed by a current // Physical Review B. – 1996. – Vol. 54. 8. *Boone C.T., Katine J. A., Childress J. R., Tiberkevich V., Slavin A., Zhu J., Cheng X., Krivorotov I. N.* Resonant nonlinear damping of quantized spin waves in ferromagnetic nanowires: a spin torque ferromagnetic resonance study // Physical Review Letters. – 2009. – Vol. 103. 9. *Cheng X., Boone C. T., Zhu J., Krivorotov I. N.* Nonadiabatic stochastic resonance of a nanomagnet excited by spin torque // Physical Review Letters. – 2010. – Vol. 105. 10. *Chumak A. V., Serga A. A., Hillebrands B., Melkov G. A., Tiberkevich V., Slavin A. N.* Parametrically stimulated recovery of a microwave signal using standing spin-wave modes of a magnetic film // Physical Review B. – 2009. – Vol. 79. 11. *Duzer T. V., Turner C. W.* Superconductive Devices and Circuits. – NJ, 1999. 12. *Georges B., Grollier J., Cros V., Fert A.* Impact of the electrical connection of spin transfer nano-oscillators on their synchronization: an analytical study // Applied Physics Letters. – 2008. – Vol. 92. 13. *Heide C.* Spin Currents in Magnetic Films // Physical Review Letters. – 2001. – Vol. 87. 14. *Hoefer M. A., Ablowitz M. J., Ilan B., Pufall M.R., Silva T. J.* Theory of Magnetodynamics Induced by Spin Torque in Perpendicularly Magnetized Thin Films // Physical Review Letters. – 2005. – Vol. 95. 15. *Houssameddine D., Ebels U., Delaët B., Rodmacq B., Firastrau I., Ponthenier F., Brunet M., Thirion C., Michel J.-P., Prejbeanu-Buda L., Cyrille M.-C., Redon O., Dieny B.* Spin-torque oscillator using a perpendicular polarizer and a planar free layer // Nature Materials. – 2007. – Vol. 6. 16. *Kaka S., Pufall M. R., Rippard W. H., Silva T. J., Russek S. E., Katine J. A.* Mutual phase-locking of microwave spin torque nano-oscillators // Nature. – 2005. – Vol. 437. 17. *Katine J. A., Albert F. J., Buhrman R. A., Myers E. B., Ralph D. C.* Current-driven magnetization reversal and spin-wave excitations in Co/Cu // Physical Review Letters. – 2000. – Vol. 84. 18. *Katine J. A., Fullerton E. E.* Device implications of spin-transfer torques // Journal of Magnetism and Magnetic Materials. – 2008. – Vol. 320. 19. *Kiselev S. I., Sankey J. C., Krivorotov I. N., Emley N. C., Schoelkopf R. J., Buhrman R. A., Ralph D. C.* Microwave oscillations of a nanomagnet driven by a spin polarized current // Nature. – 2003. – Vol. 425. 20. *Kiselev S. I., Sankey J. C., Krivorotov I. N., Emley N. C., Rinkoski M., Perez C., Buhrman R. A., Ralph D. C.* Current-induced nanomagnet dynamics for magnetic fields perpendicular to the sample plane // Physical Review Letters. – 2004. – Vol. 425, № 3. 21. *Kiselev S. I., Sankey J. C., Krivorotov I. N., Emley N. C., Garcia A.G.F., Buhrman R. A., Ralph D. C.* Spin-transfer excitations of permalloy nanopillars for large applied currents // Physical Review B. – 2005. – Vol. 72. 22. *Kobeliatskyi V., Melkov G., Moiseienko V., Prokopenko O.* Correlation receiver with wave front reversal of magnetostatic waves // Вісник Київського національного університету імені Тараса Шевченка. Серія: радіофізика та електроніка. – 2010. – № 13. 23. *Krivorotov I.N., Emley N. C., Sankey J. C., Kiselev S. I., Ralph D. C., Buhrman R. A.* Time-domain measurements of nanomagnet dynamics driven by spin-transfer torques // Science. – 2005. – Vol. 307. 24. *Lee K. J., Deac A., Redon O., Nozières J.-P., Dieny B.* Excitations of incoherent spin waves due to spin-transfer torque // Nature Materials. – 2004. – Vol. 3. 25. *Likharev K. K.* Dynamics of Josephson Junctions and Circuits. – N.-Y., 1986. 26. *Mancoff F. B., Rizzo N. D., Engel B. N., Tehrani S.* Area dependence of high-frequency spin-transfer resonance in giant magnetoresistance contacts up to 300 nm diameter // Applied Physics Letters. – 2006. – Vol. 88. 27. *Mancoff F. B., Rizzo N. D., Engel B. N., Tehrani S.* Phase-locking in double-point-contact spin-transfer devices // Nature. – 2005. – Vol. 437. 28. *Myers E. B., Ralph D. C., Katine J. A., Louie R. N., Buhrman R. A.* Current-induced switching of domains in magnetic multilayer devices // Science. – 1999. – Vol. 285. 29. *Pikovsky A., Rosenblum M., Kurths J.* Synchronization: a universal concept in nonlinear sciences. – Cambridge, 2007. 30. *Pozar D. M.* Microwave Engineering. –N.-Y., 1998. 31. *Prinz G. A.* Magnetoelectronics // Science. – 1998. – Vol. 282. 32. *Prokopenko O., Tyberkevych V., Slavin A.* Mutual phase-locking of two spin-torque oscillators: Influence of time delay of a coupling signal // Proceedings of the Europe International Magnetics Conference (Intermag 2008), Madrid, Spain, 2008. 33. *Prokopenko O., Verba R.* Broad-band regime of forced phase-locking of magnetization oscillations in spin-torque nanooscillators // Вісник Київського національного університету імені Тараса Шевченка. Серія: радіофізика та електроніка. – 2009. – № 12. 34. *Ralph D. C., Stiles M. D.* Spin Transfer Torques // Journal of Magnetism and Magnetic Materials. – 2008. – Vol. 320. 35. *Ramo S., Whinnery J. R., Duzer T. V.* Fields and Waves in Communication Electronics. – N.-Y., 1984. 36. *Rezende S. M., de Aguiar F. M., Azevedo A.* Spin-wave theory for the dynamics induced by direct currents in magnetic multilayers // Physical Review Letters. – 2005. – Vol. 94. 37. *Rippard W. H., Pufall M. R., Kaka S., Russek S .E., Silva T. J.,* Direct current induced dynamics in Co90Fe10 = Ni80Fe20 point contacts // Physical Review Letters. – 2004. – Vol. 92. 38. *Rippard W. H., Pufall M. R., Silva T. J.* Quantitative studies of spin-momentum-transfer-induced excitations in Co/Cu multilayer films using point-contact spectroscopy // Applied Physics Letters. – 2003. – Vol. 82, № 8. 39. *Rippard W. H., Pufall M. R., Kaka S., Silva T. J., Russek S. E.* Current-driven microwave dynamics in magnetic point contacts as a function of applied field angle // Physical Review B. – 2004. – Vol. 70. 40. *Ruotolo A., Cros V., Georges B., Dussaux A., Grollier J., Deranlot C., Guillemet R., Bouzehouane K., Fusil S., Fert A.* Phase-locking of magnetic vortices mediated by antivortices // Nature Nanotechnology. – 2009. – Vol. 4. 41. *Sankey J. C., Braganca P. M., Garcia A. G. F., Krivorotov I. N., Buhrman R. A., Ralph D. C.* Spin-transfer-driven ferromagnetic resonance of individual nanomagnets // Physical Review Letters. – 2006. – Vol. 96. 42. *Schafer S., Chumak A. V., Serga A. A., Melkov G. A., Hillebrands B.* Microwave spectral analysis by means of nonresonant parametric recovery of spin-waves signals in a thin magnetic film // Applied Physics Letters. – 2008. – Vol. 92. 43. *Slavin A. N., Kabos P.* Aproximate theory of microwave generation in a current-driven magnetic nanocontact magnetized in an arbitrary direction // IEEE Transaction on Magnetics. – 2005. – Vol. 41. 44. *Slavin A., Tiberkevich V.* Nonlinear auto-oscillator theory of microwave generation by spin-polarized current // IEEE Transaction on Magnetics. – 2009. – Vol. 45. 45. *Slonczewski J. C.* Current-driven excitation of magnetic multilayers // Journal of Magnetism and Magnetic Materials. – 1996. – Vol. 159. 46. *Slonczewski J. C.* Excitation of spin waves by an electric current // Journal of Magnetism and Magnetic Materials. – 1999. – Vol. 195. 47. *Tiberkevich V., Slavin A., Bankowski E., Gerhart G.* Phase-locking and frustration in an array of nonlinear spin-torque nano-oscillators // Applied Physics Letters. – 2009. – Vol. 95. 48. *Tulapurkar A. A., Suzuki Y., Fukushima A., Kubota H., Maehara H., Tsunekawa K., Djayaprawira D. D., Watanabe N., Yuasa S.* Spin-torque diode effect in magnetic tunnel junctions // Nature. – 2005. – Vol. 438. 49. *Vasyuchka V. I., Melkov G. A., Moiseienko V. A., Prokopenko A. V., Slavin A. N.* Correlation receiver of below-noise pulsed signals based on parametric interactions of spin waves in magnetic films // Journal of Magnetism and Magnetic Materials. – 2009. – Vol. 321, No. 20. 50. *Wang C., Cui Y.-T., Sun J. Z., Katine J. A., Buhrman R. A., Ralph D. C.* Sensitivity of spin-torque diodes for frequency tunable resonant microwave detection // Journal of Applied Physics. – 2009. – Vol. 106. 51. *Wickenden A. E., Fazi C., Huebschman B., Kaul R., Perrella A. C., Rippard W. H., Pufall M. R.* Spin torque nano-oscillators as potential terahertz (THz) communications devices // Report of U. S. Army Research Laboratory. – 2009. 52. *Yang Z., Zhang S., Li Y.C.* Chaotic dynamics of spin-valve oscillators // Physical Review Letters. – 2007. – Vol. 99.

Submitted 30.09.10

UDC 621.272.832.01

V. Sidorenko Ph. D.,
Yu. Gaidai Ph. D.,
P. Apalkovskiy stud.,
O. Sinkevich eng.

ACTIVE PROBE OF MODULATION TYPE IN MICROWAVE MICROSCOPY

Розроблено структурну схему ближньопольового мікрохвильового мікроскопа нового типу – з активним модуляційним зондом, яка принципово відрізняється від існуючих світових аналогів та розширює можливості в точності визначення діелектричних параметрів матеріалів. Експериментально отримані залежності перестройки резонансної частоти від магнітного поля. Підтверджено придатність феритової перестройки частоти резонатора в схемі мікроскопа з активним зондом модуляційного типу.

Ключові слова: ближньопольова мікроскопія, феритова перестройка частоти резонатора.

The block diagram of near-field microwave microscope of new type with the active modulation probe was developed, which essentially differs from existing world analogues and enhances the possibilities in accuracy of determination of dielectric parameters of materials. The dependences of resonant frequency tuning on a magnetic field are experimentally received. The suitability of ferrite of frequency tuning of the resonator in the scheme of a microscope with an active probe of modulation type is confirmed.

Keywords: near-field microscopy, ferrite frequency tuning of resonator.

The development of modern microwave microelectronics for space and cellular communication needs the appropriate instruments for quality control of advanced dielectric materials and their further development. It's important to do the control with the high-resolution and in that range of frequencies in which they will be used.

The traditional wave microscopy is unable to meet the demands of modern technology, because the diffraction effects limit the degree of focusing of rays and also the resolving power of devices in the size of the $\lambda/2$.

The scanning microwave near-field microscopy is one of the most perspective methods of research of dielectrics' parameters. The given method allows to measure locally the values of permeability (dielectric constant) with high sensitivity to $\Delta\varepsilon \sim 10^{-3}$. The spatial separative power of the near-field microscopes (both optical, and the microwave frequency (SHF) of ranges) doesn't depend on length of a wave and can reach $\delta \sim 1$ nm.

Our analysis of world developments of the near-field microscopy shows that in the overwhelming majority of microscopes are used the generators which tuning to frequency [1–6]. The instability of the analog generators introduces the additional errors in measuring of small displacements of maximum resonance line, which negatively influences the accuracy of measurements. The inaccuracy fixation of the bias of a maximum of the resonant characteristic of the resonator leads accordingly to the error in determining ε. For example, to register the change as $\Delta\varepsilon \sim 10^{-3}$ it's necessary with the accuracy to 10 kHz to record the frequency tuning of generator [1,3]. This fact indicates the need to use expensive and high- stable generators and impossibility of use of the majority of the home generators, which give the random deviation of sequence frequency 1–10 MHz.

We have proposed a fundamentally new scheme of the near-field microscope (Fig. 1), which has no analogues in the world. It does not need the smooth tuning of the generator because we used in it the relatively inexpensive high-stable generator with the fixed frequency - synthesizer. So, instead of tuning and the frequency modulation of the microwave generator relatively to the fixed frequency of resonator probe, which are in the world analogues, we suggested the opposite – to tune up and modulate the frequency of the resonator probe relative to the fixed frequency of the high-stable generator.

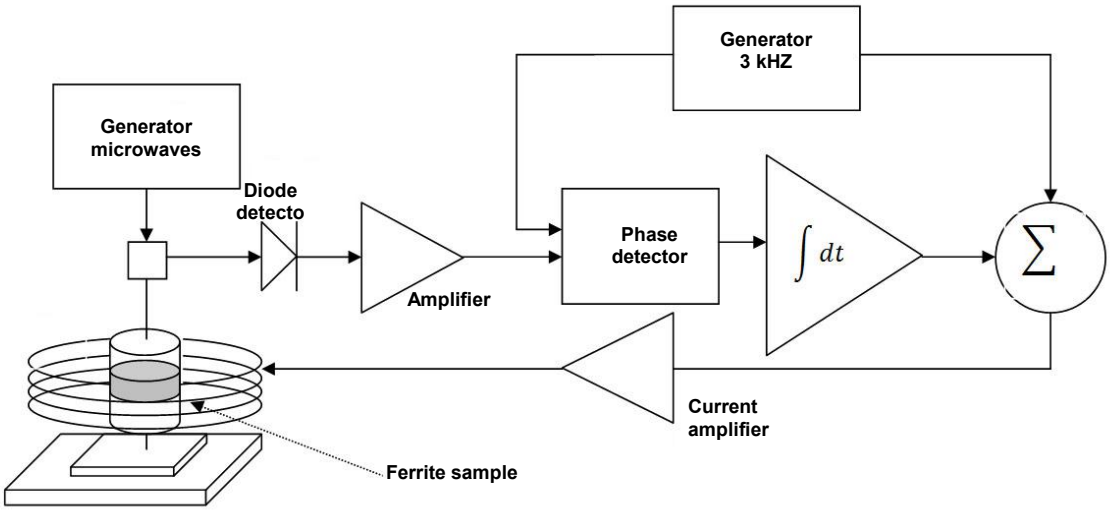

Fig. 1. Block diagram of the near-field microway microscope with the active probe of modulation type

The scheme works in following way. The signal of the synthesizer moves on a resonator of the probe, the resonance frequency is modulated by the signal 3 kHz, i. e. the signal, that is reflected from the microwave resonator, is amplitude-modulated with the frequency of 3 kHz. Using the directional coupler the reflected signal is moved on the diode detector and then the low-frequency signal is amplified and moved to phase detector where is compared with the reference signal modulation to a frequency of 3 kHz. The reference signal is summarized simultaneously with the constant voltage on the output of the integrator, proportionally to the bias of the central frequency of the resonance probe and moved to the power supply and further to the modulation coil, which creates an alternating magnetic field at the frequency of the reference signal. So far as the ferrite sample is placed in the resonator, it changes its parameters under the influence of the magnetic field μ, μ_a, so the resonant frequency of the probe is modulated with the frequency of 3 kHz.

The frequency of the generator can not coincide with the resonant frequency of a probe in the beginning of work of the scheme then in a signal from the microwave detector arises the component of a signal on the frequency of the first harmonic of a reference signal 3 kHz. Depending on a sign of mismatch this component will be in a phase or an antiphase to the reference signal (Fig. 2). Accordingly to this, the constant voltage that is proportionally to the size of mismatch will be change on an integrator exit.

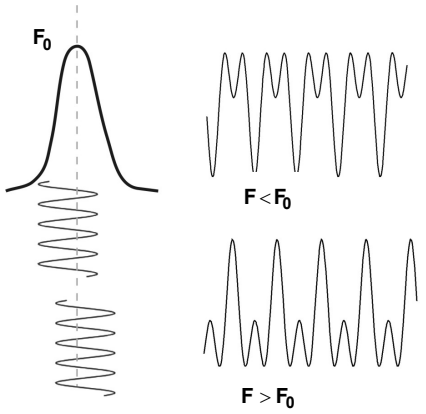

Fig. 2. The signal at the output of the phase detector by mismatch frequency band modulation probe relative to the frequency of the synthesizer

Proportionally to the constant voltage at the output of the integrator the central frequency band of the frequency modulation probe will be changed to the coincidence with the fixed frequency of the synthesizer. Then, due to symmetry in the spectrum of detected signal will be missing the first harmonic 3 kHz. Accordingly, there will be no the constant component to the output signal on the phase detector and the constant voltage will be fixed into an output of the integrator. The calibration process is completed at this step. Thus, the automatic tuning of the central frequency band of the frequency modulation probe is implemented on the frequency of the microwave generator.

If load the open end of the probe on the sample, that is investigated, then the resonant frequency and the good (high) quality of resonant probe will change The system automatically tunes the resonator frequency to a fixed frequency of the microwave generator. The integrator output voltage is fixed again, but at another level, the difference of this voltage with the calibrating one will be proportional to the local dielectric permeability of the measured sample, as a result of its scanning it's possible to construct a card of the distribution of its dielectric parameters.

The principal difference of this type of microscope is that during the operation of the scheme the generator of SHF does not change its frequency, and linear and modulation (per harmonic law) modulation of the resonance frequency of the probe is due to the ferrite probe placed in the resonator. So we do not change the frequency of the generator, but we shift and modulate the resonance frequency of the probe.

To calculate the shift of resonant frequency of the active modulation probe with the ferrite from an external magnetic field we use the known ratio of the theory perturbation:

$$\frac{\omega-\omega_0}{\omega}=\frac{\int_{V1}\left((\dot{\mathbf{E}}_0^*(\varepsilon-\varepsilon_0)\dot{\mathbf{E}}+\dot{\mathbf{H}}_0^*(\bar{\mu}-\mu_0)\dot{\mathbf{H}}\right)dV}{2W_0}, \qquad (1)$$

where $W_0=\frac{1}{2}\int_V(\varepsilon\dot{\mathbf{E}}\dot{\mathbf{E}}_0^*+\mu_0\dot{\mathbf{H}}\dot{\mathbf{H}}_0^*)dV$ – energy, stored in non perturbation resonator [7].

For the coaxial λ/4 resonator without filling and cover S, which is an ideal conductor, its sizes are selected so that only TEM wave is propagated.

The field distribution in the given resonator looks like:

$$\dot{\mathbf{E}}_0=-\frac{p\pi}{l}\dot{\mathbf{A}}\frac{1}{r}\sin\frac{p\pi}{2l}z,$$

$\dot{\mathbf{H}}=-\frac{ip\pi}{Z_0 l}\frac{1}{r}\cos\frac{p\pi}{2l}z$, where l – length of the resonator, Z_0 – wave resistance, p – quantity of half-waves, that are insert in the length of the resonator l [8].

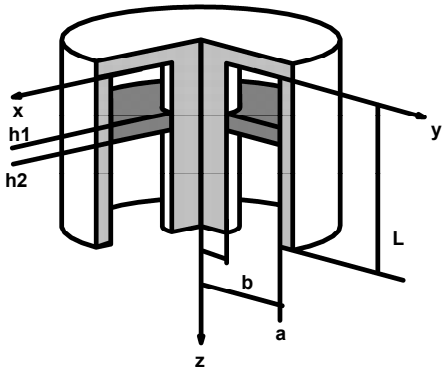

Fig. 3. Coaxial λ/4 resonator with the ferrite disk

If the ferrite has the form of a thin disk magnetized perpendicular to its plane (see Fig. 3), the tensor components of the demagnetizing factor will have the following values:

$$N_x=0,\quad N_y=0,\quad N_z=4\pi$$

Accordingly to this, the perturbed field will be of the form:

$$\mathbf{H}_\perp=\mathbf{H}_{\perp 0};\quad \mathbf{H}_z=\frac{\mu}{\mu_0}\mathbf{H}_{Z0},$$

where $\mathbf{H}_\perp=\mathbf{x}_0H_x+\mathbf{y}_0H_y$, a $\mathbf{x}_0$, $\mathbf{y}_0$, $\mathbf{z}_0$ – unit vectors in the direction of the respective axes [12].

Substituting the values of perturbed and unperturbed fields in (1) and integrated the integral in the numerator by the volume of ferrite, and the integral in the denominator by the volume of the resonator we have:

$$\frac{\omega-\omega_0}{\omega}=\frac{A(\varepsilon-\varepsilon_0)}{\pi\varepsilon_0 l}-\frac{B(\mu-\mu_0)}{Z_0\pi\varepsilon_0 l},\ \text{де}$$

$$A=\left(\sin(\frac{\pi h_1}{l})-\sin(\frac{\pi h_2}{l})+\frac{\pi(h_2-h_1)}{l}\right)$$

$B=\left(\sin(\frac{\pi h_1}{l})-\sin(\frac{\pi h_2}{l})+\frac{\pi(h_1-h_2)}{l}\right)$ – coefficients that characterize the position and size of ferrite washer.

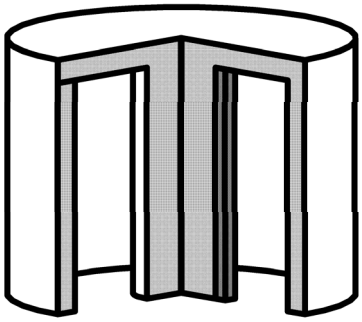

Fig. 4. Coaxial λ/4 resonator with the longitudinal ferrite core placed near the central core

Similarly calculate the shift of resonant frequency for ferrite, which has the form of thin cylinder magnetized along its axis (see Fig. 4), then the tensor components of the demagnetizing factor will have the following values:

$$N_x = 2\pi, \quad \boldsymbol{N_y = 2\pi}, \quad N_z = 0 .$$

Accordingly to this, the perturbed field will be of the form:

$$\mathbf{H}_\perp = \frac{2\mu_0(\mu+\mu_0)}{(\mu+\mu_0)^2-\mu_a^2}\mathbf{H}_{\perp 0} + \frac{2i\mu_0\mu_a}{(\mu+\mu_0)^2-\mu_a^2}\mathbf{z}_0 \times \mathbf{H}_{\perp 0}$$

$$H_z = H_{0z}$$

Substituting the values of perturbed and unperturbed fields in (1) and integrated the integral in the numerator by the volume of ferrite, and the integral in the denominator by the volume of the resonator we have:

$$\frac{\omega-\omega_0}{\omega} = A\left(\frac{2\mu_0(\mu^2+\mu_0^2-\mu_a^2)}{(\mu+\mu_0)^2-\mu_a^2} + \frac{2\varepsilon_0(\varepsilon-\varepsilon_0}{\varepsilon+\varepsilon_0}\right)$$

where the coefficient A characterizes the position and size of ferrite sampler.

For the experimental research of resonant frequency shift of the probe the scheme of panoramic measuring instrument VSWR was collected (see Fig. 5), which works accordingly the method of the isolated extraction of the incident and the reflected waves using the directional couplers. We used in our research: standing wave ratio meter (SWR meter) and reduction "Я2Р-67", sweep generator, the probe on the basis of λ/4 resonator with the modulation coil.

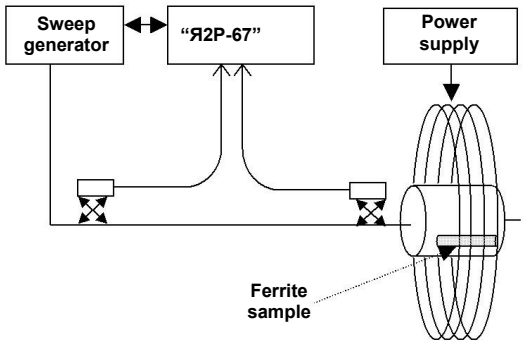

Fig. 5. Block diagram of the measuring apparatus

It has been found experimentally the dependence of the resonance frequency's shift of the probe from the current strength, given to the coil (an external constant magnetic field) at different locations and different marks of ferrites.

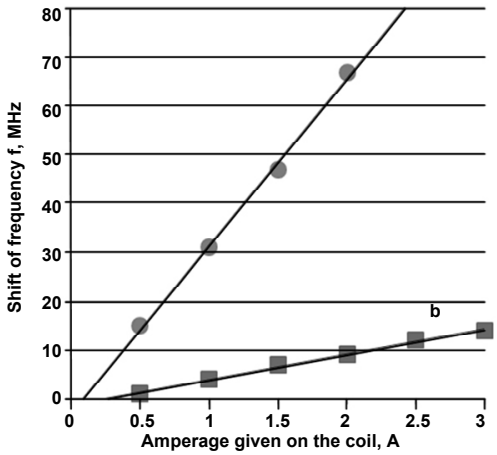

**Fig. 6. The dependence of shift of the resonant frequency of the probe at the amperage given on the coil for different disposition of ferrites:
a) ferrite core (10СЧ-8) near the central filament of the resonator,
b) ferrite core (10СЧ-8) near the wall of the resonator**

Comparing the size shift of the resonant frequency (Fig. 6) at the location of the ferrite core in position near the central filament (a) and near the wall of the resonator (b) it's easy to see that the shift is more pronounced when the ferrite is closer to the center. This is due to the fact that the magnetic field in the coaxial resonator in the direction from the central filament to the walls of a cavity decreases in proportion to 1/r.

The ferrite location in the position (b) requires a greater intensity of modulating magnetic field to obtain the same resonance frequency shifts of the probe and, therefore, to use bigger currents in the coil and consequently to unnecessary losses. Therefore, the further researches were conducted with the ferrite location near the central filament of the resonator.

Having compared dependences for one (a) and two identical samples (b) (Fig. 7), placed in the resonator, we see that at identical currents the resonant frequency in the second case shifts in almost twice as much, and it shows the possibility of summation of the contribution to shift of resonant frequency of two various samples placed in one resonator. However, the losses are also added that leads to faster reduction of good quality of the resonator, and accordingly to the narrower strip of reorganization of the resonator without changing of its good quality.

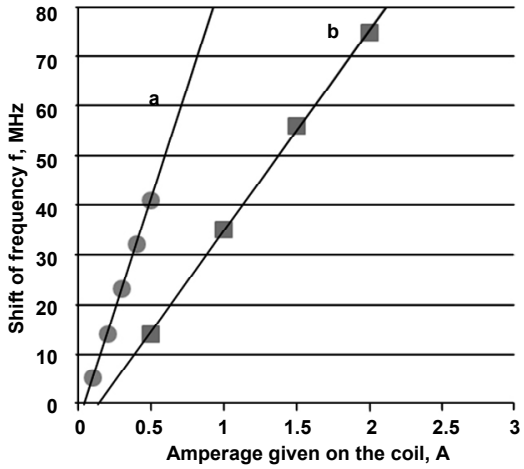

**Fig. 7. The dependence of shift of the resonant frequency of the probe at the amperage given on the coil for different disposition of ferrites:
a) three ferrite cores (40СЧ-2) near the central filament of the resonator,
b) two ferrite cores (10СЧ-8) near the central filamentl of the resonator**

In all four cases it's accurately traced the tendency of change of resonant frequency of a probe is depending on an external magnetic field. There is some nonlinearity on the beginning of the dependence, however starting from small values of current (0.5 A) we observe a linear change of resonant frequency.

It's evident from the presented graphs, that it is possible to realize a linear shift in resonance frequency of the ferrite $\Delta f \sim 70$ MHz, and the resonator quality factor remains almost unchanged. This is quite enough to realize the idea of the near-field microscope with an active probe of the modulation type.

Thus, there was proposed the near-field microwave microscope of new type with the active modulation probe. It essentially differs from the existing world analogues because it gives the possibility to use instead of expensive high-stable analogue generators relatively cheap fixed-frequency synthesizers, therefore the microscope is more accurate and cheaper.

We investigated the tuning of the resonator frequency by ferrite under the influence of an external constant magnetic field.

The system of modulation of resonant frequency of a probe is calculated and made, it provides the necessary uniformity of a magnetic field.

It has been found experimentally that the bandwidth of the linear tuning of the resonator with ferrite frequency can be $\Delta f \sim 70$ MHz without the noticeable losses in quality factor of the resonator. Since the width of the resonance curve of the probe was 14 MHz, and the shift of frequency when approach to the needle of probe a dielectric with $\varepsilon = 100$ is 10 MHz, then the width of the tuning of probe frequency received by us is sufficient for the linear compensation of the displacement of the resonance curve due to approach to the needle of probe a measuring dielectric.

1. *Steinhauer D. E., Vlahacos C. P., Wellstood F. C.* // Rev. Sci. Instrum. – 2001. – V. 71, No 7. 2. *Gao C., Xiang X.-D. Rev. Sci.* Instrum., November 1998. – V. 69, No 11. 3. *Гайдай Ю. О., Сидоренко В. С., Сінькевич О. В.* Ближньопольовий мікроскоп для дослідження дисперсії діелектричної проникності. // Вісник Київського національного університету ім. Т. Шевченка Радіофізика та Електроніка. – 2008. – №.11, – С. 16–18. 4. *Гайдай Ю. О., Сидоренко В. С., Сінькевич В. О.* Ближньопольовий мікрохвильовий мікроскоп з активним зондом. // Вісник КНУ Радіофізика та Електроніка. – 2006. № 9, – С. 19–21. 5. *Сидоренко В. С., Гайдай Ю. О., Сінькевич О. В., Жила С. В.* Пристрій для ближньопольової мікроскопії діелектричних об'єкті. Державний патент інтелектуальної власності. - Бюл № 10, 15.10.2003 р. Патент за заяв. № 2002119038. 6. *Danilov V. V, Sidorenko V. S., Gaidai Yu. A., Sinkevich O. V*. Near-filed microwave microscope based on the annular generator. // Third international yang scientists' conference on applied physics, Kyiv, 2003. – p. 105–106. 7. *Гуревич А. Г.* Ферриты на сверхвысоких частотах. – М., 1960. 8. *Григорьев А. Д.* Электродинамика и техника СВЧ. – М., 1990.

Submitted 20.11.10

UDC 53.082.7, 534.2

D. Sinchuk, stud.,
S. Radchenko, Ph. D.

THE ULTRASONIC BACKSCATTERING IMITATION IN BIOLOGICAL TISSUES UNDER FLUCTUATIONS OF THEIR BULK MODULE

Різні типи тканини при ультразвуковому зондування можуть бути описані як відповідні набори розсіювачів. Сигнал відлуння, сформований розсіювачами з різними властивостями, підкоряється статистиці з різними функціями густини імовірності огинаючої. Основну увагу у роботі приділено впливу флуктуаційних змін об'ємного модуля стиснення м'яких біологічних тканин при ехо-імпульсному режимі сканування. Формування сигналу відгуку розглядається у рамках моделі тканини як набору дискретних розсіювачів із випадковими змінами характеристик. На основі загальних фізичних принципів розсіяння аналітично отримано функцію відгуку від системи обраних неоднорідностей із змінами об'ємного модуля стиснення, густини, положення та розмірів. Отримані в результаті моделювання оцінки функції густини розподілу амплітуди сигналу відгуку свідчать про значний вплив невеликих локальних флуктуацій об'ємного модуля стиснення на амплітуду сигналу відлуння.

Ключові слова: розсіяння ультразвуку, біологічна тканина, флуктуації об'ємного модуля стиснення, стохастична неоднорідність.

Different types of tissue at ultrasonic ranging can be represented as corresponding sets of scatterers. Echo signal formed by scatterers wih different properties conforms to statistics with different probability density functions of the envelope. The main attention is paid to the influence of bulk module fluctuation in soft biological tissues under echo-pulse scanning. Formation of response signal is considered within the tissue model as a set of discrete scatterers with random changes of their characteristics. The response function from the system of mentioned above inhomogeneities with fluctuation of bulk module, density, position and size are analytically obtained based on general physical principles of scattering. The resulting simulation estimation of probability density function of response signal amplitude shows significant effect of small local fluctuations of the bulk module on the echo signal amplitude.

Key words: ultrasonic scattering, biological tissue, bulk module fluctuation, stochastic inhomogeneity.

Introduction. Nowadays a great attention is paid to the development of medicine and health monitoring. More and more methods are implemented to prevent various diseases. To reveal pathology at early stages of the disease is one of the important problems of modern medicine. The earlier we can set a deviation from the norm, so we can easily and effectively cure the patient. Modern technological advances have given impetus to the rapid development of medical equipment of various types and purposes. With the advent of the first installations of live tissue visualization, there appeared the problem of processing data for setting the parameters of the investigated objects and restore their internal structure.

Solution of the problem is based on the study of physical processes, mathematical models elaboration of biological tissues and development of the correct reconstruction algorithms of measured data on their basis. The accuracy of diagnosis is the key to successful treatment. So now the reconstruction accuracy of the measuring signal remains an acute problem. Reconstruction algorithms for magnetic resonance, X-ray computed tomography techniques, or ultrasound introscopy (USI) are built on a model that describes the influence of measured signal parameters on object chacracteristics. For USI this is a restoration of location and impedance characteristics of the environment with acoustic echo signal. Based on comparison of received signal parameters and the parameters of object the reconstruction algorithm is built. Therefore, accurate records of tasks, respectively, determines the accuracy of building backward algorithm that consistently affects the quality of the received image. Therefore it is urgent to develop new methods of solving problems of reconstruction, which is a way to improve visual image.

The main characteristic that determines the scattering of ultrasound (US) waves on the inhomogeneities is a ratio of the specific acoustic environment impedances in which this wave propagates and inhomogeneity [1]. This ratio depends on the change of density ρ and bulk module of matter G at the boundary separating media. The difference in the density of soft biological tissues with and without minor pathology is little – these changes in absolute value do not exceed 10 %, while the bulk module changes can reach tens times [2].

The discrete scatterers models are well describing the formation of backscattered component of the field in the pulse-echo scan [3, 4]. But there is difficulty to use ones for description of impact of tissue characteristics fluctuations on the ultrasound images formation due to idealization embedded in the models. Hence statistical characteristics of the scattered field amplitude are obtained when inhomogeneity is little and its impedance cancellation of non-scatterring environment is significant and fixed.

Therefore, the amplitude of acoustic wave scattered from the inhomogeneity depends on average on its size and acoustic impedance, i. e. on its change of relative acoustic impedance. Additionally, the impulse characteristic of biological tissue at the back scattering is exactly unknown, although various models of sound scattering are developed [2–6].

Simplifications and generalizations used in these models restrict areas of their adequacy and do not allow the application of theoretical approaches outside them. So the question remains actual in creation of a relevant echo model, which would have changes of bulk modulus of compressibility inhomogeneity as one of its impact parameters. This paper is an attempt to describe the impact of fluctuations compressibility of soft biological tissues on the characteristics of the echo signal at backscatterring on the basis of a universal approach to the inhomogeneity of the echo signal.

Theoretical basis for description of response signal from inhomogeneity. In general, the signal response of inhomogeneity according to spatial location in Fig. 1 can be described as a convolution of three functions:

$$p_r\left(\vec{r_2}, t\right) = v_{pe}(t) \underset{t}{\otimes} f_m\left(\vec{r_1}\right) \underset{r}{\otimes} h_{pe}\left(\vec{r_1}, \vec{r_2}, t\right)$$

where sign $\otimes$ denotes convolution operator. $p\left(\vec{r}, t\right)$ is a response or echo signal function. v_{pe} is our exciting pulse, which includes sensor excitation and electromechanical impulse response during emitting and receiving of the wave packet. Function f_m describes the medium inhomogeneity. Particularly it contains contribution of the density variation and velocity distribution to the scattered signal. Term h_{pe} is modified spatial impulse response that covers the sensor or ultrasound transducer geometry and spatial framework of the scattered field [2–3].

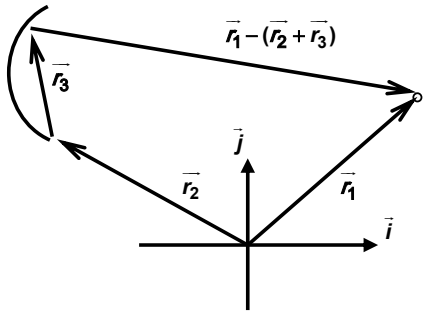

Fig. 1. General scheme of scatterers $\vec{r_1}$ and the source of ultrasonic waves $\vec{r_2}$ location. $\vec{i}$, $\vec{j}$ are unit basis vectors in space and make up coordinate system to describe the scattered field

Vector $\vec{r_3}$ in Fig. 1 and Fig. 2 considers the sensor stretch, which leads to the time delay of echo signal arrival time at the different transducer points.

For rectangular exciting pulse [3]:

$$v_{pe} = A \cdot H(z - t \otimes c) H(t \otimes c + a - z) \cdot \exp\left(i(\omega t - kr)\right)$$

For small spherical inhomogeneity [3]:

$$f_m(z) = -\frac{\pi k^4 r_d^2}{18}\left(\frac{G_e - G}{G} - \frac{3\rho_e - 3\rho}{2\rho_e + \rho}\right)^2 r_n^4 \cdot \delta(z - z_0)$$

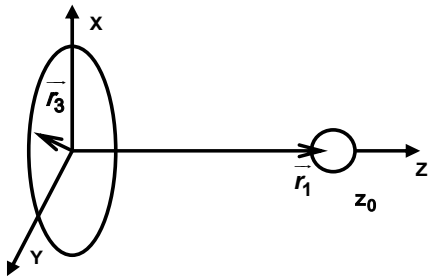

Fig. 2. General spatial scheme of scatterer location

Based on representations of scattering there are obtained analytical dependence of echo signal function of spatially heterogeneous environment where diversity is characterized by compression bulk modulus, density, size and location. Diffusers are located on the symmetry axis of the system. Ultrasonic wave transmitter is plane.

Within this model the response of the system of various scatterers that are uniformly placed on the length of sampling, in which bulk module fluctuates and are randomly set is investigated.

$$P_s(t) = \sum_{k=1}^{N} P_z\left(t - \frac{2z_k}{\nu}, z_k, G_{z_k}\right).$$

$P_s(t)$ is total echo signal from scatterers set. $P_z(t, z_0, G_z)$ is echo signal function of single scatterer, which depends on the scatterer coordinate and bulk modulus, z is coordinate vector of scatterer, G_z is value of bulk modulus, N is number of scatterers in the set, in other words N different sum components with pair of own values of vector z and bulk module G_z.

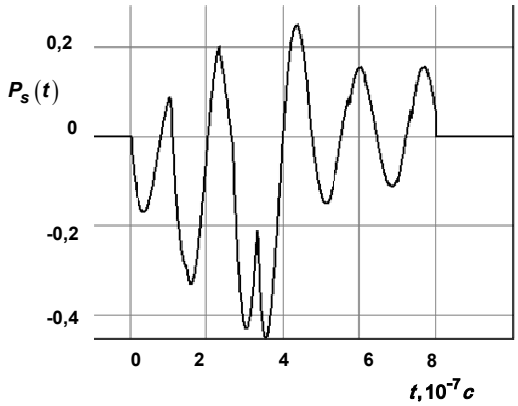

Fig. 3. Oscillogram of scatterers system echo signal measured as the overpressure amplitude (scatterer number N in the set equals to 8). Overpressure time dependence $P_s(t)$ is represented in units relative to excitation pulse amplitude

Mathematical modeling of the echo signal at fluctuations of the bulk modulus. Ultrasound imaging represents a signal from the tissue as the envelope maximum [7] fixed by ultrasonic transducer. Therefore the statistics of amplitude maximum of the echo signal envelope at 1000 items sampling with the scatterers number range from 1 till 10 [6] has been obtained. The average amplitude of the echo signal for different number of scatterers were also calculated. Dependence of envelope maximum value was approximated by the third order polynom of the scatteres number according to minimization of standard deviation between measured and approximated values (Fig. 4).

The polynomial parameters for the curve displayed in Fig. 4 is represented in Table 1.

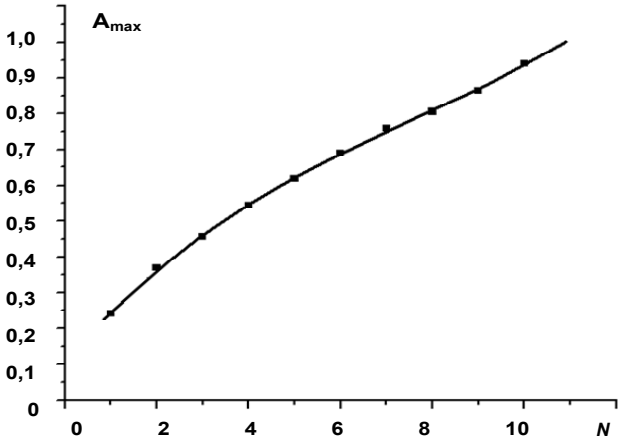

Fig. 4. Dependence curve of the average maximum value of envelope amplitude A_{max} in relative units calculated for the scatterers number N

Polynomial regression equation is

$$Y = A + B_1 \cdot X + B_2 \cdot X^2 + B_3 \cdot X^3 .$$

Thus, the result shows that the scatterers number nonlinearly increases average value of maximum amplitude.

There are strong fluctuations of the differential scattering cross-section in resolution element. Density distribution function (DDF) of the envelope amplitude does not match the case of Rayleigth statistics [3]. The effective number of scatterers $M = N(\nu + 1)$ and variation of their scattering cross sections b are used to describe the deviation from Rayleigth statistics. The statistical parameter of DDF M is defined as the actual number of scatterers N, and size distribution asymmetry of scatterers. ν Parameter b takes into account the variation of their scattering cross sections a by way of $b = 2\sqrt{(\nu+1)/\langle a^2 \rangle}$ [4].

Table 1. **Polynomial coefficients value.**

Parameters		
Symbol	**Magnitude**	**Error**
A	1,1	0,1
B_1	1,5	0,1
B_2	-0,12	0,02
B_3	0,005	0,001

The value of M and b are parameters of the probability density function of echo signal envelope from the scatterers system. They completely represent scattering property of inhomogeneous medium. It was chosen to characterize the soft tissue [8].

Recovery of M and b values are done by estimations of distribution moments. Based on the obtained data of the envelope amplitude the parameters M, b and ν were calculated as $b = 2\Gamma(1{,}5)/E\{A\} \cdot \Gamma(M + 0{,}5)/\Gamma(M)$, where $\Gamma(\cdot)$ is the gamma function, $E\{A^n\}$ – is the statistical moment of n order.

The values of variable M was found independently. It is used equation based on property of DDF envelope amplitude for ultrasound echo in the range of K-model [4].

$$M = 2/(r_4 - 2)$$

where r_4 is the second order and the fourth order moment ratio as follow $r_{2m} = E\{A^{2m}\}/\left(E\{A^2\}\right)^m$.

Table 2. **Estimated value of the scatterers effective number M, inverse scattering cross-section b and size distribution asymmetry ν according to scatterers number N of system**

N	M	b	ν
1	0,2	0,24	-0,76
2	0,8	0,39	-0,59
3	1,4	0,41	-0,54
4	3,6	0,61	-0,10
5	0,8	0,22	-0,84
6	8,3	0,73	0,39
7	19,1	0,99	1,73
8	9,1	0,65	0,13
9	17,7	0,87	0,96
10	2,9	0,31	-0,71

It should be noted that bulk module fluctuations of heterogeneities compressibility have a significant impact on the effective number of scatterers in the cell of resolution at ultrasound scanning [6] that is shown in Table 2.

The evaluation of the amplitude DDF. DDF of the amplitude according point scatterers model is described by the two-parameter distribution [4].

$$f(a) = [2b/\Gamma(\nu+1)](ba/2)^{\nu+1} K_\nu(ba),$$

where $K_\nu(\cdot)$ is the modified Bessel function of ν order. Parameter ν denotes asymmetry of scatterers distribution.

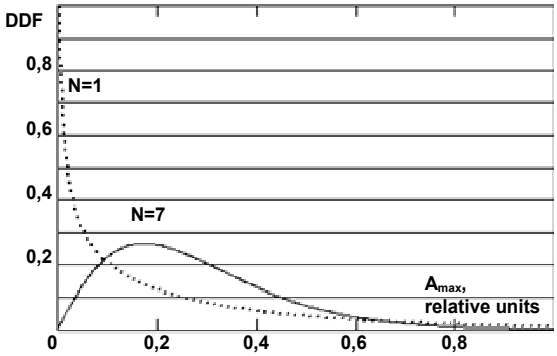

Fig. 5. DDF of echo signal amplitude for different set of scatterers (for boundary value of number is one and seven)

Conclusions. Expression of the envelope amplitude for ultrasound echo in an inhomogeneous medium has been derived under the assumption of small number of scatterers with fluctuation of bulk module, density, position and size.

A general expression was derived for the received amplitude of overpressure field using the discrete scatterers model are well describing the formation of backscattered component of the field in the pulse-echo scan. The model can be applied to different transducer types and excitations pulse forms.

The derived expression takes into account scatterers position, bulk module, density and size fluctuation. They are the parameters that should be displayed in medical ultrasound images, but we observe a temporally and spatially averaged version of the tissue differences. Therefore the dependence of maximum amplitude of scattering echo signal on distribution characteristics of the scatterers are obtained using statistical evaluation method.

Based on these estimates significant effect bulk module fluctuation on the echo signal amplitude is shown. The average amplitude dependence of scattered signal on the number of scatterers is also found. The obtained amplitude density functions of echo signal distribution depending on the number of scatterers are the basis of tissue identification by ultrasound introscopis images analysis.

1. The Physics of Medical Imaging. / Edited by S. Webb. – IOP Publishing Ltd. – 1991, 640 p. 2. *Duck F. A.* Physical properties of tissue: A comprehensive reference book. // London, San Diego, N.-Y., Boston: Academic Press, 1990. 346 p. 3. *Jensen J. A* model of propagation and scattering of ultrasound in tissue // J. Acoust. Soc. Am. – 1991. – Vol. 89, p. 182–190. 4. *Shankar P.* A model for ultrasonic scattering from tissues based on the K distibution // Phys. Med. Biol. – 1995. – Vol. 40. 5. *Shankar P.* Use of the K-distribution for classification of breast masses // Ultrasound in Med. & Biol. – 2000. – Vol. 26. 6. *Oelze M. L., Zachary J. F., O'Brien W. D.* Characterization of tissue microstructure using ultrasonic backscatter: Theory and technique for optimization using a Gaussian form factor // J. Acoust. Soc. Am. – 2002. – Vol. 112, Is. 3, p. 1202–1211. 7. *Shankar P. M., Dumane V. A.* Classification of breast masses in ultrasonic B-mode images using a compounding technique in the Nakagami distribution domain // Ultrasound in Med. & Biol. – 2002. – Vol. 28. 8. *Sinchuk D., Radchenko S.* The influence of the soft biological tissue bulk modulus statistical changes on pulse-echo response characteristic. Proc. of the 10-th international young scientists conference on applied physics: Kyiv, June, 16–19, 2010, Ukraine, p. 142–143.

Submited on 29.09.2010

UDC 535.621.3

A. Shchyrba Stud.
A. Goriachko Ph. D.
P. Melnik Ph. D.
M. Nakhodkin Dr. Sci.

EXPERIMENTAL INVESTIGATIONS OF BI-NANOSTRUCTURES ON THE GE-SURFACE VIA SCANNING TUNNELING MICROSCOPY

В даній роботі було досліджено процес формування та росту тонких плівок вісмуту на підкладинці Ge(111) - 2 x 8. До 0.25 МШ, прогрів при 450 К спричиняє дифузію вісмутових атомів по поверхні та відповідно – формування острівців. Атоми вісмуту, адсорбовані на поверхні германію, формують маленькі острівці, густина яких зростає по мірі збільшення Ві покриття. За товщини вісмутової плівки порядку 1.5 МШ спостерігалось утворення 3-вимірних кластерів. Таким чином, за кімнатної температури вісмутова плівка росте з деякими відхиленнями від пошарового режиму росту. При подальшому вирощуванні плівки до товщин порядку від 7 до 10 МШ та подальшому прогріві до 450 К утворюються нанокристали вісмуту з орієнтацією поверхні типу (110).

Ключові слова: Германій, Вісмут, тонкі плівки, наноструктури, скануюча тунельна мікроскопія.

In this work, we have investigated the growth process of thin Bi-films on the Ge(111)-2x8 substrate. Below 0.25 ML, annealing at 450K causes diffusion of Bi atoms into dense Bi islands but no long-range order is established. Bi atoms adsorbed on top of germanium are forming small islands, their density increasing as metal coverage grows. Three-dimensional (3D) clusters were observed, starting with Bi-film thickness of about 1.5 ML. At room temperature, bismuth is growing with certain deviations from layer by layer regime. Larger Bi coverages (from 7 to 10 ML) deposited on Ge(111) and annealed at 450 K produce nanocrystalls with Bi(110) surface exposed on top of them.

Key words: Germanium, Bismuth, thin films, nanostructures, scanning tunneling microscopy.

Introduction. Thin Bi films are attracting attention due to substantial difference between their bulk and surface electronic properties. The bulk Bi is a semi-metal, but its surfaces can be metallic and show interesting spin-orbit effects [4]. A single monolayer film would represent the "ultimate" bismuth surface, but it would require a substrate to be placed on. In case of semiconductor substrates, this holds promise for "on-chip" integration of spintronic devices, creation of δ-doping layers, modelling of surfactant-mediated growth of heterostructures, etc.

Recently, a strong Rashba-type spin orbit splitting was observed at 1ML-($\sqrt{3} \times \sqrt{3}$)-Bi/Ge(111) interface [2]. Bi on Ge(111) was initially studied by low energy electron diffraction, where a $\sqrt{3} \times \sqrt{3}$ periodicity was detected at the coverage of 1/3 monolayer (ML) [9]. Recently, this structure was studied in detail by core level photoelectron spectroscopy [4]. These experimental studies are found to agree with a theoretical investigation of θ_{Bi} = 1/3 ML, T4 monomer phase [1], which also predicts another $\sqrt{3} \times \sqrt{3}$ structure to be a stable one: θ_{Bi} = 1 ML, T4 trimer phase. The latter structure was recently observed with STM [8], confirming the existence of trimers by means of atomic resolution imaging. However, there exists only scarce information concerning a detailed growth mode of such thin films [3].

Thicker Bi-films were a subject of investigation with low-index Bi surfaces such as (100), (110) and (111) as a target. Bi(100) stands out among other ones because some of the metallic surface states penetrate very deeply into the bulk crystal, down to about 20 layers. For the Bi(110), surface states are rather localized in the surface region and for Bi(111) they are strongly localized in the two topmost layers. The (111) unit cell is hexagonal, (110) – pseudosquare, (100) – quasi-hexagonal. As was pointed out in [2], the film's surface changes its orientation from (110) to (111) at 6–10 ML coverage range.

This warrants a wider investigation using real-space techniques, and therefore, we present a systematic scanning tunneling microscopy (STM)investigation of 0.1 up to 10 ML Bi films on Ge(111)-2 × 8.

Experimental. Our investigations were carried out in ultra-high vacuum (UHV) system with base pressure of 2×10^{-10} mbar, equipped with home-built STM [7], Auger electron spectrometer (AES), facilities for sample annealing, ion bombardment and bismuth deposition. A standard Ge(111) substrate preparation procedure consisted of numerous cycles of 500 eV Ar^+ bombardment at room temperature (RT) and annealing at 900 K. A drop of bismuth was placed on a curved tungsten wire and evaporated by means of direct current heating. In accordance with a generally accepted convention, we define 1 ML (monolayer) of deposited species as the density of atoms on the unreconstructed Ge(111) surface (7.22×10^{14} atoms/cm^2). The amount of adsorbed bismuth was controlled by a quartz micro-balance and AES measurements. The latter also confirmed the absence of any contamination both on clean and Bi-covered Ge(111) surface. STM images were obtained in constant current mode (typical tunneling current 0.3 nA). Probe tips were made of Pt-Ir wire (80 % Pt, 20 % Ir) by means of simple mechanical cutting. The tip conditioning consisted of electron bombardment in UHV with 2.5 kV voltage applied between the tip and the cathode. The last part of experiment consist of STM-investigating of annealed sample, 7 and 10 ML Bi-films, at 450 K.

Results. In fig. 1 we present series of STM images (125 nm × 125nm) with ever increasing Bi coverage on top of Ge(111) -2 × 8. Fig. 1a shows the pure substrate before deposition. One can see individual atomically flat terraces separated by single atomic height steps. Images 1b-f demonstrate sub-monolayer Bi growth at room temperature: 0.05 ML, 0.1 ML and 0.5 ML correspondingly. Here, from (fig. 1b, c, d, e, f) Bi atoms adsorbed on top of germanium are forming small islands, their density increasing as metal coverage grows. Within the 1 ML film (fig. 1e) bright spots amidst the terraces are clearly visible, indicating the second layer nucleation. At the same time, the terraces do not appear completely uniform but with some depressions still present. The second layer nucleation sites increase in density as the film growth up to 1.5 ML (figs. 1f). A careful analysis (see below) shows that three-dimensional (3D) clusters are already present in figs. 1f. Thus, we conclude about a deviation from the ideal layer-by-layer growth mode of Bi on Ge(111) - 2 × 8 at RT in the thickness range around 1 ML. A formation of Bi nano-objects is observed while increasing Bi coverage from 7 to 10 ML. Such tendency develops when some Bi islands begin to unite with each other (fig. 1). Also, the objects are becoming more structured, wich is caused by strong Bi/Ge interaction, and creating of islands wich cover more area of Ge-substrate. The size of such objects increase from 5 to 50 nm with increasing of the Bi quantity.

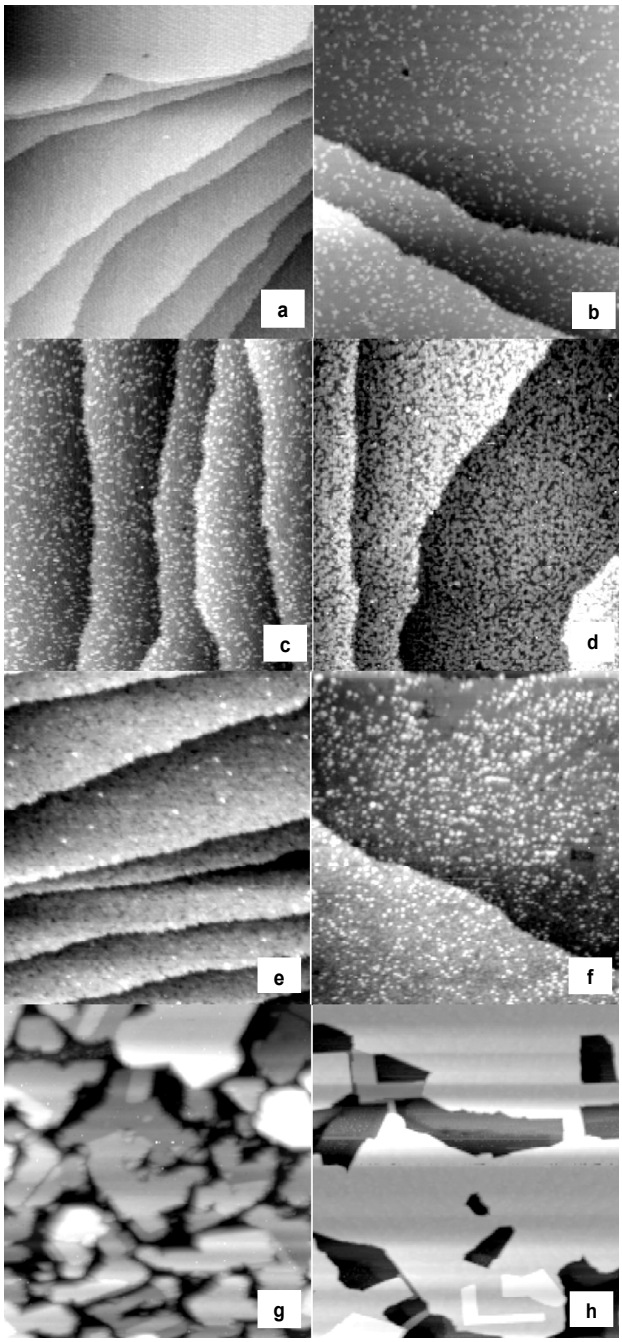

Fig. 1. STM images 125 nm × 125 nm of the Ge(111) – 2 × 8 substrate and ultrathin Bi films deposited at 300 K: a) pure Ge(111) – 2 × 8, Usample = 2.0 V; b) 0.05 ML, Usample = -2.0 V; c) 0.1 ML, Usample = 2.0 V; d) 0.5 ML, Usample = -3.0 V.; e) 1 ML, Usample = 2.0 V; f) 1.5 ML, Usample = 2.5 V; g) 7 ML, Usample = 0.5 V; h) 10 ML, Usample = 2 V

Fig. 2 shows STM images obtained after bismuth deposition on Ge(111) – 2 × 8 at RT and subsequent annealing at 450 K. The latter causes a coalescence of bismuth islands into larger ones. Increasing Bi coverage leads to larger island sizes (figs. 2a). Further, the substrate area covered by bismuth is roughly equal to uncovered substrate in fig. 2b (0.5 ML), and almost a continuous film is observed in fig. 2c (1 ML). As expected, the second layer species are more abundant at 1.5 ML (fig. 2d).

Finally, we follow the room temperature growth of Bi in the range from 0.5 to 1.5 ML in high resolution STM images. At 1 ML coverage the first layer is still not continuous and the second layer species are more abundant. Also, a lot of small patches, consisting of parallel stripes, are visible within the first layer. These stripes are very similar to a 2 × 1 zig-zag chain structure formed by 1ML Sb on Ge(111) [6]. At 1.5 ML the area occupied by the second layer of the growing film, as well as the number of 3D clusters are larger.

Images in fig. 2(a-h), were taken after the samples with deposited Bi were annealed at 450 K. At 0.5 ML coverage, one observes the germanium substrate partially covered by bismuth islands. On top of the first layer, three dimensional clusters are clearly seen. This stands in line with the earlier STM observation of 1 ML Bi on Ge(111) [8].

We measured step-height from STM-observation of 10 ML Bi-films (fig. 2g,h). This value is about 0.333 nm, wich corresponds to (110)-structure step-height. At the same time a theoretical value of interlayer distance of bulk Bi is about 0.328 nm.

Discussion. The low coverage segment of our data (figs. 1b, 2a) needs to be compared with the investigations of Wan et al [9] and Kuzmin et al [5]. Both groups deposited up to 2 ML of bismuth either onto a substrate at 600 K or performing a postdeposition annealing at the same temperature. The excess bismuth was desorbed from the substrate and the long-range order was established within the remaining adsorbate layer. In our work, annealing at 450 K is enough to activate diffusion of bismuth on top of Ge(111) - 2 × 8, but not to desorb it. The latter fact was verified by the unchanged $Bi(N_{6,7}O_{4,5}O_{4,5}$, ~100eV)/$Ge(M_1M_2V$, ~50 eV) AES peak ratio before and after annealing in our experiments. In this case, the Bi/Ge(111) system does not reach the global equilibrium, instead, highly nonuniform bismuth distribution prevails in the form of islands with no long range ordering.

In STM, one has to achieve atomic resolution in order to establish the structure we are dealing with. Ohtsubo et al used a low bias voltage of only 50 mV to resolve Bi atoms within the trimers [8]. We were not able to obtain stable tunneling at bias voltages smaller than ±0.4 V when the probe tip was placed over the pure germanium substrate. Such behavior can be attributed to the insufficient density of states within the bulk/surface band gaps of Ge(111) - 2 × 8. This circumstance prevented us from using low bias on samples, where Ge substrate was at least partially exposed.

The other coverage segment of our data (figs. 1g,h; 2e-h; 3a, b) needs to be compared with the investigations of S. Hatta et al. This group deposited up to 14 ML of bismuth onto a substrate at 120, 300, 350 K with a postdeposition annealing at the 400 K for 1 min.

Figures 2 e), f) and g), h) show a large-scale STM image at 7 and 10 ML correspondingy. The most part of the surface is covered with two-dimensional Bi islands with the various sizes of 10–40 nm and larger primitive nano-objects. The observed step height is evaluated to be 0.326 nm, wich roughly corresponds to the interlayer distance of bulk Bi(110) (0.328 nm).

It is expected that annealing after the deposition promotes the growth of higher islands with a smaller lateral dimension.

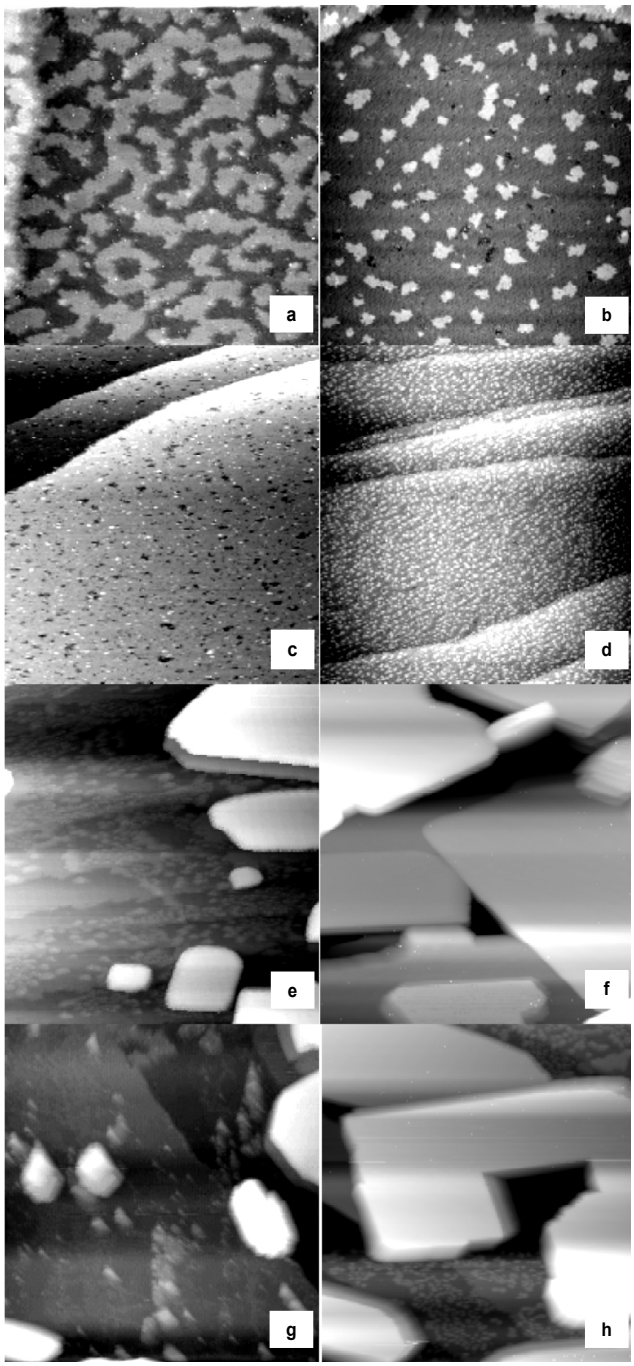

Fig. 2. STM images 125 nm × 125 nm of ultrathin Bi films on Ge(111) – 2 × 8 after deposition at RT and annealing at 450 K: a) 0.1 ML, U_{sample} = 2.0 V; b) 0.5 ML, U_{sample} = 2.0 V; c) 1 ML, U_{sample} = -2.0 V; d) 1.5 ML, U_{sample} = -2.0 V; e) 7 ML, U_{sample} = 2.0 V; f) 7 ML, U_{sample} = 2.0 V; g) 10 ML, U_{sample} = 2.0 V; h) 10 ML, U_{sample} = 2.0 V

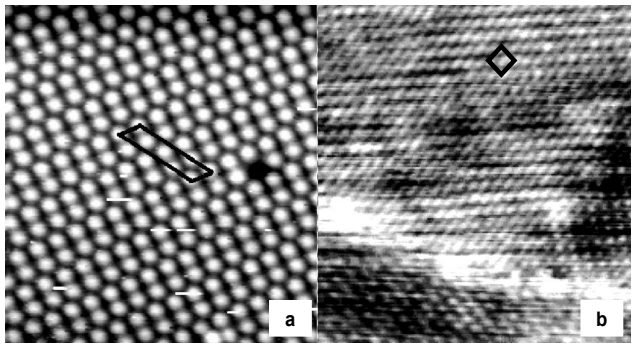

Fig. 3. STM images 12.5 x 12.5 nm of the Ge(111) – 2 × 8 substrate and 12.5 x 12.5 nm thin Bi film deposited at RT: a) pure Ge(111) – 2 × 8, Usample = 1.0 V; b) 10 ML, Usample = 0.1 V. Black square – unit cell

Fig. 3 shows STM images obtained before and after bismuth deposition on Ge(111) - 2 × 8 at RT. One can see Ge and Bi unit cells: (2 x 8) (fig. 3a) and (2 x 2) (fig. 3b). From the last figure we can conclude that 10 ML Bi film has pseudosquare lattice, wich according to its periodicity corresponds to (110)-plane. A theoretical periodicity of the pseudosquare lattice is 4.54 A x 4.75 A [3], while experimental value is 4.64 A x 4.80 A. Therefore, it seems evident, that no structural change from (110) to (111) is happening after annealing at 400 K for 1 min in the case of 10 ML coverage.

Conclusions. In this paper we have followed the deposition of ultrathin Bi films at room temperature onto Ge(111) - 2 × 8. Our STM data indicate the intermediate case between the layer by layer and 3D growth modes up to 10 ML nominal film thickness. No long range order was present in as-deposited films, however, small patches of the 2 × 1 zig-zag chain structure, intrinsic to 1 ML Sb/Ge(111), were observed. We have also investigated our films after moderate annealing at ~ 450 K, which did not lead to bismuth desorption from the substrate. Nano-objects formation was observed after increasing of Bi-film thickness up to 10 ML. From atomically-resolved STM- images, we concluded that before and after annealing at ~ 450 K, the bismuth islands have quasi-cubic unit cell, which roughly corresponds to the bulk Bi(110) structure.

1. *Cheng C., Kunc K.* Structure and stability of Bi layers on Si(111) and Ge(111) surfaces. // Phys. Rev. B – 1997 – Vol. 56. 2. Hatta *S., Aruga T., Ohtsubo Y. and Okuyama H.* Large Rashba spin splitting of surface resonance bands on semiconductor surface// Phys. Rev. B – 2009 – Vol. 80. 3. *Hatta S., Ohtsubo Y., Miyamoto S., Okuyama H., Aruga T.* Epitaxial growth of Bi films on Ge(111). // Appl. Surf. Sci. – 2009 – Vol. 256. 4. *Koroteev Yu. M. , Bihlmayer G., Chulkov E. V., Blügel S.* First-principles investigation of structural and electronic properties of ultrathin Bi films // Phys. Rev. B – 2008 – Vol. 77. 5. *Kuzmin M., Laukkanen P., Perälä R. E., Ahola-Tuomi M., Väyrynen I. J.* High-resolution core-level photoemission study of Ge(111) 2 x 1 – Sb and Ge(111)(√3x√3)*R*30◦ – Bi reconstructions. // Journal of Electron Spectroscopy and Related Phenomena – 2007 – Vol.159. 6. *Kuzmin M., Laukkanen P., Peraëlaë R. E., Ahola-Tuomi M., VaëyrynenI.J.* Atomic geometry and electronic properties of the Ge(111)2 x 1 – Sb surface studied by scanning tunneling microscopy/spectroscopy and core-level photoemission. // Surf. Sci. – 2007 – Vol. 601. 7. *Lyubinetsky I. V., Melnik P. V., Nakhodkin N. G., Anisimov A. E.* A reliable compact ultra-high vacuum scanning tunneling microscope. // Vacuum 46. – 1995. 8. *Ohtsubo Y., Hatta S., Iwata M., Yaji K., Okuyama H., Aruga T.* Structure determination of Bi/Ge(111)-(√3x√3)R30◦ by dynamical low-energy electron diffraction analysis and scanning tunneling microscopy. // J. Phys.: Condens. Matter – 2009. – Vol. 21. 9. *Wan K. J., Ford W. K., Lapeyre G. J., Hermanson J. C.* Observation and low-energy-electron-diffraction structure analysis of the Ge(111)(√3x√3)*R*30◦– Bi system. // Phys. Rev. B – 1991 – Vol. 44.

Submitted 20.09.10

Наукове видання

ВІСНИК

КИЇВСЬКОГО НАЦІОНАЛЬНОГО УНІВЕРСИТЕТУ ІМЕНІ ТАРАСА ШЕВЧЕНКА

РАДІОФІЗИКА ТА ЕЛЕКТРОНІКА

Випуск 15

Друкується за авторською редакцією

Оригінал-макет виготовлено Видавничо-поліграфічним центром "Київський університет"

**Підписано до друку 10.03.11. Формат 60x84$^{1/8}$. Вид. № РФ1. Гарнітура Arial. Папір офсетний.
Друк офсетний. Наклад 300. Ум. друк. арк. 7,2. Обл.-вид. арк. 10,0. Зам. № 211-5563.**

**Видавничо-поліграфічний центр "Київський університет"
01601, Київ, б-р Т. Шевченка, 14, кімн. 43
☎ (38044) 239 32 22; (38044) 239 31 72; (38044) 239 31 58; факс (38044) 239 31 28**